

N 00-16378

FACILITY FORM 602

(ACCESSION NUMBER)
104
(PAGES)
CR49869
(NASA CR OR TMX OR AD NUMBER)

(THRU)
1
(CODE)
33
(CATEGORY)

GPO PRICE \$ _____

CFSTI PRICE(S) \$ _____

Hard copy (HC) 164.00

Microfiche (MF) .75

ff 653 July 65

COUPLED CONVECTIVE AND
RADIATIVE HEATING TO
SUPERORBITAL ENTRY VEHICLES

October 1965

TASK I OF A FUNDED STUDY ON SUPERORBITAL ENTRY HEATING
PROBLEMS UNDER CONTRACT NAS 7-295

PREPARED BY:

A. C. Buckingham
A. C. Buckingham, Member
Aerospace Sciences Laboratory

H. Hoshizaki
H. Hoshizaki, Senior Member
Aerospace Sciences Laboratory

FOREWORD

The work described in this report was completed for the National Aeronautics and Space Administration Headquarters, under the terms and specifications of their Contract NAS 7-295, issued through their Western Operations Office, 150 Pico Boulevard, Santa Monica, California - 90406.

The work was performed in Lockheed Missiles & Space Company's Aerospace Sciences Laboratory under R. D. Moffat, Manager.

ABSTRACT

16378

Results of theoretical studies on the coupled radiative and convective heating for superorbital entry conditions are presented. The velocity range is $30 \leq U_{\infty}(\text{K-fps}) \leq 50$. The altitude range is $150 \leq F_{\infty}(\text{K-ft}) \leq 250$. Geometries analyzed consisted of hemisphere-cones with varying cone-frustrum half angles, paraboloids, and power law bodies generated by a hybrid half-power equation. The analytical profiles generated had continuously diminishing body curvature.

The results are given as correlations of digital computer results. Simple algebraic relations for the convective and radiative distributions are developed. These relations are in turn integrated over surface area for the geometries studied. Graphs and polynomial curve fits of the integrals are given in addition to the correlation equations. Also presented are results of applications of the equations made for entry conditions within the range of validity of the correlations.

author

CONTENTS

<u>Section</u>	<u>Page</u>
FOREWORD	ii
ABSTRACT	iii
ACKNOWLEDGEMENTS	iv
ILLUSTRATIONS	vi
TABLES	x
NOTATION	xi
1 INTRODUCTION	1-1
2 TECHNICAL DISCUSSION	2-1
3 DEVELOPMENT OF CORRELATIONS AND RESULTS	3-1
3.1 CONVECTION HEATING	
3.2 RADIATIVE HEATING	
3.3 AN EVALUATION OF GEOMETRICAL EFFECTS	
3.4 EFFECT OF MASS INJECTION AND SELF ABSORPTION OF RADIANT ENERGY	
SUMMARY AND CONCLUSIONS	
REFERENCES	
Appendix	
A ANALYSIS OF ENTRY TRAJECTORY, NOSE RADIUS, AND NOSE BLUNTNESS	
A.1 ENTRY TRAJECTORY AND NOSE RADIUS OF CURVATURE	
A.2 NOSE BLUNTNESS	

ACKNOWLEDGEMENTS

The writers would like to express their sincere appreciation to the following members of the laboratory for their helpful discussions and suggestions during the course of the work described in this report: K. H. Wilson and W. E. Nicolet. Particular thanks are extended to: H. R. Hirsch for her many contributions in IBM code revisions, programming and suggestions on the numerical analysis; M. A. Snaider for her work on the polynomial curve fits of the integrated heating expressions; J. E. Newt for his diligent work in reduction of results, supporting calculations, and preparation of figures for the report.

FIGURES

<u>Figure No.</u>		<u>Section</u>
1	Hypersonic Pressure Distributions for Various Re-entry Conditions, Geometries	2
2	Variation in Radiation Loss Parameter over Trajectory Range Analyzed	2
3	Upper and Lower Estimate of High-Temperature Air Emissivity	2
4	Summary of Geometries Analyzed	2
5	Boundary Layer Convection Solutions (Adiabatic Shock Layer) For Geometries Analyzed	3.1
6	Correlation of Convective Heat Flux Coupling Defect with Pressure Distribution	3.1
7	Conical Surface Correlations of Heat Flux Components - Hemisphere Cones	3.1
8	Dimensionless Convection Integral, $\sqrt{I_1}$ - Hemisphere Cones	3.1
9	Dimensionless Convection Integral, $\sqrt{I_1}$ - Paraboloids, Power-Laws	3.1
10	Dimensionless Convection Integral, I_2 - Hemisphere Cones	
11	Dimensionless Convection Integral, I_2 - Paraboloids, Power Laws	3.1
12	Dimensionless Convection Integral, I_3 Conical Surface Hem. Cones	3.1
13	Convection Heating Integrated Over Surface Area - $\bar{Z}_\infty = 1.5, \bar{U}_\infty = 3$	3.1

<u>Figure No.</u>	<u>Title</u>	<u>Section</u>
14	Convection Heating Integrated Over Surface Area - $\bar{Z}_\infty = 1.5, \bar{U}_\infty = 4$	3.1
15	Convection Heating Integrated Over Surface Area - $\bar{Z}_\infty = 1.5, \bar{U}_\infty = 5$	3.1
16	Convection Heating Integrated Over Surface Area - $\bar{Z}_\infty = 1.5, \bar{U}_\infty = 3$	3.1
17	Convection Heating Integrated Over Surface Area - $\bar{Z}_\infty = 1.9, \bar{U}_\infty = 4$	3.1
18	Convection Heating Integrated Over Surface Area - $\bar{Z}_\infty = 1.9, \bar{U}_\infty = 5$	3.1
19	Convection Heating Integrated Over Surface Area - $\bar{Z}_\infty = 2.5, \bar{U}_\infty = 3$	3.1
20	Convection Heating Integrated Over Surface Area - $\bar{Z}_\infty = 2.5, \bar{U}_\infty = 4$	3.1
21	Convection Heating Integrated Over Surface Area - $\bar{Z}_\infty = 2.5, \bar{U}_\infty = 5$	3.1
22	Reduction in Stagnation Point Radiative Heat Flux as a Function of Radiation Loss Parameter	3.2
23	Correlation of Radiation Heat Flux With Pressure Distribution	3.2
24	Radiative Heat Flux Distribution, Hemisphere Cones Comparison of Correlation Equation with Computer Solution	3.2
25	Dimensionless Radiation Integral, I_4 , Hemisphere Cones	3.2
26	Dimensionless Radiation Integral, I_4 , Paraboloids, Power-Laws	3.2

<u>Figure No.</u>	<u>Title</u>	<u>Section</u>
27	Dimensionless Radiation Integral, I_5 , Hemisphere Cones	3.2
28	Radiation Heating Integrated Over Surface Area, $\bar{Z}_\infty = 1.5, \bar{U}_\infty = 3$	3.2
29	Radiation Heating Integrated Over Surface Area, $\bar{Z}_\infty = 1.5, \bar{U}_\infty = 4$	3.2
30	Radiation Heating Integrated Over Surface Area $\bar{Z}_\infty = 1.5, \bar{U}_\infty = 5$	3.2
31	Radiation Heating Integrated Over Surface Area, $\bar{Z}_\infty = 1.9, \bar{U}_\infty = 3$	3.2
32	Radiation Heating Integrated Over Surface Area, $\bar{Z}_\infty = 1.9, \bar{U}_\infty = 4$	3.2
33	Radiation Heating Integrated Over Surface Area, $\bar{Z}_\infty = 1.9, \bar{U}_\infty = 5$	3.2
34	Radiation Heating Integrated Over Surface Area, $\bar{Z}_\infty = 2.5, \bar{U}_\infty = 3$	3.2
35	Radiation Heating Integrated Over Surface Area, $\bar{Z}_\infty = 2.5, \bar{U}_\infty = 4$	3.2
36	Radiation Heating Integrated Over Surface Area, $\bar{Z}_\infty = 2.5, \bar{U}_\infty = 5$	3.2
37	Dimensionless Enclosed Volume - Geometries Analyzed	3.3
38	Effects of Geometry on Total Heating for Fixed Volume	3.3
39	Continuum Absorption Coefficients of Nitrogen	3.4
40	Static Enthalpy Profiles	3.4
41	Ratio of Radiative Flux With and Without Self Absorption for a Slab of Gas 1 cm. Thick	3.4
42	Radiative Flux as a Function of Frequency, $h\nu$	3.4

<u>Figure No.</u>	<u>Title</u>	<u>Section</u>
43	Reduction of Convective Heating Due to Mass Injection	3.4
A.1	Spherical Nose Radius for Minimum (Stagnation Point) Total Heating	A.1

TABLES

<u>Table No.</u>	<u>Title</u>	<u>Section</u>
1	Cases Analyzed with Viscous Shock Layer	2
2	Polynomial Coefficients - Convection Integrals	3.1
3	Polynomial Coefficients - Radiation Integrals	3.2

NOTATION

A, B	Arbitrary coefficients of power law provide (p. 2-1). Polynomial coefficients, eq. (9).
A_1, A_2	Numerical correlation coefficients; eq. (6), eq. (12), respectively.
C_o	Constant in convection similarity expression (eq. (7)); dependent on free stream conditions.
C, D, E	Polynomial coefficients, eq. (9).
$F(\beta, t_E)$	Convection correlation function, eq. (2). Computer from Cohen (Ref. 10, p. 32).
$f(\Gamma)$	Radiation coupling function, eq. (13).
g_1, g_2	Correlation functions, heat flux in conical flow region; eq. (6), eq. (12), respectively.
I_1, I_2, I_3, I_4, I_5	Heating integrals defined in eqs. (3), (8), (14).
L	Characteristic length in correlations ($L = R_N$).
M, N	Correlation exponents, eq. (5).
p	Static pressure.
q_c, q_r	Convective, radiative heat flux.
R_N	Radius of curvature of the entry body measured at forward stagnation point.
\tilde{R}	Dimensionless radius of curvature, ($R_N^{1/2}$ ft).
r	Radial cylindrical coordinate.
U	Velocity.
V	Enclosed volume of entry body, subsection 3.3.
v_1, v_2	Correlation exponents; eq. (5), (12), respectively.
x	Body surface distance, measured from forward stagnation point.

y	Correlation exponent, pressure expansion, eq. (4).
Z_{∞}	Altitude.
z	Axial cylindrical coordinate.
β	Stagnation point velocity gradient.
Γ	Radiation loss parameter.
γ	Isentropic exponent.
ϵ/L	Emissivity per unit length of shock layer.
θ	Local body surface angle as measured from radial axis.
μ	Viscosity coefficient.
ξ	Dimensionless body surface distance, (x/R_N).
ρ	Gas Density.
ϕ_c	Cone frustrum half-angle.

Subscripts

δ, e	Refers to conditions at "outer edge" of boundary layer.
θ	Refers to local body surface angle.
0	Refers to conditions at forward stagnation point.
T	Refers to body surface tangency point (hemisphere-cone).
∞	Refers to free stream conditions.
s	Refers to conditions behind the shock.
w	Refers to conditions at the wall.

1. INTRODUCTION

This final report describes the work carried out under Task 1 of NASA Contract No. NAS 7-295. The purpose of this study was to determine the effect of vehicle shape on the convective and radiative heating during super-orbital reentry. The effect of coupling between the convective and radiative heating created by radiation cooling was considered in detail. The body shapes considered were hemisphere cones and analytic bodies such as paraboloids and power law generated profiles with continuously decreasing body curvatures.

The intent of the present work was to study the flow field in detail around particular vehicles at representative entry conditions rather than to make a complete trajectory analysis. Preliminary studies were first carried out to determine which points in a given family of entry trajectories would be most representative of the total heating pulse. The results of this study were used to select the most representative entry conditions and detailed studies were carried out on the local and total heating at these trajectory points. A summary of the results of the initial trajectory studies along with a discussion of the effect of nose radius and nose bluntness on the total heating appear in appendix A of this report.

The convective and radiative heating to various vehicle shapes were calculated using the viscous shock layer analysis of Hoshizaki and Wilson, (Ref. 1). In Ref. 1 the viscous, radiating flow in the shock layer about a blunt nosed body is analyzed by an integral method. This is a direct method in that the shock shape and flow details in the shock layer are determined for a specified body shape. The method of solution is as follows. The governing equations are first simplified by means of the thin shock approximations. This reduces the Navier-Stokes equations and the complete energy equation to essentially the

boundary-layer equations with the addition of the curvature terms. These equations are then integrated across the shock layer to eliminate one independent variable. The integrals in the resulting equations are evaluated by representing the velocity and total enthalpy profiles by polynomials with unknown coefficients.

All of the coefficients, with the exception of one coefficient in the total enthalpy profile, are determined by means of appropriate boundary conditions. The remaining coefficient is determined by satisfying the integrated energy equation. The integrated momentum equation is used to determine the shock stand-off distance.

The resulting equations are solved numerically by an iteration method. A shock shape is assumed and the equations integrated around the body to obtain the details of the flow field and a new shock shape. The shock shape is used to replace the assumed shock shape and the equations are re-integrated. This procedure is repeated until satisfactory convergence is obtained. Real gas properties are utilized in the numerical solutions (Ref. 2). The numerical solution will accept arbitrary air emissivity data. Emissivity data used in the present study is discussed in Section 2 of this report.

It was originally intended to use the viscous shock layer program to calculate the radiative and convective heating for each condition of interest. It soon became apparent, however, that it would be far more economical and useful to develop correlation equations based on results of the computer solutions for the local convective and radiative heating as a function of vehicle shape, velocity and flight altitude. The correlation formulas for the local heat flux can then be integrated to obtain the total heating to the vehicle as a function of the trajectory parameters. Hence, the correlation formulas can be used to determine the total heating to a given vehicle shape over a wide range of trajectory conditions with very little effort since these correlation formulas are simple analytic functions.

Correlation formulas for the radiative and convective heating have been obtained for hemisphere cones, paraboloids, and power law bodies.

These correlation formulas do not include the effect of self absorption of radiant energy or the effect of mass injection into the shock layer. Self absorption was neglected on the basis of estimates made using the gray-gas approximation. These estimates indicated that the shock layer was optically thin for a wide range of entry conditions. We now know, however, that the gray-gas approximation is a very poor one and that self absorption can be important under almost all entry conditions of interest. The correlation formulas presented are still useful, however, since they have been normalized to the heating rate at the stagnation point. Thus, it is felt for reasons discussed in more detail in Subsection 3.4 that the distribution of the radiative and convective heating under some conditions will not be significantly affected by self absorption. Self absorption will certainly tend to raise or lower the absolute heating levels but probably has a small effect on the relative heating to different vehicle shapes. The analysis presented herein is then useful for making relative studies on the effect of vehicle shape and entry conditions on the total heating.

Mass injection can have a very significant effect on the convective heating and may also be significant in reducing the radiative heating if self absorption is taken into account. A brief discussion of the effect of mass injection on the results presented is given in Subsection 3.4.

2. TECHNICAL DISCUSSION

The digital computer program used in the present analysis was based on the Hoshizaki-Wilson integral shock layer method (Ref. 1). The program calculates the coupled convective and radiative heating to a body of revolution entering a planetary atmosphere at superorbital speeds. The original computer code, developed for hemisphere-cones with arbitrary cone frustrum half angles has been modified to generate results for paraboloids and power-law profiles with continuously decreasing body curvatures. The power law profile is a modified half-power body of revolution generated by the equation: $r = A\sqrt{z} + Bz$, where r and z are, respectively, the radial and axial cylindrical coordinates with reference to the origin at the forward stagnation point. The coefficients, A and B , are arbitrarily specified when initiating a calculation. This permits development of a considerable variation of profiles within this general family, that may be of interest or closely simulate other geometries of interest.

Initially, it was planned to use the computer code to generate results for a large number of cases covering a practical range of entry velocities and altitudes where strong coupling effects were anticipated. However, study of the preliminary results suggested that a more general and useful analysis could be developed through empirical correlation of computer code results over a range of flow conditions where strong coupling was encountered. Clearly if such a correlation of selected numerical results could be obtained, this would permit an economical extension of the analysis over intermediate flow conditions without excessive computer use. It was further recognized a set of simple algebraic relations might be obtained which could, in turn, be used repeatedly in systematic application of the correlations to check the effects of governing parameters. The added usefulness of explicit, easily applied algebraic relations for design applications is of course, obvious.

The independent variable sought as the primary correlation parameter was the surface pressure distribution. This seemed the most desirable correlation variable on the basis of several considerations. Among the more prominent considerations we note:

1. For hypersonic flow the surface pressure distribution, normalized to the stagnation point value, is essentially a function only of the geometry. Hence, correlations developed on the basis of this variable are to all intents uncoupled from variations in free stream flow conditions.
2. There probably exists as much or more reported and available data on surface pressure distributions than any other flow variables for arbitrary geometries, based on exact numerical solutions and experiment.
3. Surface pressure distributions may be readily computed for bodies of revolution and asymmetric bodies using an assortment of analytical approximations of varying degrees of accuracy and ease of application, i.e., conical flow solutions, modified Newtonian law, shock expansion theory, blast wave theory, etc.

Certainly, initial consideration of surface pressure as a correlation variable is strongly supported by practical considerations. It will be shown that functional relationships based on the pressure distribution can be and have been developed which satisfactorily correlate the complex physical processes analyzed through use of the digital computer solutions. The relative insensitivity of the surface pressure to flow conditions for similar geometries is illustrated in Fig. 1. This figure shows a summary of the pressure distributions from numerical results of the present computer solutions over the range of entry conditions and geometries studied. The independent variable, ξ , is the ratio of the distance along the body surface divided by the radius of curvature of the nose measured at the axis of symmetry. The distance is measured along the body surface from an origin at the forward stagnation point.

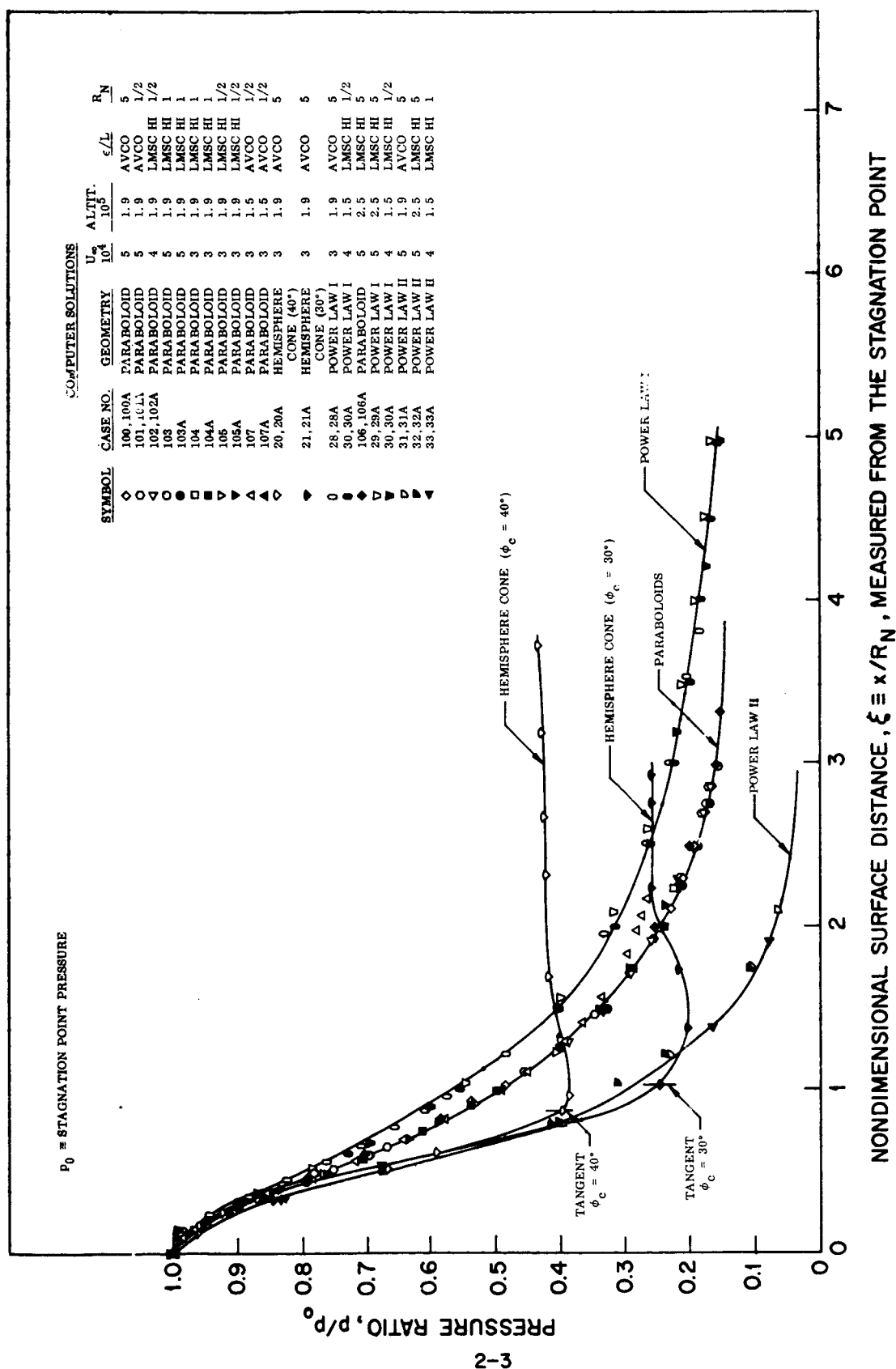


Fig.1 Hypersonic Pressure Distributions for Various Reentry Conditions, Geometries

The necessity for a small radius of curvature, considering combined effects of radiation and convection became obvious after a preliminary study of several lifting re-entry trajectories and heating profiles. This preliminary work is discussed in Appendix A of this report. The desirability of small entry vehicle nose radii in the superorbital entry flight regime to minimize total heating is emphasized by the results of entry heating studies made by Allen & Seiff (Ref. 3) at NASA on slender cones.

The range of altitudes and velocities covered was limited in part by limitations on the valid range of the curve fits of emissivity, thermodynamic and particle transport property data used in the computer code. The data for the thermodynamic & transport properties are from (Ref. 2). Extensions of these data to higher temperatures and a larger range of densities are planned for a new computer program presently being developed which will include the important effects of self-absorption mentioned in the introduction. The curve fit limits in the code presently used, limit, in turn the velocity (temperature) and density. The practical limits for solutions were found to restrict entry velocities to 50,000 fps or less and altitudes no greater than 250,000 ft.

The onset of significant radiation coupling could be investigated through the magnitude of the coupling parameter, Γ , which is a ratio of the radiant energy loss by a fluid particle to the total energy within the time (δ/V_δ) . Here V_δ is the normal velocity behind the shock and δ is the shock stand-off distance. The lower bound on velocity was established at $U_\infty = 30,000$ fps where the value of Γ is negligibly small. Thus, radiation coupling could be considered unimportant. Figure 2 shows bands of values of Γ determined from results of the solutions for the cases analyzed. The variation of values in Γ for a fixed velocity and altitude was the result of variations in the air emissivity specified (3 optional levels are available in the current program) as well as a weaker effect caused by varying the nose radius of curvature. The distribution of points was narrow enough to permit selection of a representative value of Γ for a fixed velocity and altitude in the later analysis. Two of the emissivity values used in the computer

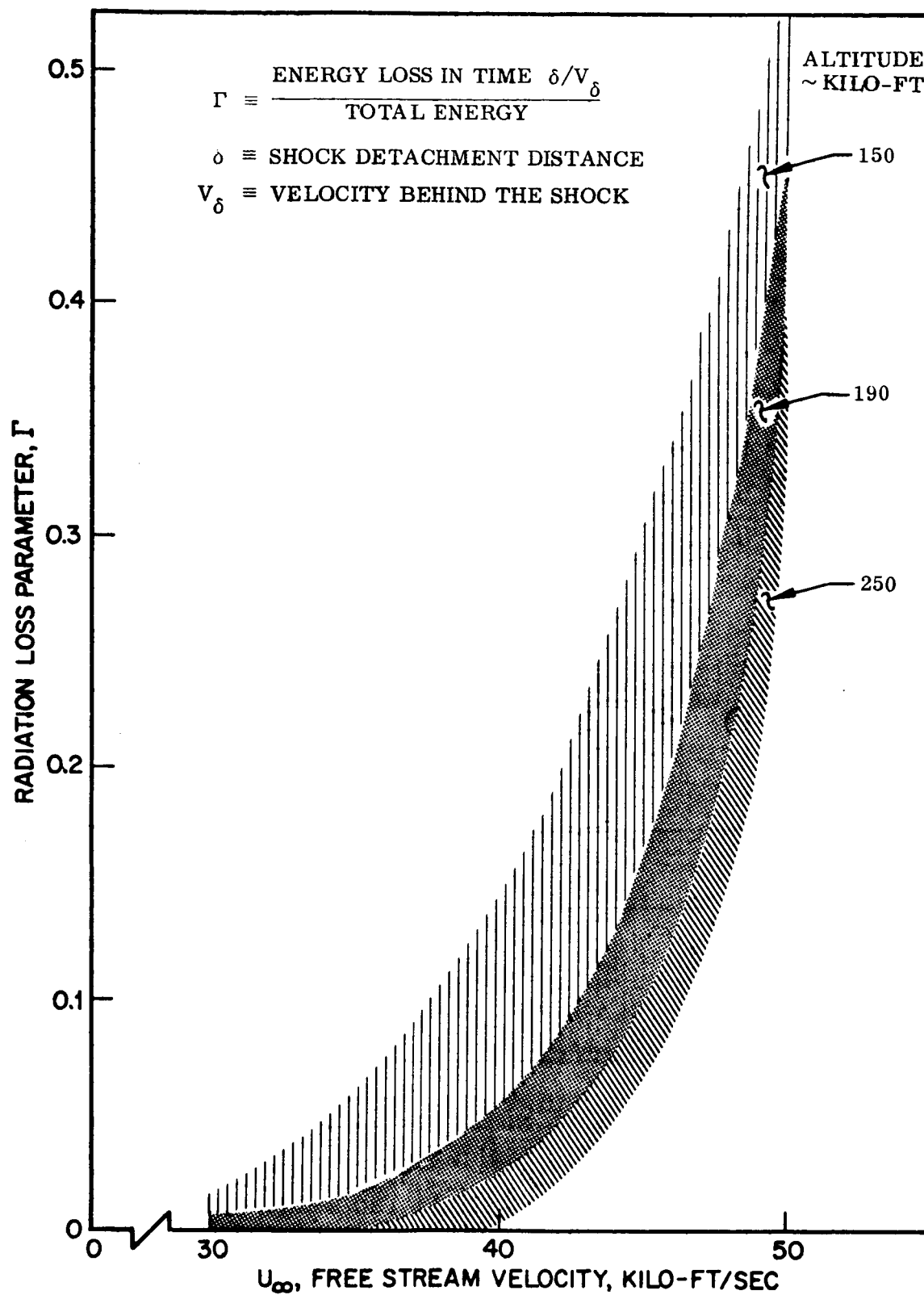


Fig. 2 Variation in Radiation Loss Parameter Over Trajectory Range Analyzed

program are shown in Fig. 3 which depicts the log of the emissivity as a function of temperature and density. These estimates represent high and low levels with and without atomic line contributions), based on calculations made at Lockheed. The third emissivity prediction used is that developed at Avco (Ref. 4) and used by Howe and Viegas (Ref. 5) at NASA. The Avco data is bracketed by the Lockheed upper and lower estimates shown.

Computer solutions are initiated by a selection of the flight and shock layer conditions (present studies were based on the normal shock wave data of P. V. Marrone, (Ref. 6)), and a selection of the geometrical parameters. The 32 numerical cases on which the present analysis and correlations are based is summarized in Table 1 which depicts, in addition to the geometries and flow conditions, the value of the radiation loss parameter, Γ .

The explicit geometries investigated are given in Fig. 4 in terms of the dimensionless cylindrical coordinates \bar{r} , \bar{z} in the radial and axial directions, respectively. These dimensions have been ratioed to the radius of curvature of the nose measured at the stagnation point, R_N .

In the next section examination of theoretical relations and the numerical results of the solutions will be reviewed. Development of correlations for the convective and radiative heat flux distribution will be discussed and compared with results of the numerical analysis. The relations developed are referenced to the stagnation point heat flux, which can be readily obtained for the case of convective heating from existing correlations such as Hoshizaki (Ref. 7). The stagnation radiative heat flux may be readily computed using one of the several current predictions for air emissivity for optically thin shock layers and additional data on the flight conditions leading to values of the shock stand-off distance and shock-layer temperature. Correlation equations also exist for planar radiation to an optically thin stagnation region such as those of P. D. Thomas (Ref. 8).

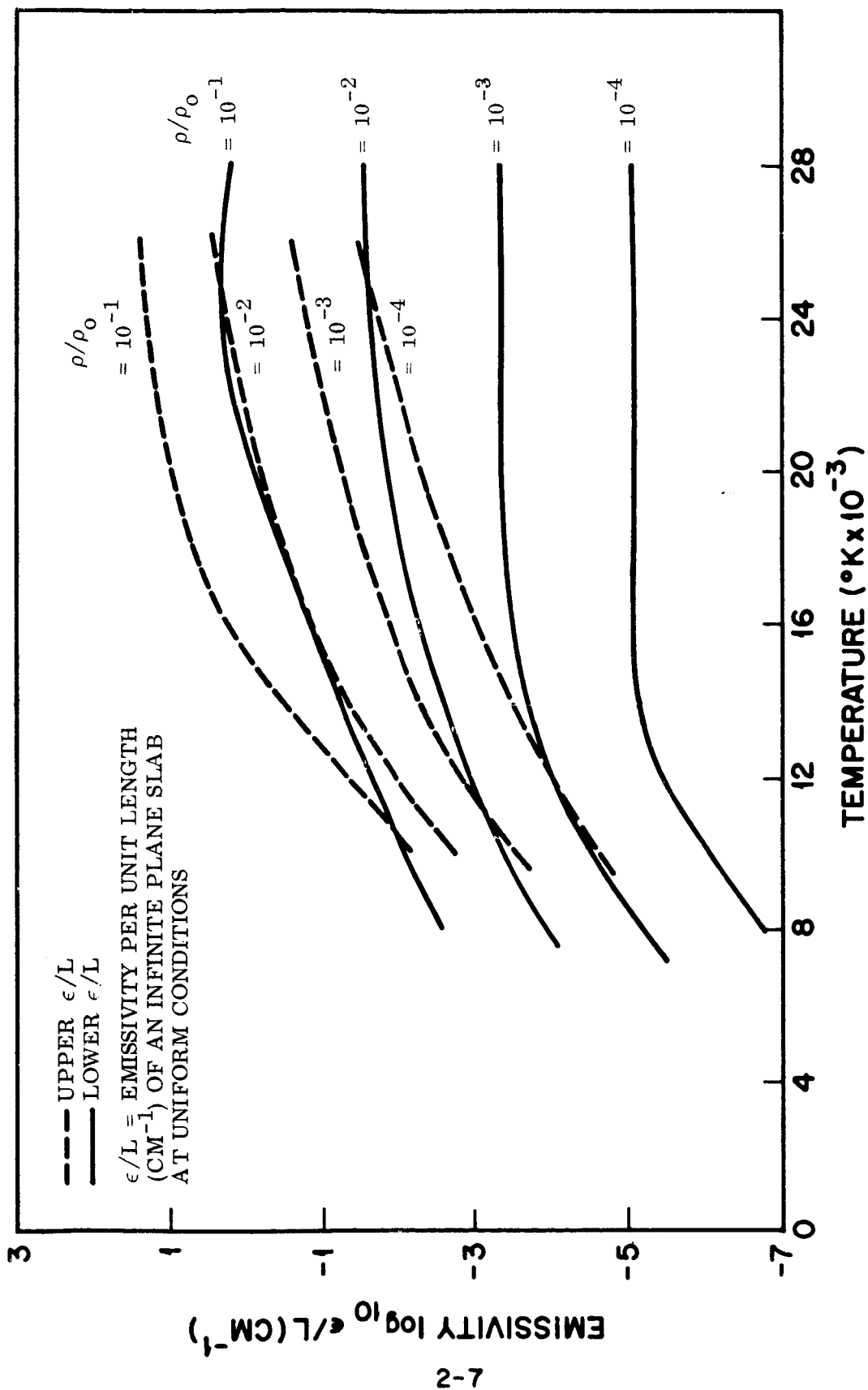


Fig.3 Upper and Lower Estimate of High-Temperature Air Emissivity

Table 1
CASES ANALYZED WITH VISCOUS-RADIATING SHOCK LAYER COMPUTER PROGRAM

	\bar{Z}_{∞}	\bar{U}_{∞}	ϵ/L	R_N		
Case No.	($\frac{\text{Altitude}}{10^5 \text{ ft}}$)	($\frac{U_{\infty}}{10^4 \text{ fps}}$)	(Emissivity) Used	(ft)	Γ	Geometry
20, 20A*	1.9	5	AVCO	5	0.416	Hem-Cone, $\phi_c = 40^\circ$
21, 21A	1.9	5	AVCO	5	0.416	Hem-Cone, $\phi_c = 30^\circ$
28, 28A	1.9	5	AVCO	5	0.416	Pwr. Law I
29, 29A	2.5	5	IMSC H1	5	0.318	Pwr. Law I
30, 30A	1.5	4	IMSC H1	$\frac{1}{2}$	0.146	Pwr. Law I
31, 31A	1.9	5	AVCO	5	0.416	Pwr. Law II
32, 32A	2.5	5	IMSC H1	5	0.316	Pwr. Law II
33, 33A	1.5	4	IMSC H1	1	0.274	Pwr. Law II
100, 100A	1.9	5	AVCO	5	0.416	Paraboloid
101, 101A	1.9	5	IMSC H1	$\frac{1}{2}$	0.226	Paraboloid
102, 102A	1.9	4	IMSC H1	$\frac{1}{2}$	0.0524	Paraboloid
103, 103A	1.9	5	IMSC H1	1	0.465	Paraboloid
104, 104A	1.9	3	IMSC H1	1	0.0085	Paraboloid
105, 105A	1.9	3	IMSC H1	$\frac{1}{2}$	0.00414	Paraboloid
106, 106A	2.5	5	IMSC H1	5	0.318	Paraboloid
107, 107A	1.5	3	AVCO	$\frac{1}{2}$	0.00108	Paraboloid

* (A) Suffix Designates Adiabatic Case

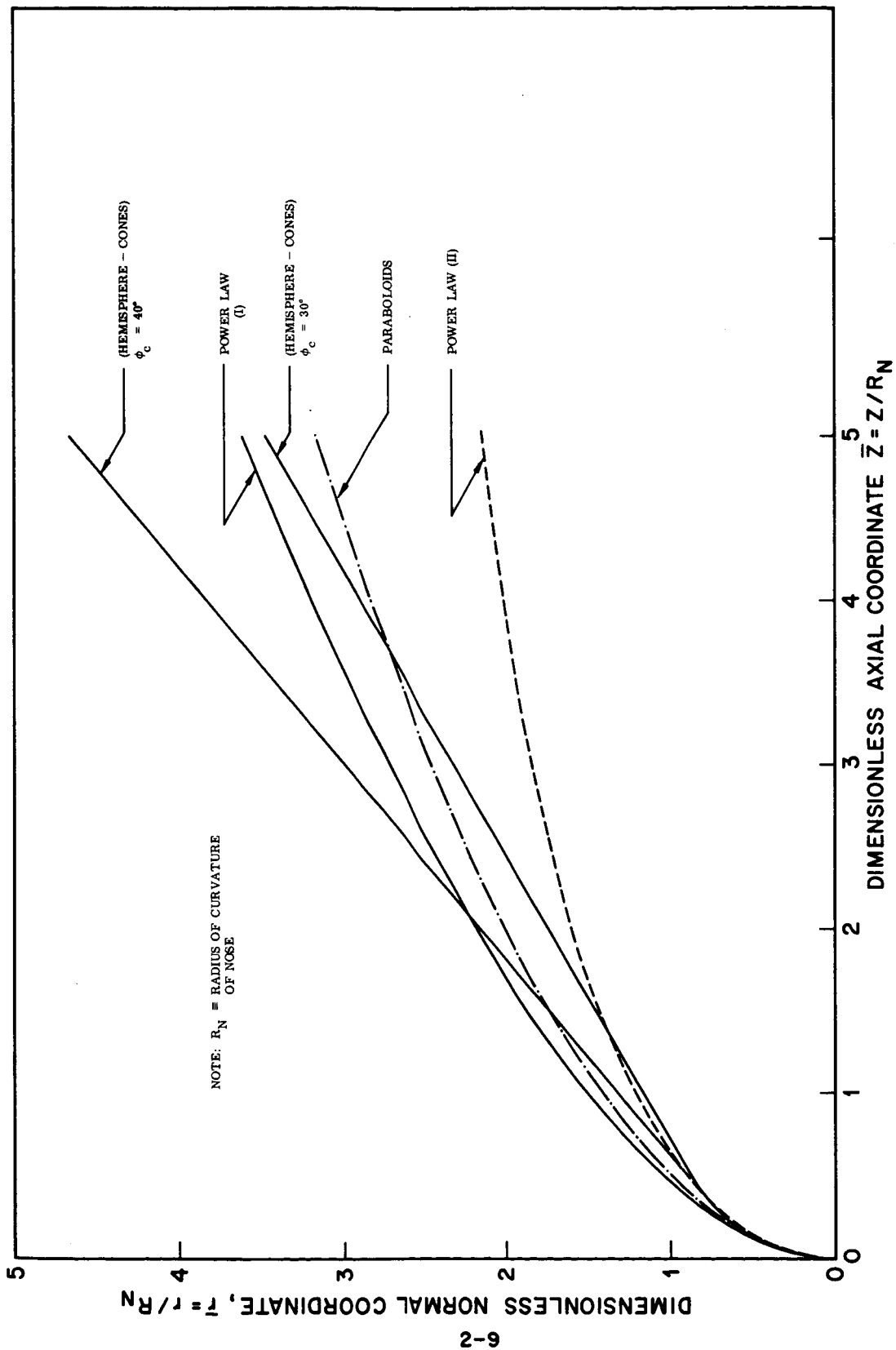


Fig. 4 Summary of Geometries Analyzed

3. DEVELOPMENT OF CORRELATIONS AND RESULTS

3.1 CONVECTIVE HEATING

3.1.1 Correlation of Convective Heat Flux Distribution

The convective heat flux is noticeably diminished below the level predicted by boundary layer theory when there exists a significant degree of coupling between the shock layer radiation loss and the energy convected toward the vehicle surface during planetary entry (Ref. 1). The distribution of convective heat flux along the vehicle surface, including the effects of such coupling may be written as a simple expression. The expression is simply a statement that the distribution of heat flux in a non-adiabatic or coupled flow situation is the difference between adiabatic boundary layer theory results and a coupling term which accounts for the energy lost from the shock layer due to gas radiation:

$$\frac{q_c(\xi)_{\text{Non-Adiab.}}}{q_c(0)_{\text{Adiab.}}} = \frac{q_c(\xi)}{q_c(0)}_{\text{b.l.}} - \Delta q_c(\xi) \quad (1)$$

In eq. (1) ξ is surface distance ratioed to the nose radius of curvature, measured from the forward stagnation point. The second term on the RHS of eq. 1, $\Delta q_c(\xi)$ represents the convective coupling defect. The subscripts, "Adiab.", "Non-Adiab" refer to the uncoupled and coupled heat flux components, respectively. These are evaluated from separate computer solutions for adiabatic and non-adiabatic shock layer flow. Eq. (1) is a convenient expression to work with in correlating the convective heating results.

Numerical solutions developed from the Hoshizaki-Wilson integral method (Ref. 1) neglect the effects of self absorption in evaluating the shock layer radiation. The present results thus represent valid solutions only for flow conditions in which the shock layer gas can be considered transparent to the radiation. For flow conditions in which significant self absorption is encountered, the results would reflect a comparatively smaller coupling

defect. Thus results with self absorption would tend back towards the adiabatic results. Quantitative evaluation of the self absorption in coupled heating solutions is necessarily delayed until completion of a new version of the computer code presently in development. The omission of this effect in the present analysis was discussed in the introduction and will receive further attention in the discussion of the present results. However, trends and correlations indicated by the present analysis will possibly be amenable to relatively simple scaling and adjustment of the correlation coefficients once the new solutions are available. Clearly, in the interim period prior to completion of the new computer code, qualitative trends, geometrical effects, correlation techniques and results of the present analysis will be useful in application for systematic design studies.

The approach adopted for correlation of the numerical results and the development of expressions for the convective heating distribution is to examine separately the behavior of the two terms in the RHS of Eq. (1). The computer solutions are used as both a basis for and a check against the resulting correlations. Subsequently, the expressions are used to evaluate the heating integrated over the surface area. The surface area integration of heating is done numerically with results presented in both graphical form and in a table of coefficients from polynomial curve fits generated for the integrals.

An expression for the uncoupled boundary layer contribution to convection (first term on the RHS of Eq. 1) is adapted from work by Lees (Ref. 9) and later work by Cohen (Ref. 10). The expression is based on similarity solutions of the laminar boundary layer equations for an axisymmetric body of revolution immersed in equilibrium, high enthalpy shock-layer flow. In our present notation this expression becomes:

$$\left. \frac{q_c(\xi)}{q_c(0)} \right|_{b.l.} = \frac{F(\beta, t_E)}{\sqrt{\left\{ 2 \left[d(U_e/U_\infty) / d(r_w/L) \right] \right\}_{\theta=0}}} \cdot \frac{[(\rho\mu)_w / (\rho\mu)_{w,0}] (U_e/U_\infty) r_w/L}{\left\{ 2 \int_0^\xi [(\rho\mu)_w / (\rho\mu)_{w,0}] (U_e/U_\infty) (r_w/L)^2 d\xi \right\}^{1/2}} \quad (2)$$

In Eq. (2), the local wall quantities are designated by the subscript, w, while the subscript, $\delta, 0$, refers to conditions at the boundary layer "edge" (δ) evaluated at the forward stagnation point (o). The term, $F(\beta, t_e)$ represents Cohen's correlation function (p. 32, Ref. 10) which is dependent on the stagnation point velocity gradient, β and the ratio of stagnation point ("edge") enthalpy to a reference enthalpy, t_e . F (which is almost unity) may be evaluated for the particular flow conditions using Cohen's relation, but with care taken to evaluate the term $(\rho_w \mu_w / (\rho \mu)_{w,0})$ specifically from property data for the shock layer conditions of interest. To illustrate the solution development it is useful at this point to integrate Eq. (2) over the differential annular area element, $2\pi[r_w(\xi)/L] d\xi$. Making the substitution:

$$\chi = \int_{\xi} \frac{(\rho \mu)_w}{(\rho \mu)_{w,0}} \cdot \frac{u_e}{u_{\infty}} \left(\frac{r_w}{L} \right)^2 d\xi, \quad d\chi = \frac{(\rho \mu)_w}{(\rho \mu)_{w,0}} \frac{u_e}{u_{\infty}} \left(\frac{r_w}{L} \right)^2 d\xi$$

and introducing the differential area element into Eq. (2) we obtain after integration over both sides of the equation:

$$\begin{aligned} \frac{1}{L^2} \tilde{Q}_c(\xi) &= \int_{\text{Area}} \frac{q_c(\xi)}{q_c(0)} dA = 2\pi \cdot \text{const} \cdot \sqrt{2\chi} \\ &= \frac{2\pi \sqrt{2} \cdot F(\beta, t_e)}{\sqrt{\left\{ 2 \frac{d(U_e/U_{\infty})}{d(r_w/L)} \right\}_{\theta=0}}} \cdot \sqrt{I_1(\xi)} \end{aligned} \quad (3)$$

where

$$I_1(\xi) = \int_0^{\xi^*} \frac{(\rho \mu)_w}{(\rho \mu)_{w,0}} \frac{U_e}{U_{\infty}} \left(\frac{r_w}{L} \right)^2 d\xi$$

Further simplifications are possible, prior to evaluating I_1 for the cases under investigation. It is noted that for high enthalpy flows with relatively cool walls the variation of the term, $(\rho \mu)_w / (\rho \mu)_{w,0}$, may be closely simulated by the ratio, $P_w / P_0 = P(\xi) / P_0$. Also, for an equilibrium high enthalpy flow, the isentropic index varies slowly over the running length of the body from the stagnation

point, hence $\gamma(\xi)/\gamma(0) \approx 1$, for practical purposes and an isentropic expansion may be substituted for the velocity distribution:

$$\frac{u_e}{u_\infty} \cong \left[1 - \left(\frac{p(\xi)}{p_0} \right)^y \right]^{1/2}, \quad \text{where } y \equiv \frac{\gamma_0 - 1}{\gamma_0}$$

hence,
$$I_1(\xi) = \int_0^{\xi^*} \frac{p(\xi)}{p(0)} \left[1 - \left(\frac{p(\xi)}{p(0)} \right)^y \right]^{1/2} \left(\frac{r_w(\xi)}{L} \right)^2 d\xi$$

For various geometries analyzed, the pressure distribution (invariant for a fixed geometry as was noted in the previous section) and the geometrical characteristic $[r_w/L(\xi)]$ were obtained from results of computer solutions. $I_1(\xi)$ was then evaluated for the cases analyzed. These results appear along with the polynomial expressions for $I_1(\xi)$ later in this section. The uncoupled convective flux distribution for the boundary layer component (Eq. 2) may now be written as an algebraic expression in terms of the evaluated function, $I_1(\xi)$, (substituting $R_N = L$ for the characteristics length in the expressions):

$$\left. \frac{q_c(\xi)}{q_c(0)} \right|_{\text{B.L.}} = \frac{1}{2} \frac{F(\beta, t_E)}{\sqrt{\left. \frac{d(u_e/u_\infty)}{d(r_w/R_N)} \right|_{\theta=0}}} \frac{\frac{p(\xi)}{p(0)} \left[1 - \left(\frac{p(\xi)}{p(0)} \right)^y \right]^{1/2} \frac{r_w}{R_N}}{\sqrt{I_1(\xi)}} \quad (4)$$

The validity of the similarity solution, applied to the present analysis may be inferred from Fig. 5 which shows the integrated dimensionless boundary layer solution results (Eq. 3) compared to those obtained from the corresponding numerical solutions for several cases. Deviation is a maximum at large distances from the stagnation point (approximately 3 nose radii along the surface). This deviation is due to inaccuracies in the viscous shock layer solutions. Because of these inaccuracies, the viscous shock layer solution is used only to evaluate the convective coupling defect term in Eq. (1).

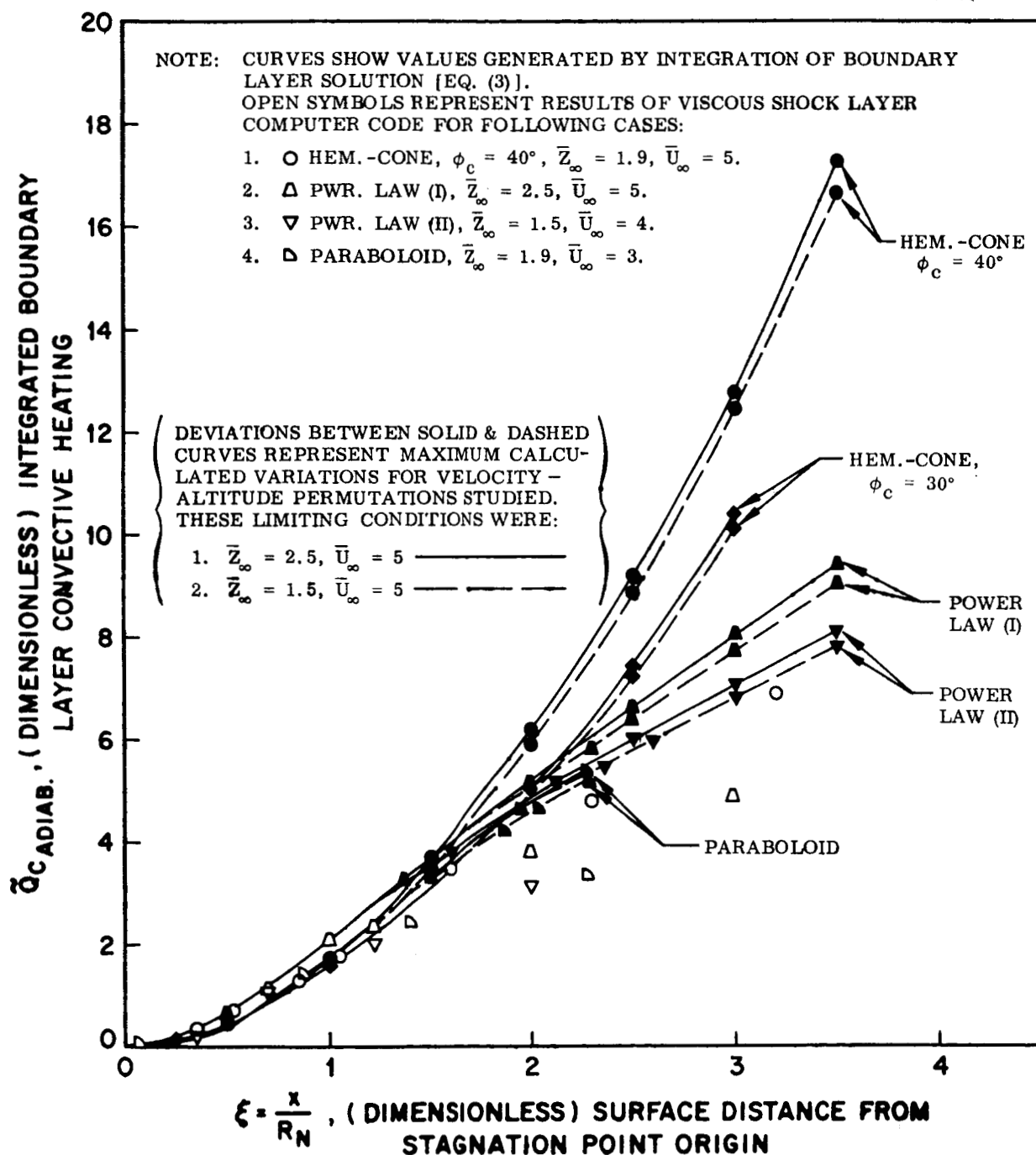


Fig. 5 Boundary Layer Convection Solutions (Adiabatic Shock Layer) for Geometries Analyzed

The convection coupling defect (the second term in Eq. 1.) correlates with the pressure distribution showing a strong dependence on the radiation loss parameter, Γ , and a weaker dependence on the nose radius of curvature, R_N . The correlation equation for the distribution of the coupling defect is:

$$\Delta q_c(\xi) = \Gamma^N \tilde{R}^M \cdot 2.54 \times 10^{-2} \exp \left[3.50 \left(\frac{p(\xi)}{p(0)} \right)^{1/2} \right]$$

$$\tilde{R} = \left(\frac{R_N}{0.5 \text{ ft}} \right), \quad N = 0.758, \quad M = 0.0653 \quad (5)$$

The comparative behavior of the analytic expression for $\Delta q_c(\xi)$ is indicated in Fig. 6 which shows the analytic expression in superposition with the results of representative digital computer solutions. The independent variable is the pressure distribution with the dependent variable showing reasonable general agreement with the data throughout and collapsing to a common value (0.83) at the stagnation point. The functional behavior of the hemisphere cones is seen to break down at the geometrical transition between hemisphere and conical portions (indicated as the start of a separate correlation on the Figure).

Fig. 6 is of particular interest since it also displays the degree of convective coupling along the surface through the coupling defect, Δq_c , which may be recovered from the figure for a case of interest by multiplying the ordinate values by the product, $\Gamma^N \tilde{R}^M$.

In the case of hemisphere-cones for regions beyond $\xi = \xi_T$ (tangent cone), a separate correlation equation must be applied. This correlation is represented by the function $g_1(\phi_c, \xi)$, given by:

$$g_1 = \left[\frac{\Delta q_c(\xi_T)}{\Gamma^N \tilde{R}^M} \right] \left[\exp(-A_1(\xi - \xi_T)^{v_1}) \right] \quad (6)$$

$$\text{with, } A_1 = 1.148, v_1 = 0.867, \quad \frac{\Delta q_c(\xi_T)}{\Gamma^N \tilde{R}^M} = 0.230 \quad (\text{For } \phi_c = 40^\circ)$$

$$A_1 = 1.231, v_1 = 0.316, \quad \frac{\Delta q_c(\xi_T)}{\Gamma^N \tilde{R}^M} = 0.144 \quad (\text{For } \phi_c = 30^\circ)$$

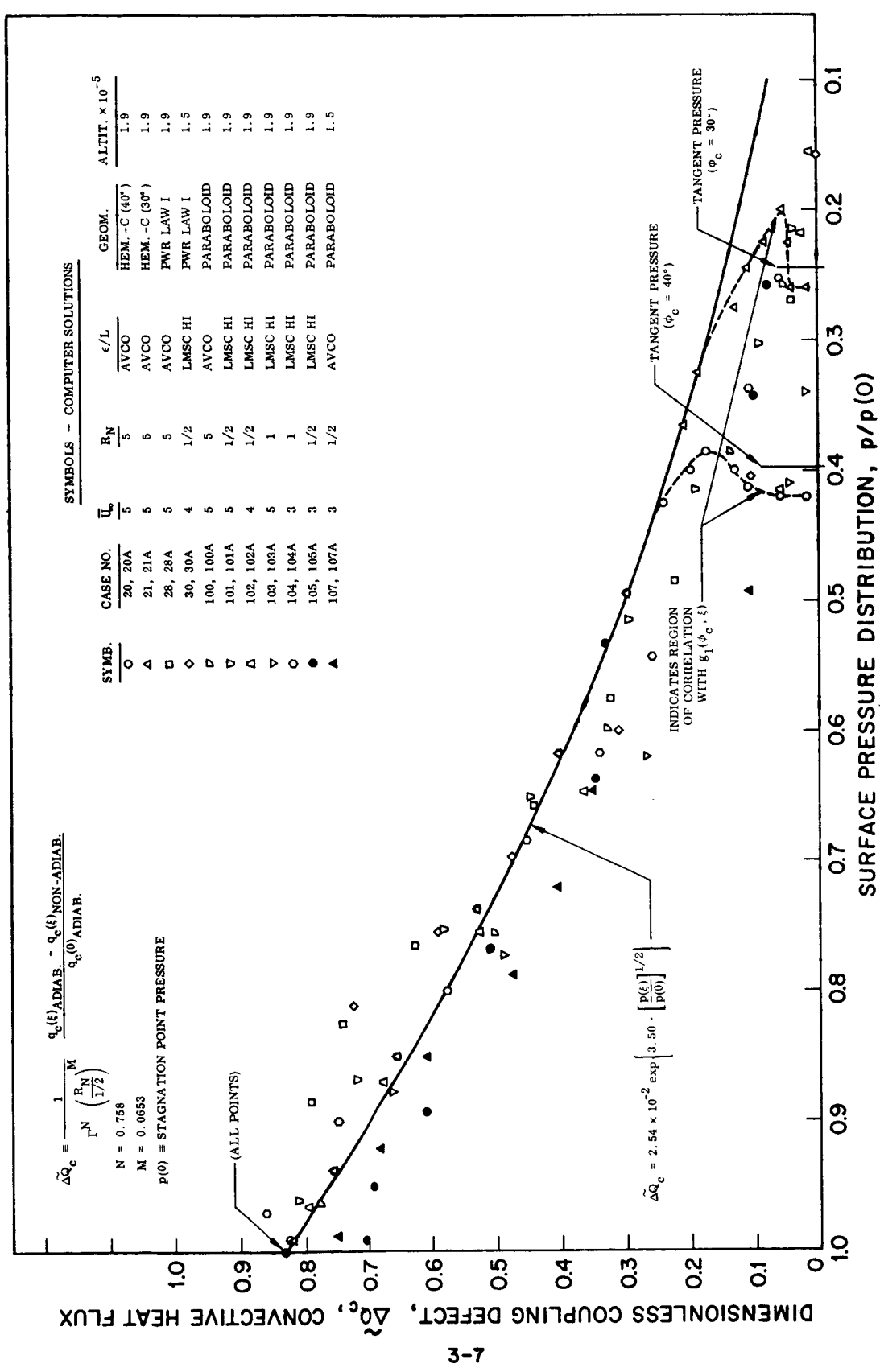


Fig. 6 Correlation of Convective Heat Flux Coupling Defect With Pressure Distribution

Fig. 7 shows the behavior of Eq. (6) applied to the cases depicted and compared with numerical results from the computer code. In general, where comparisons are made with computer results, the table of symbols appearing on the figure yields information about the flow conditions, etc. The nose radius, R_N , always has dimensions of ft. A further symbolism used frequently in the figures is the dimensionless altitude, \bar{z}_∞ , which designated the altitude for the case divided by 10^5 ft. In a similar way, the free stream velocity is commonly identified by the term, \bar{u}_∞ which signifies the velocity magnitude divided by 10^4 fps. The good agreement in the conical region for the correlation equations is apparent from the figure. Also shown on Fig. 7 is the companion correlation, $g_2(\xi)$, used for the radiation flux correlation in the conical region. This will be discussed in a later section, however, it should be noted that the same general level of agreement has been obtained for both g_1 and g_2 functions applied to the hemisphere-cone cases analyzed.

3.1.2 Integration of Convective Correlation Equations Over Surface Area

The correlation equations are next used to evaluate the total heating (integrated over surface area) for the geometries analyzed in the present study. (For reference, these geometrical profiles discussed in Section 2, are shown in Fig. 4). A review of the correlation equations indicates that their functional dependence on pressure distribution (hence, implicitly only a function of geometry in hypersonic flow) and the geometrical characteristics $(r_w(\xi)/L)$, ξ , permit separation of the flow conditions and geometrical characteristics.

The integration of the heating over the surface area element can thus be conducted separately for particular geometries using the appropriate non-dimensional correlation function. This leaves only an algebraic term to be computed separately, based on entry conditions. The product of this term and the correlation integral yield the total heating at arbitrary surface distances for arbitrary entry conditions. The procedure adopted generalizes the relations so that maximum utility results for calculations of arbitrary flow conditions.

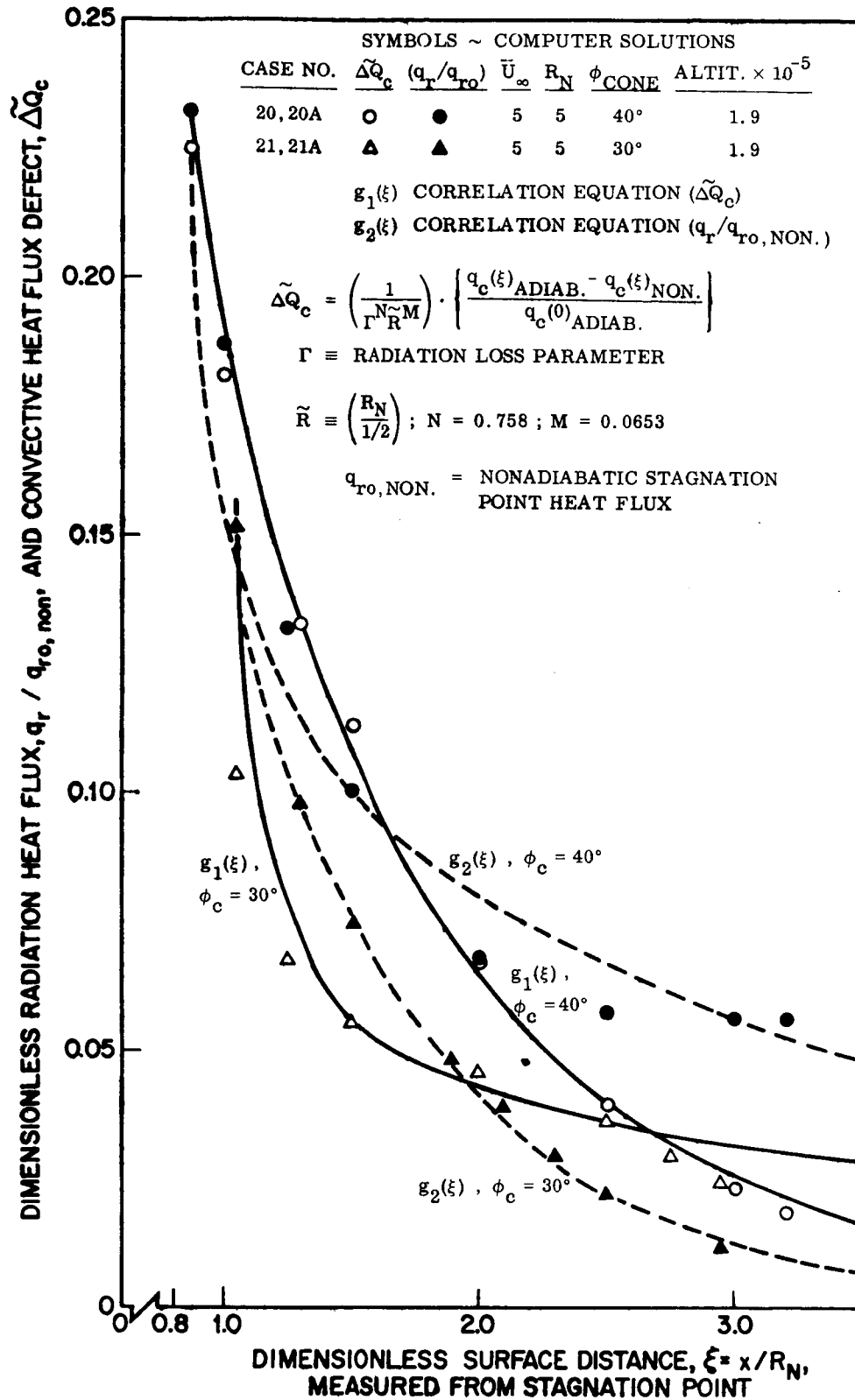


Fig. 7 Conical Surface Correlations of Heat Flux
Components-Hemisphere Cones

Further note should be taken that alternate geometries may be similarly treated based on the correlations presented. Thus, if a configuration is geometrically similar to one of those presented here, the necessary distribution variable (pressure) may be obtained from Fig. 1. For dissimilar geometries, the dependence on surface pressure distribution is convenient since this quantity is comparatively easy to obtain. Once the pressure distribution is known for a specific geometry of interest the correlation equations may be applied to determine the heat flux or, if desired, integrated numerically over surface area.

The convective heat flux distribution equations may be summarized using Eq. (1), (4), (5), and (6). For hemisphere-cones (cone frustum semi angles = 40° , 30°):

$$\begin{aligned} \frac{q_c(\xi)}{q_c(o)} \frac{\text{Non-Adia.}}{\text{Adia.}} &= C_0(U_\infty, Z_\infty) \cdot \frac{p(\xi)}{p(o)} \left[1 - \left\{ \frac{p(\xi)}{p(o)} \right\}^y \right]^{1/2} \cdot \frac{r_w(\xi)}{L} [2I_1(\xi)]^{1/2} \\ &- 2.54 \times 10^{-2} \Gamma^N \tilde{R}^M \exp \left\{ 3.50 \left(\frac{p(\xi)}{p(o)} \right)^{1/2} \right\} \bigg|_{\xi=0}^{\xi=\xi_T} \\ &- \Gamma^N \tilde{R}^M \Delta \tilde{q}_{C_T} \exp \left\{ - A_1 (\xi - \xi_T)^{v_1} \right\} \bigg|_{\xi=\xi_T}^{\xi=\xi_{\text{Final}}} \end{aligned} \quad (7)$$

Eq. (7) can also be applied to the continuous profiles analyzed (paraboloids, power laws) by omitting the final term on the RHS (i.e. evaluating the second term throughout the range of interest). For reference, the coefficients in Eq. (7) are listed below:

$$C_0(v_\infty, z_\infty) = \frac{F(\beta, t_E)}{\sqrt{2 \left\{ \frac{d(u_e/u_\infty)}{d(r_w/L)} \right\}_{\theta=0}}}$$

where the function, F , (near unity in the present analysis) may be determined from Cohen (Ref. 10) p. 32, the thermodynamic and transport properties evaluated at the stagnation point conditions are available in tables, see for example Marrone (Ref. 6), Peng & Pindroh (Ref. 11). The stagnation point velocity gradient may be evaluated from simple approximations, Lees (Ref. 9) or from analytical studies, Vinokur (Ref. 12), or from numerical results obtained independently. In the present analysis the following values were determined for the other coefficients:

$$\begin{aligned} y &= 0.130 \\ N &= 0.758 \\ M &= 0.0653 \end{aligned}$$

and for the function $g_1(\phi_c, \xi)$

	Δq_{C_T}	A_1	ξ_T	v_1
$\phi_c = 40^\circ$	0.230	1.148	0.873	0.867
$\phi_c = 30^\circ$	0.144	1.231	1.048	0.316

Integration of the convection equations over the surface area leads to the following relation for the total convective heating in terms of integrals which have been evaluated for presentation in this section.

$$\begin{aligned} \tilde{Q}_c &= \frac{1}{R_N^2} \int_{\text{Area}} \frac{q_c(\xi)}{q_c(0)} \frac{\text{Non-Adia.}}{\text{Adia.}} dA = 2\pi\sqrt{2} C_0(U_\infty, Z_\infty) \sqrt{I_1(\xi)} \bigg|_{\xi=0}^{\xi=\xi_{\text{Final}}} \\ &\quad - 5.08 \times 10^{-2} \pi \Gamma^N \tilde{R}^M I_2(\xi) \bigg|_{\xi=0}^{\xi=\xi_T} \\ &\quad - 2\pi \Gamma^N \tilde{R}^M I_3(\xi) \bigg|_{\xi=\xi_T}^{\xi=\xi_{\text{Final}}} \end{aligned} \quad (8)$$

In direct analogy to the equation for the heat flux, the last term in Eq. (8) is only used for the hemisphere cones. It is dropped for the paraboloids and power-law geometries with the evaluation continuous over the second term from $\xi = 0$ to $\xi = \xi_{\text{Final}}$.

The evaluated integrals (I_1, I_2, I_3) for arbitrary surface distance, ξ , may be obtained from the accompanying graphs (Figs. (8), (9), (10), (11), (12)) for the appropriate geometries listed on the figures. Also shown on the figures are results of trial fits of the integrals to 3rd and 4th degree polynomials of the general form:

$$f(\xi) = A + B\xi + C\xi^2 + D\xi^3 + E\xi^4 \quad (9)$$

The residual error is noted on the face of the graph for the pertinent function. In general, the 3rd degree polynomials yield satisfactory accuracy in comparison to the results of the 4th degree fits. Hence, if using the polynomial equations for the integrals to evaluate the total heating from Eq. (8), the simpler cubic form of Eq. (9) is recommended. The difference between the accuracy of the 3rd and 4th degree fits may be inferred from the accumulated residual error listed on the figures or the % error over the range of integration listed in Table 2 with the polynomial coefficients.

3.1.3 Systematic Application of Integrated Convective Heating Over Range of Analysis

In order to study the effects of geometrical variations, the total heating was evaluated, using Eq. (9) over the surface distance from the stagnation point, back for 3 or more nose radii. This was accomplished for each of the 5 basic geometries at altitudes of 250, 190, and 150 kft and entry velocities of 50, 40, and 30 kfps.

Since the nose radius of curvature enters the equations as a non-linear contribution to the sum of the terms through the factor, $(R_N/1/2 \text{ ft})^M$ (see Eqs. (7) and (8)), it was not possible to uncouple the dependence on this variable

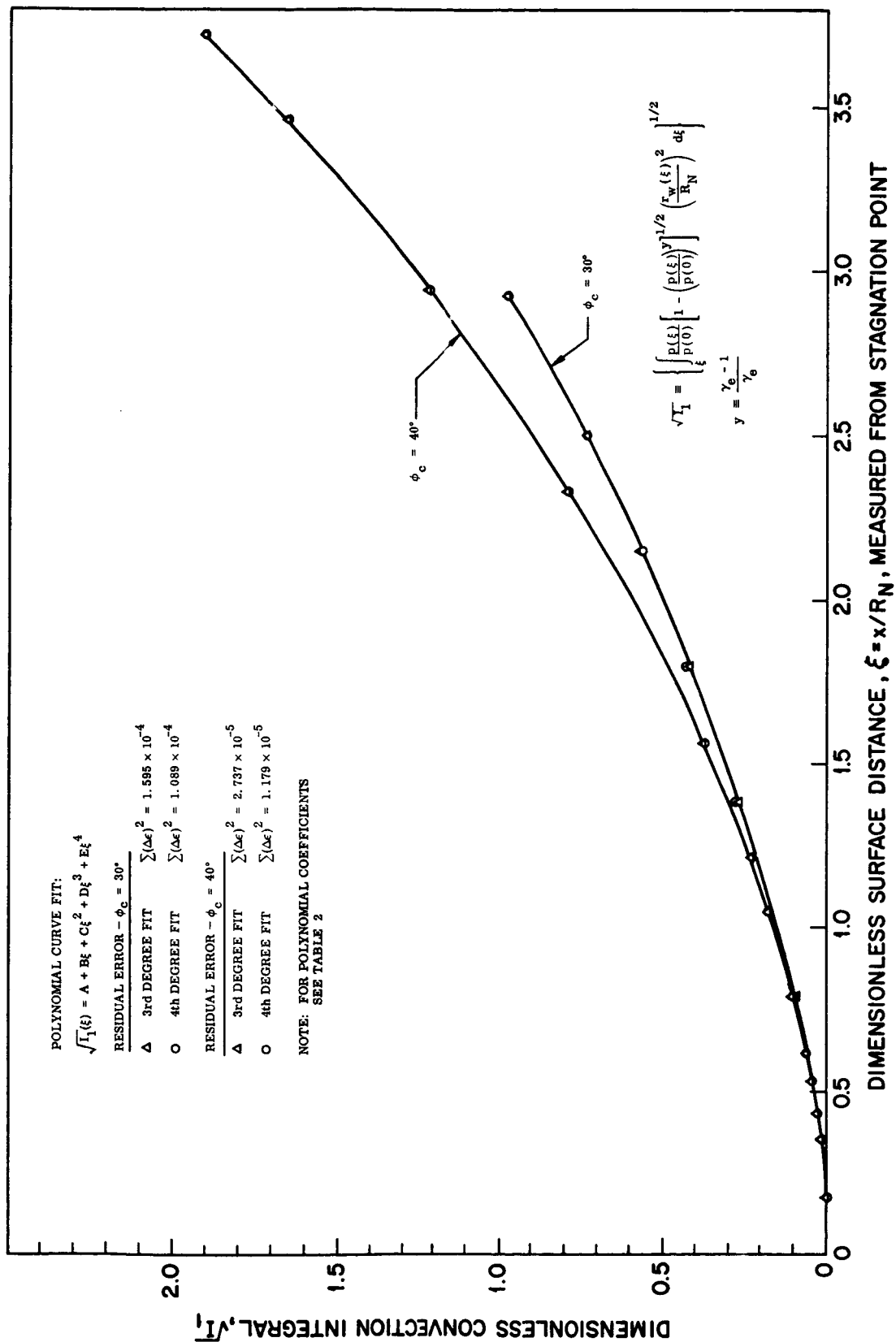
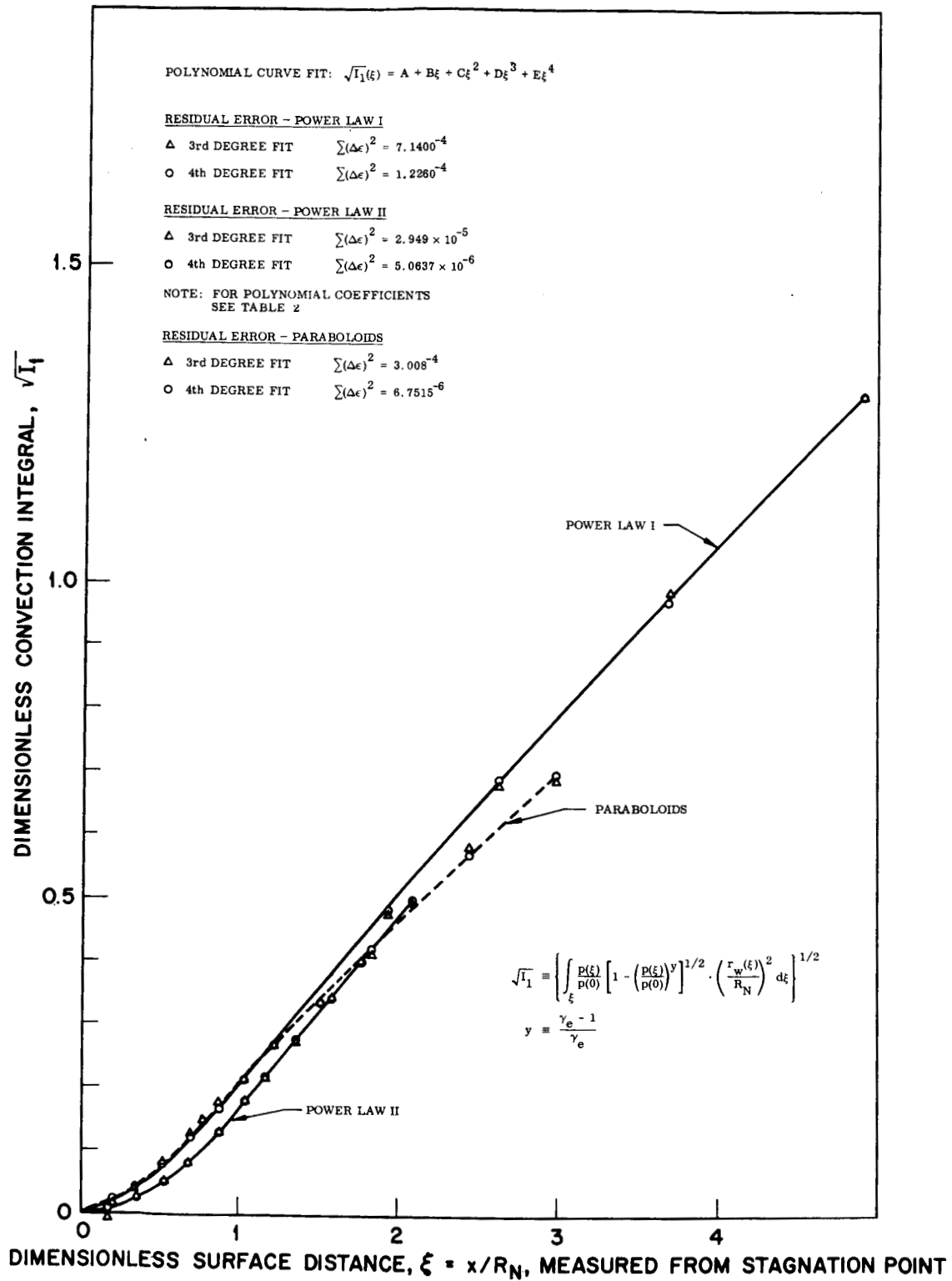


Fig. 8 Dimensionless Convection Integral, $\sqrt{I_1}$ Evaluated for Hemisphere - Cone
 ϕ_c (Cone Frustum 1/2 Angle) = $40^\circ, 30^\circ$

Fig. 9 Dimensionless Convection Integral, $\sqrt{I_1}$, Evaluated for Parabolooids and Power Laws

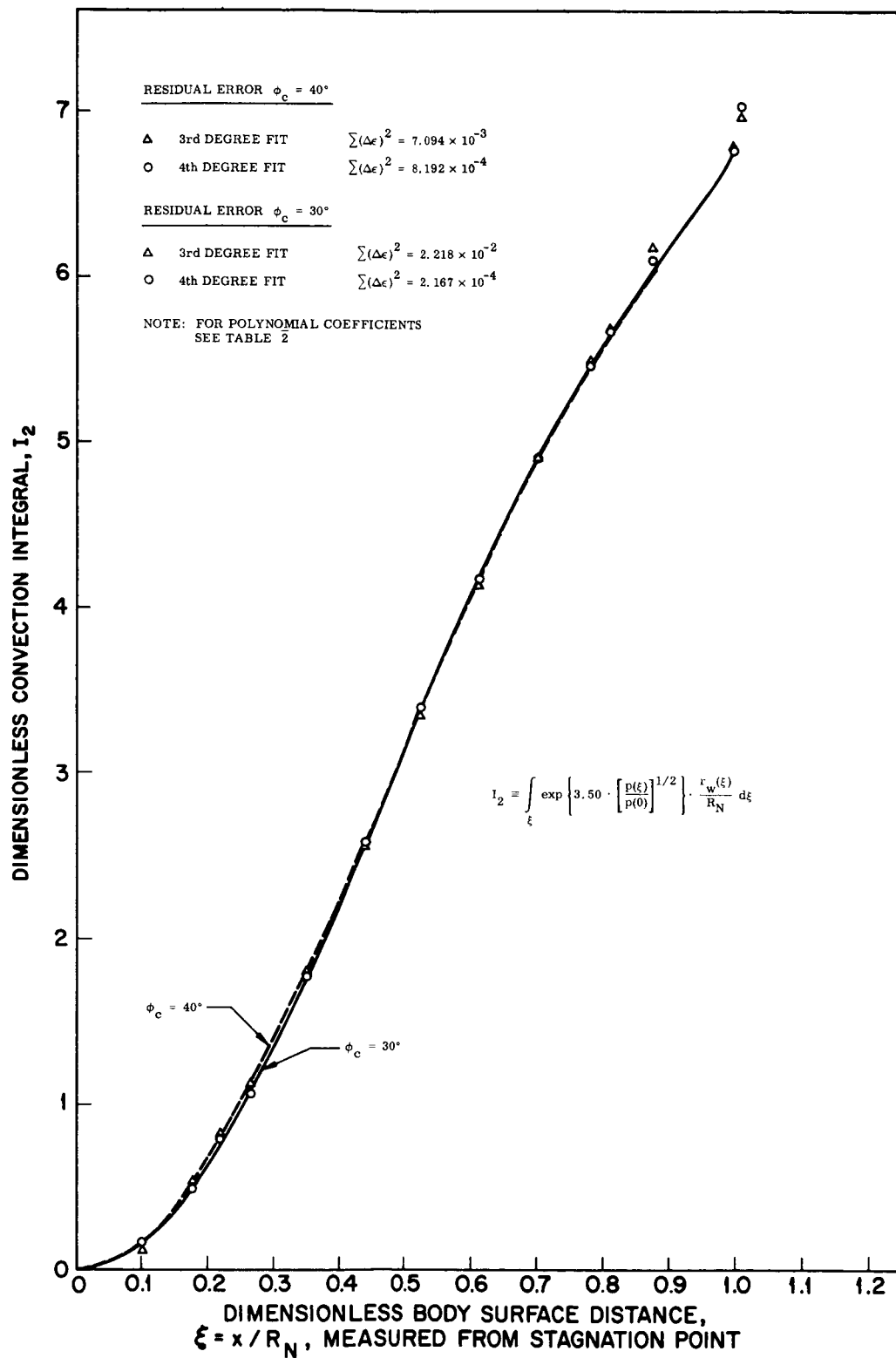
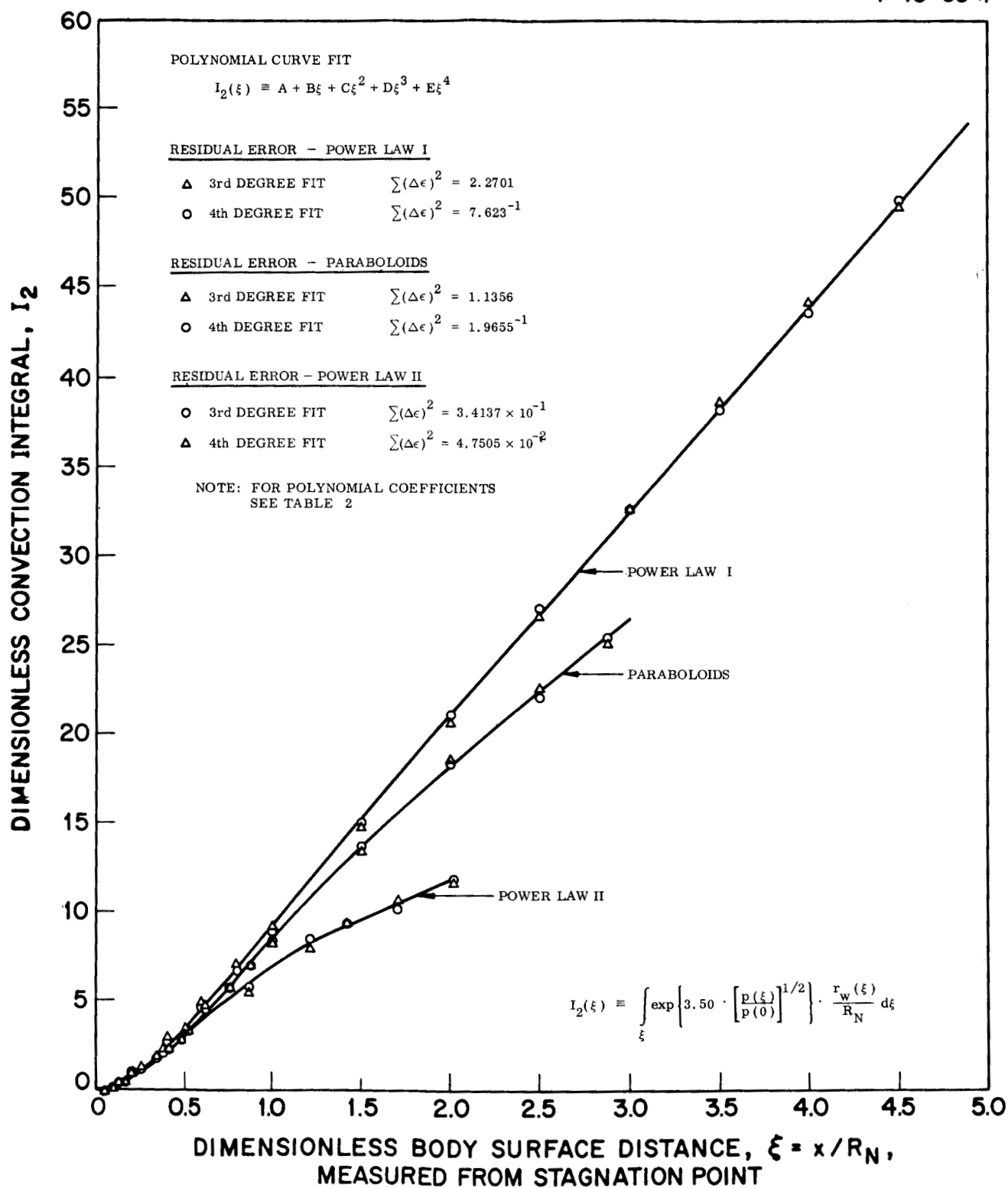


Fig. 10 Dimensionless Convection Integral, I_2 , Evaluated for Hemisphere - Cone
 ϕ_c (1/2 Angle - Cone Frustrum) = $30^\circ, 40^\circ$

Fig. 11 Dimensionless Convection Integral, I_2 , Evaluated for Paraboloids and Power Laws

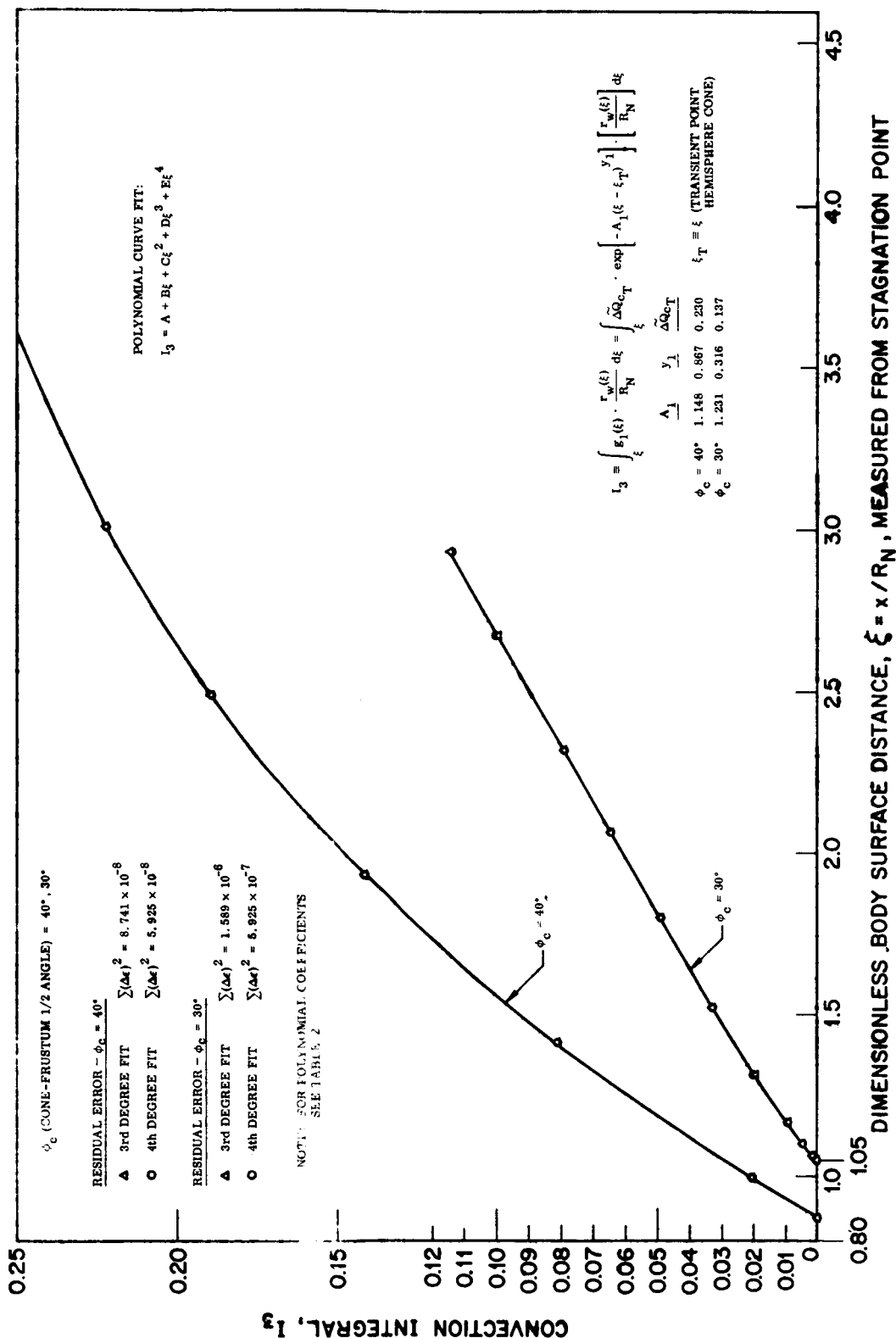
Fig. 12 Convection Integral, I_3 , Conical Surface, Hemisphere-Cone

Table 2

POLYNOMIAL COEFFICIENTS - CONVECTION INTEGRALS (SEE EQUATIONS (8) & (9)).
 POLYNOMIAL EQUATION OF THE FORM: $f(\xi) = A + B\xi + C\xi^2 + D\xi^3 + E\xi^4$

Geometry	Integral	Degree	A	B	C	D	E	% Deviation Over Integral Range
Hem.-Cone $\phi_c = 40^\circ$	$\sqrt{I_1}$	3	-1.0701 ⁻²	4.6022 ⁻²	1.3197 ⁻¹	-1.5894 ⁻³	1.4217 ⁻³	1.37 ⁻³
	"	4	-6.0420 ⁻³	2.3086 ⁻²	1.5901 ⁻¹	-1.2552 ⁻²		5.89 ⁻⁴
	I_2	3	-1.443 ⁻¹	1.580	1.501 ⁺¹	-9.961		1.18 ⁻¹
	"	4	9.1337 ⁻²	-1.569	2.779 ⁺¹	-2.9691 ⁺¹	1.0213 ⁺³	1.362 ⁻²
	I_3	3	-1.7937 ⁻¹	2.444 ⁻¹	-4.7415 ⁻²	3.479 ⁻³		3.50 ⁻⁵
	"	4	-1.8245 ⁻¹	2.514 ⁻¹	-5.283 ⁻²	5.1818 ⁻³	-1.8669 ⁻⁴	2.37 ⁻⁵
Hem.-Cone $\phi_c = 30^\circ$	$\sqrt{I_1}$	3	-2.2669 ⁻²	9.8430 ⁻²	7.8505 ⁻²	1.1624 ⁻³		1.59 ⁻²
	"	4	-1.2262 ⁻²	4.368 ⁻²	1.558 ⁻²	-3.7659 ⁻²	6.3055 ⁻³	1.09 ⁻²
	I_2	3	-2.506 ⁻¹	2.505	1.251 ⁺¹	-7.955		3.33 ⁻¹
	"	4	1.148 ⁻¹	-2.001	2.848 ⁺¹	-2.915 ⁺¹	9.333	3.29 ⁻³
	I_3	3						
	"	4						
Paraboloid	$\sqrt{I_1}$	3	-2.562 ⁻²	1.810 ⁻¹	6.482 ⁻²	-1.536 ⁻²		4.30 ⁻²
	"	4	-8.912 ⁻⁴	4.603 ⁻²	2.566 ⁻¹	-1.118 ⁻¹	1.561 ⁻²	9.64 ⁻⁴
	I_2	3	-5.400 ⁻¹	6.939	2.534	-6.283 ⁻¹		4.37
	"	4	-1.577 ⁻¹	3.090	9.617	-4.722	7.277 ⁻¹	7.55 ⁻¹

Table 2 cont'd.

Geometry	Integral	Degree	A	B	C	D	E	% Deviation Over Integral Range
Power- Law I	$\sqrt{I_1}$	3	-4.241^{-2}	2.288^{-1}	2.803^{-2}	-3.924^{-3}		5.50^{-2}
	"	4	-1.888^{-2}	1.361^{-1}	1.173^{-1}	-3.302^{-2}	2.974^{-3}	9.44^{-3}
	I_2	3	-8.821^{-1}	9.056	1.165	-1.509^{-1}		4.20
	"	4	-3.999^{-1}	6.083	4.554	-1.385	1.395^{-1}	1.41
Power- Law II	$\sqrt{I_1}$	3	3.873^{-4}	-2.704^{-2}	2.547^{-1}	-6.182^{-2}		5.90^{-3}
	"	4	6.065^{-3}	-7.429^{-2}	3.495^{-1}	-1.289^{-1}	1.531^{-2}	1.12^{-3}
	I_2	3	-5.482^{-1}	6.809	1.192	-7.883^{-1}		2.84
	"	4	-2.118^{-1}	3.245	9.769	-7.488	1.621	3.97^{-1}

as was the original intent. Hence, to evaluate either the heat flux distribution, Eq. (7), or the total heating, Eq. (8), a specific nose radius of curvature must be selected. For the present applications the results of preliminary studies (see Appendix A) indicated the desirability of nose radii ≤ 1 ft. for minimal heating at superorbital velocities. In keeping with the indicated desirability for small nose radius of curvature, those selected for analysis were 1 ft. and $\frac{1}{2}$ ft. These results are shown in the next set of figures (Figs. 13 through 21).

Each of the figures shows the total convective heating ratioed to the adiabatic, stagnation point heat flux as a function of surface distance, ξ . On each figure results for all of the geometries are superimposed for both nose radii selected, thus affording a direct comparison of the effects of geometry. The results indicate the relatively blunt hemisphere-cone profile ($\phi_c = 40^\circ$) is associated with relatively high total convective heating as is the more oblate analytic profile, (Power Law I). The primary cause of this trend appears to be the restriction in expansion of shock layer flow induced by the presence of the 40° cone frustrum. This effect can be deduced by an inspection of the pressure distributions shown in Fig. 1 which shows clearly the apparent plateau of constant pressure that is reached after the under expansion and recovery in the flow transition region near the juncture between hemisphere and cone. The analytic profiles tend to a more uniform expansion continuing over the entire extent of surface profile analyzed. This is consistent with expectations in consideration of their continuously diminishing body curvature. Particular attention can also be given to the sharp relative reduction for the more slender power law body (Power Law II) as well as the more slender hemisphere-cone ($\phi_c = 30^\circ$). The paraboloid, itself also looks promising from the present convective heating results. The relative total heating for a given surface dimension has greater meaning in design studies if it is examined in conjunction with the volume enclosed by the geometries of interest for various surface lengths. This approach applied to the present studies is discussed and examined for a set of flow conditions in Section 3.3 of this report.

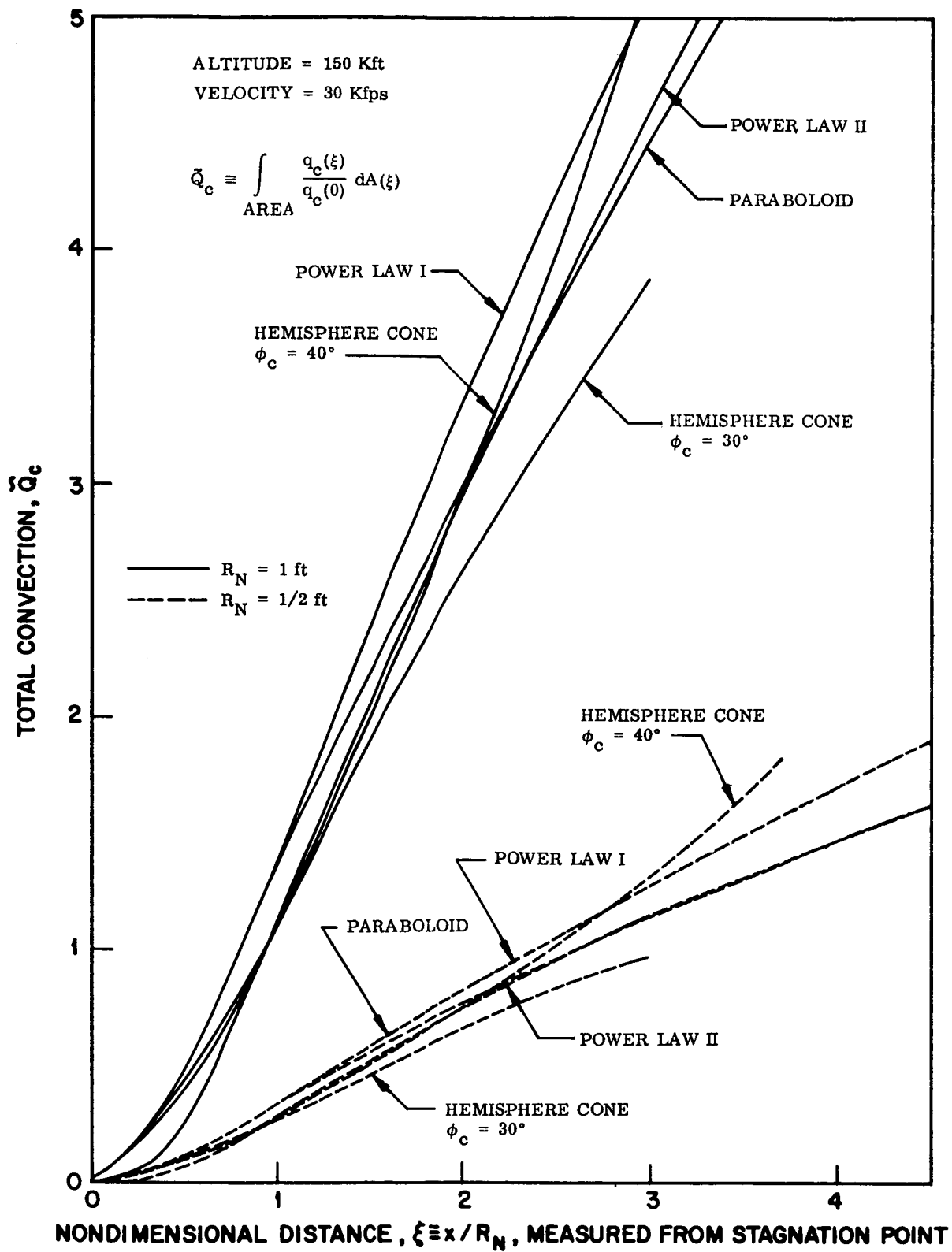


Fig.13 Convection Heating Integrated Over Surface Area

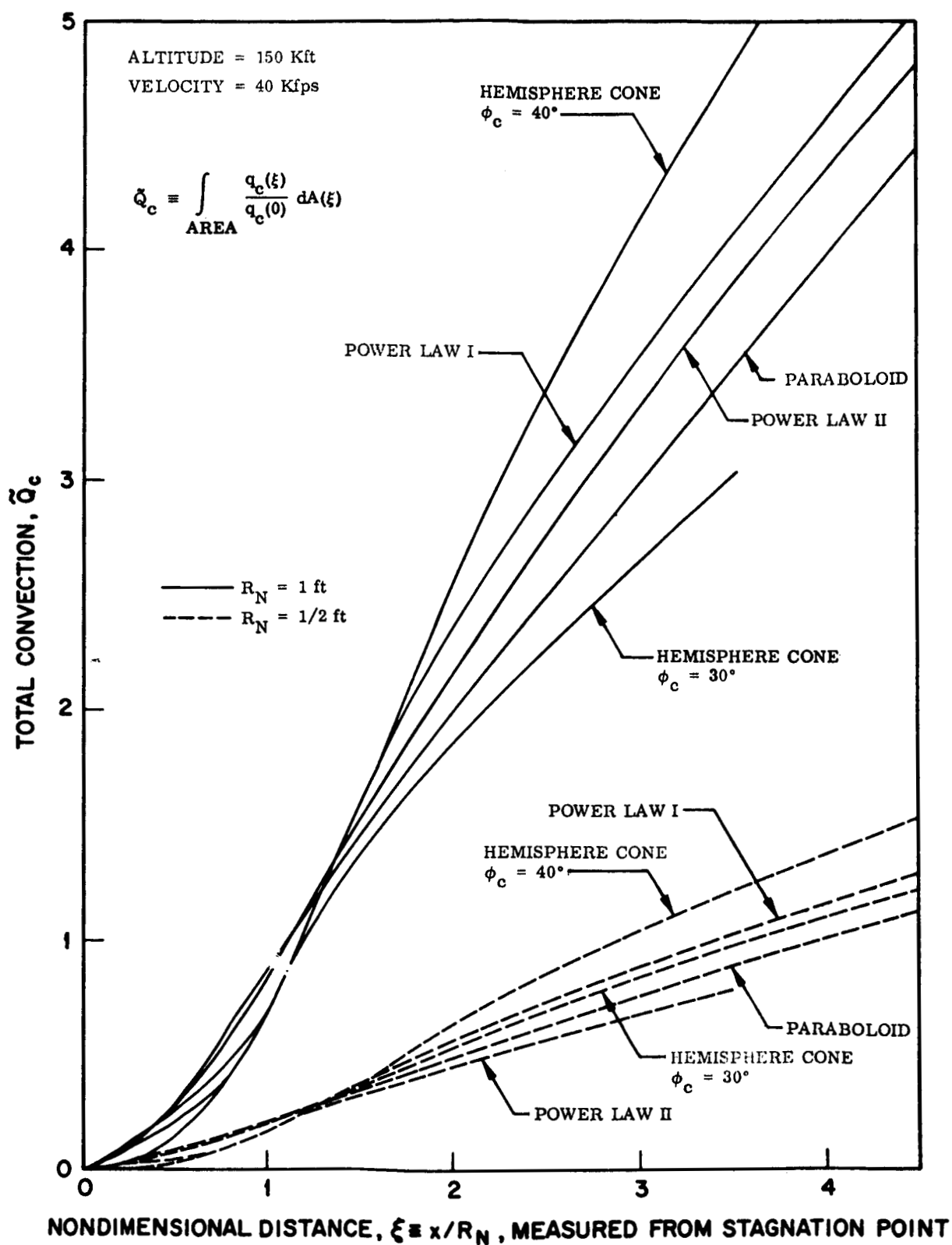


Fig.14 Convective Heating Integrated Over Surface Area

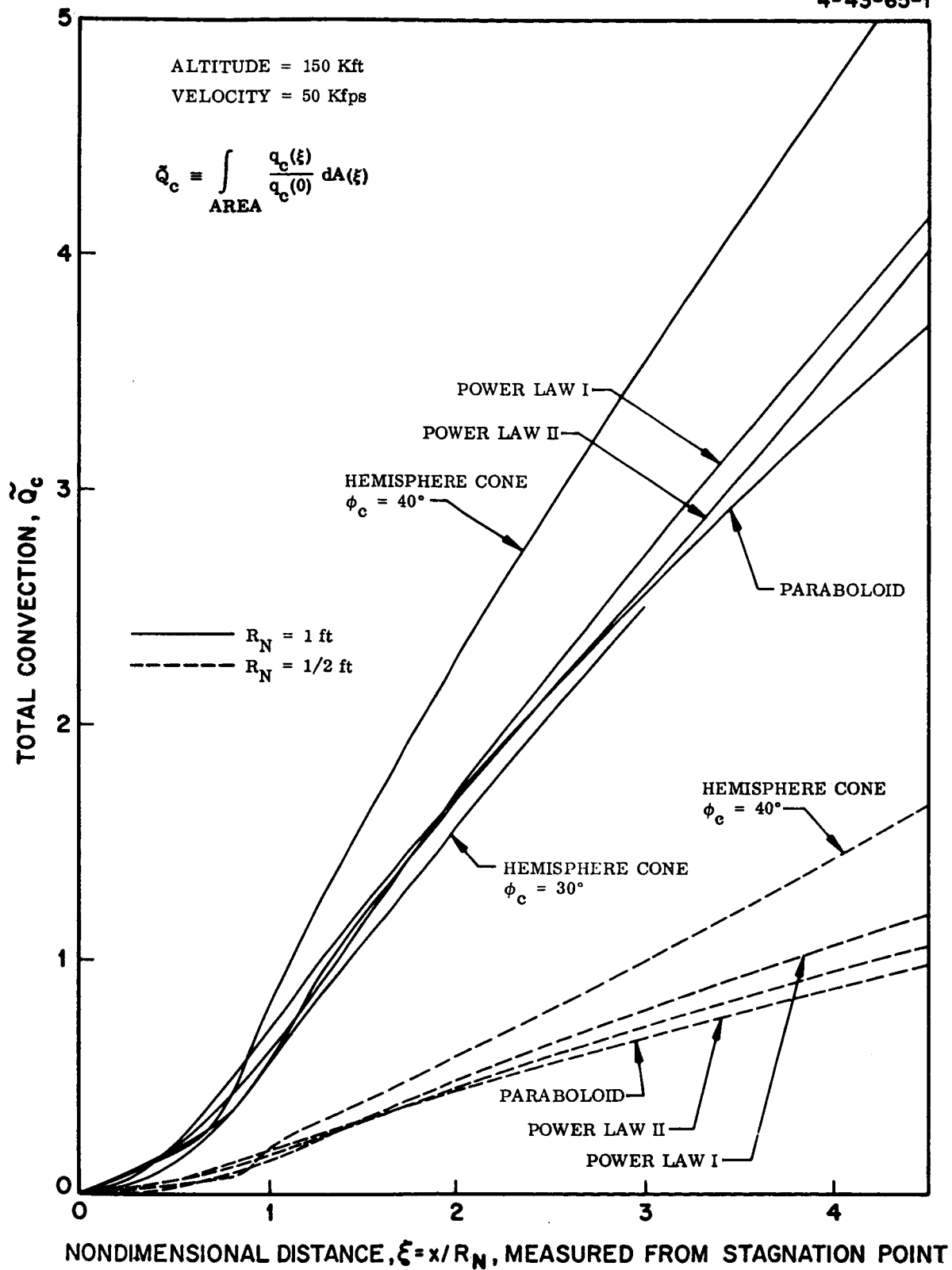


Fig. 15 Convection Heating Integrated Over Surface Area

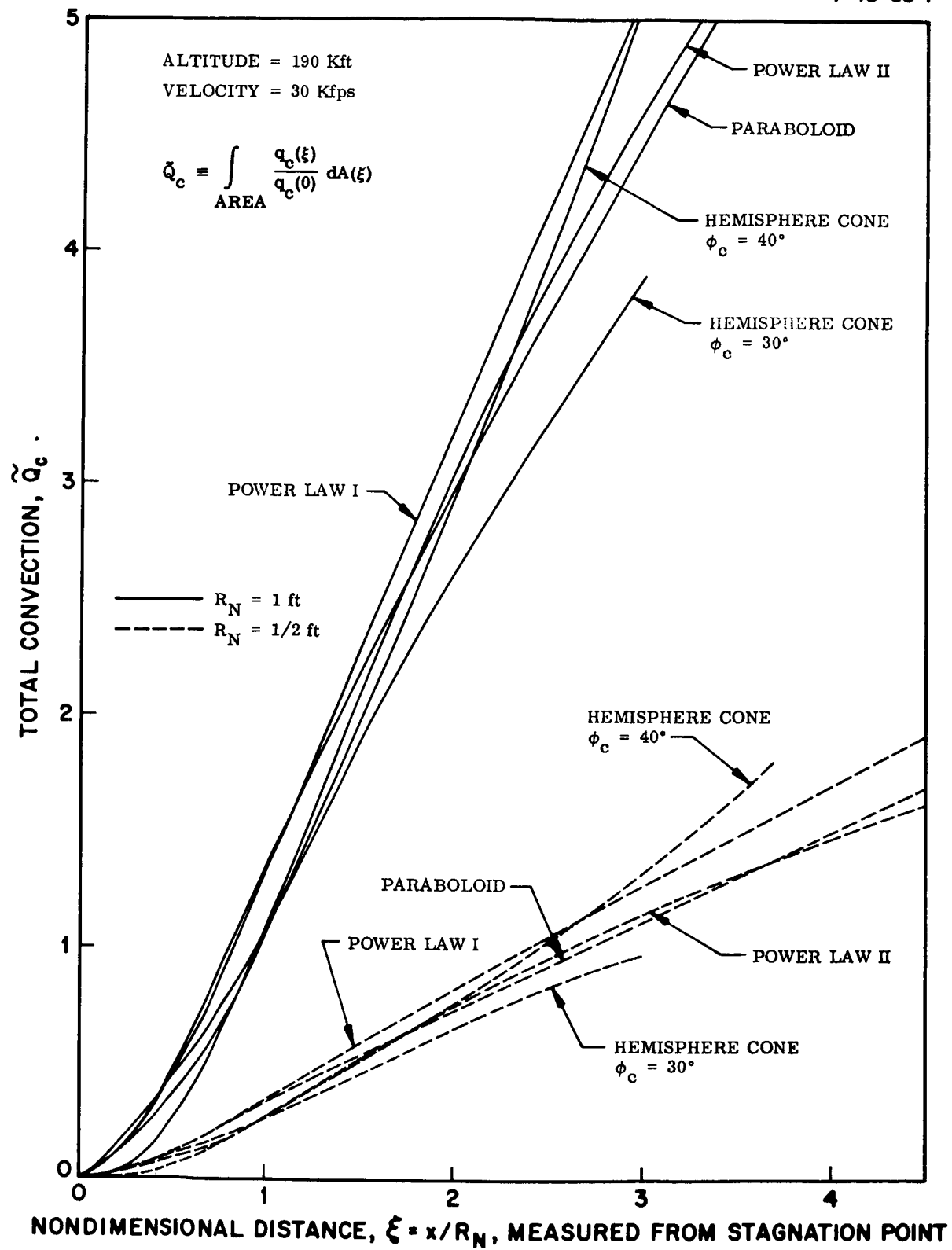


Fig. 16 Convection Heating Integrated Over Surface Area

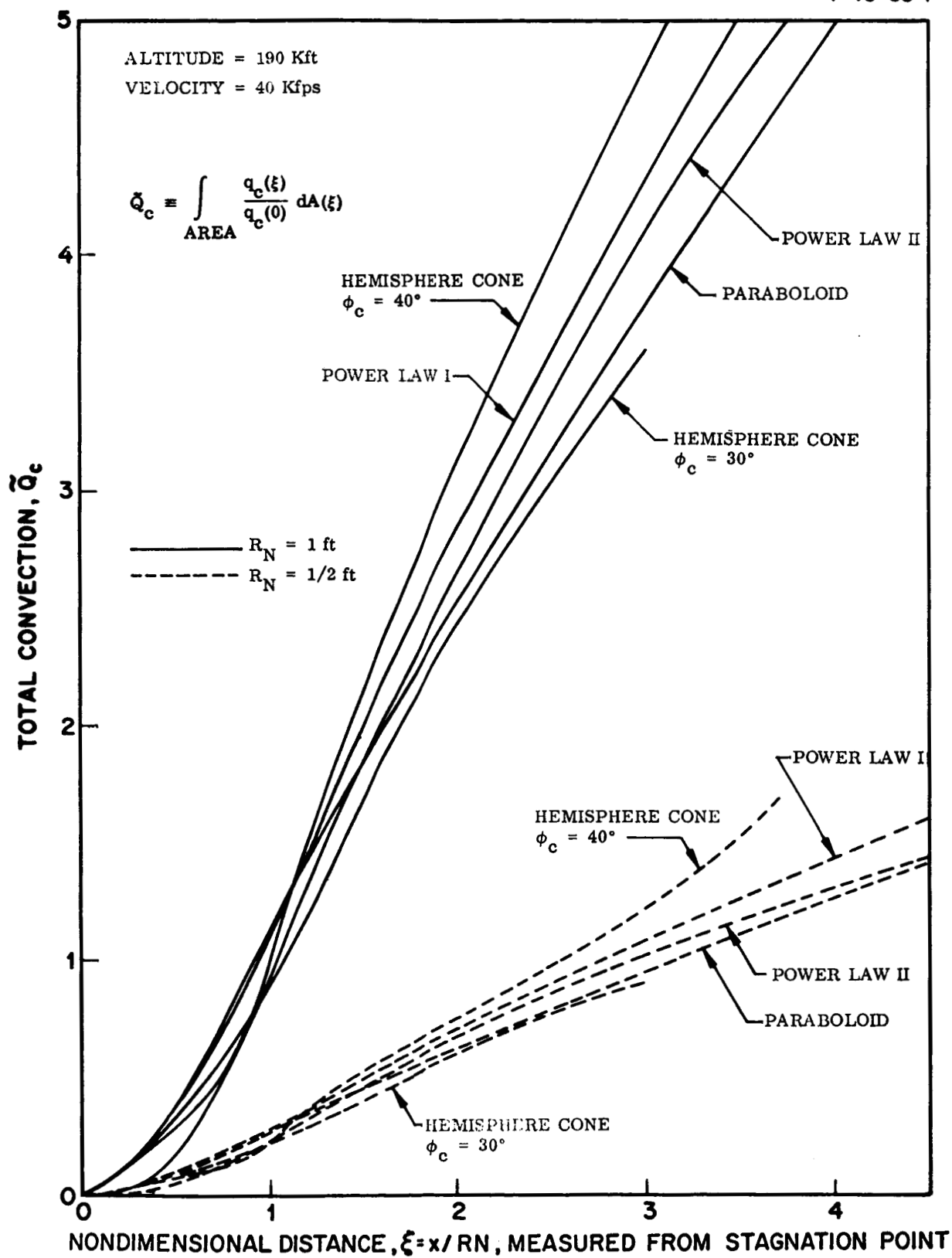


Fig. 17 Convection Heating Integrated Over Surface Area

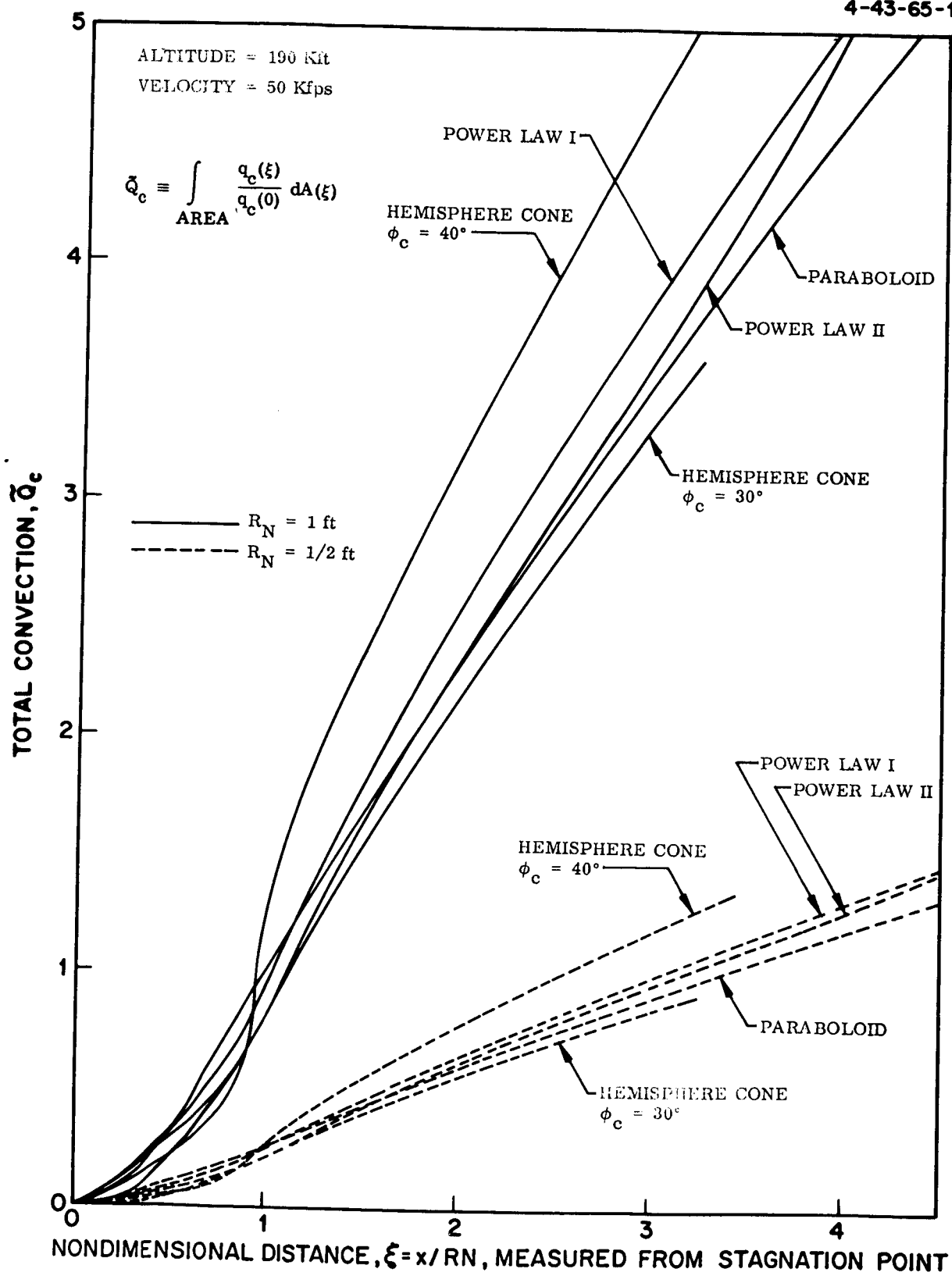


Fig. 18 Convection Heating Integrated Over Surface Area

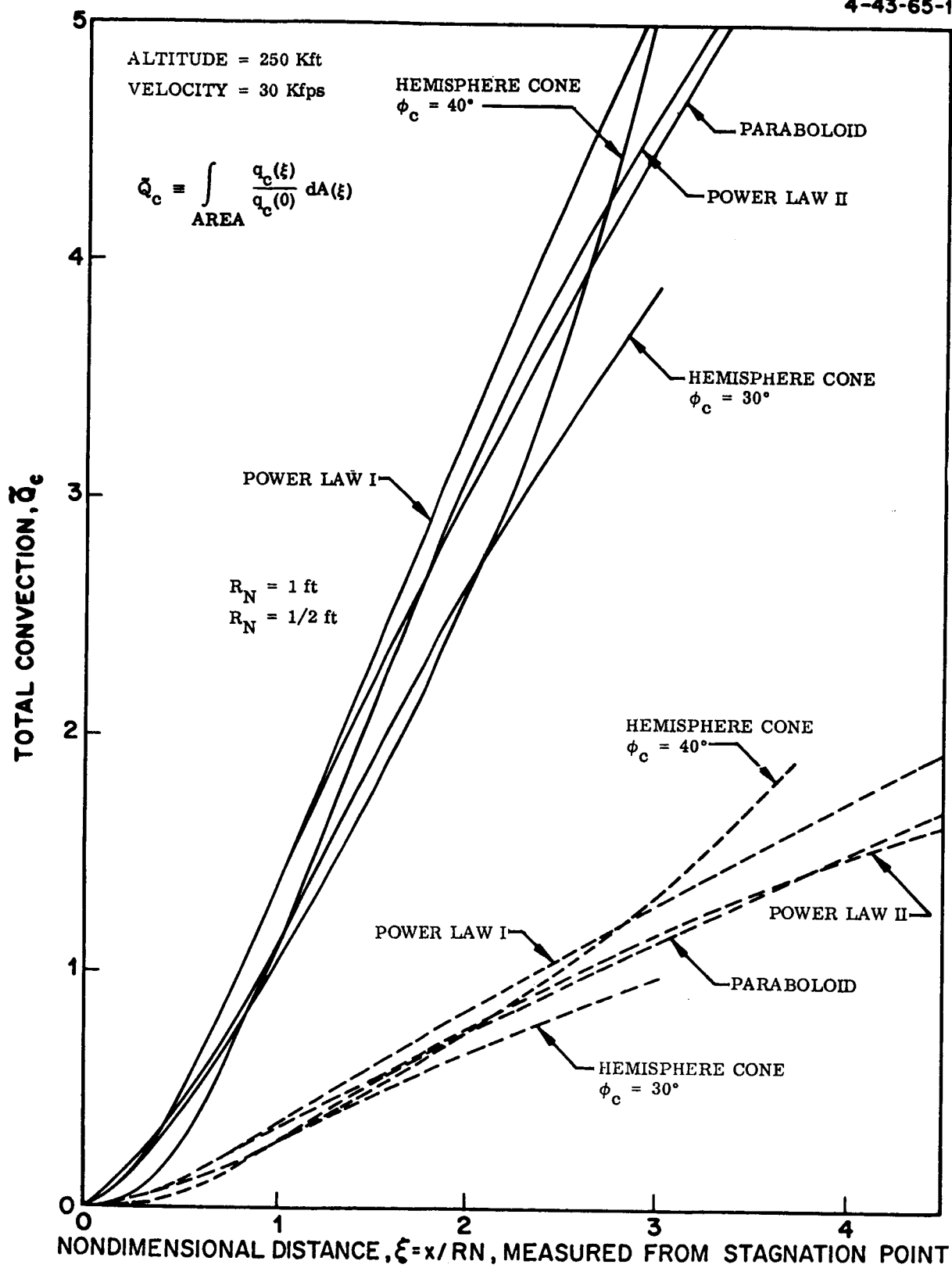


Fig. 19 Convection Heating Integrated Over Surface Area

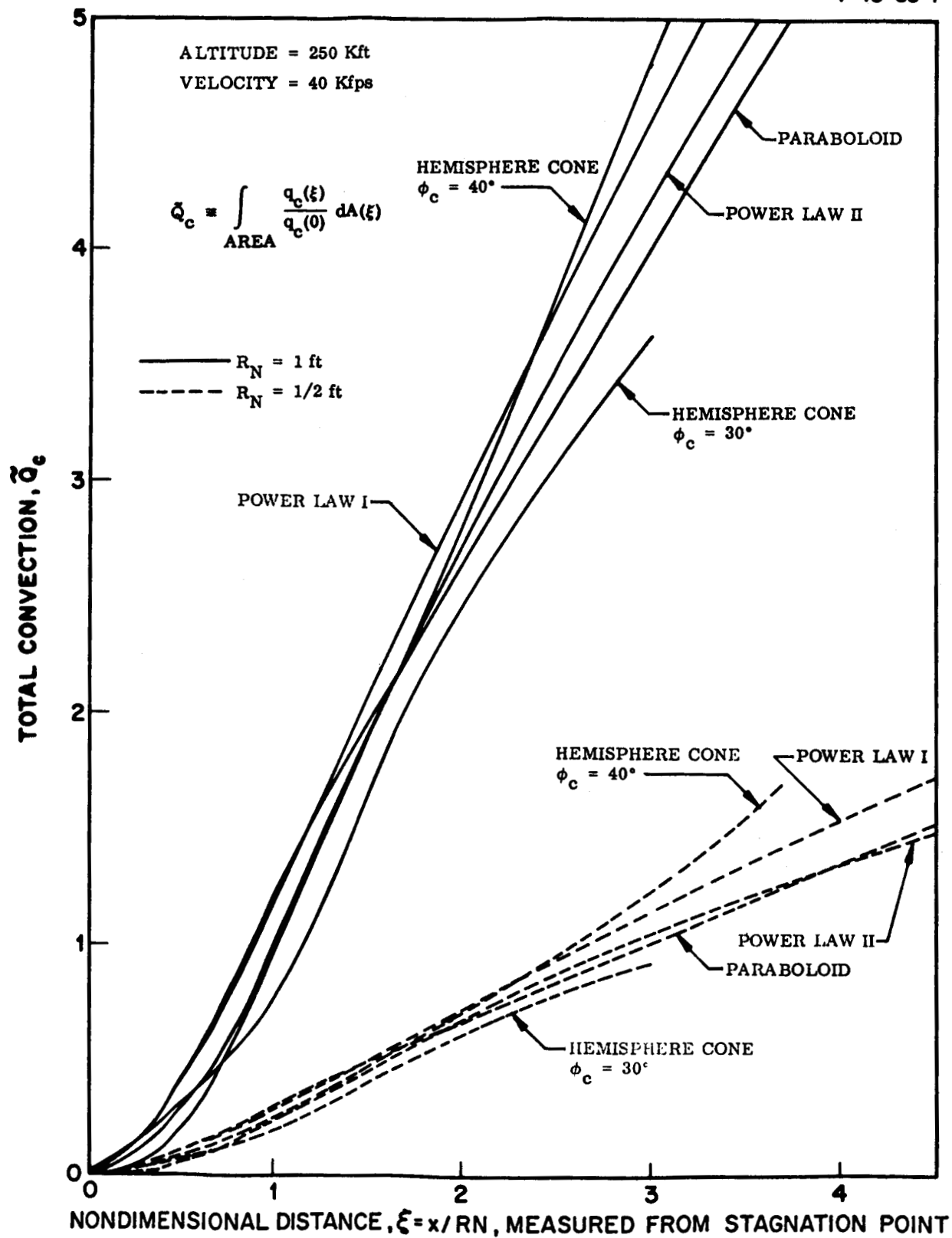


Fig. 20 Convection Heating Integrated Over Surface Area

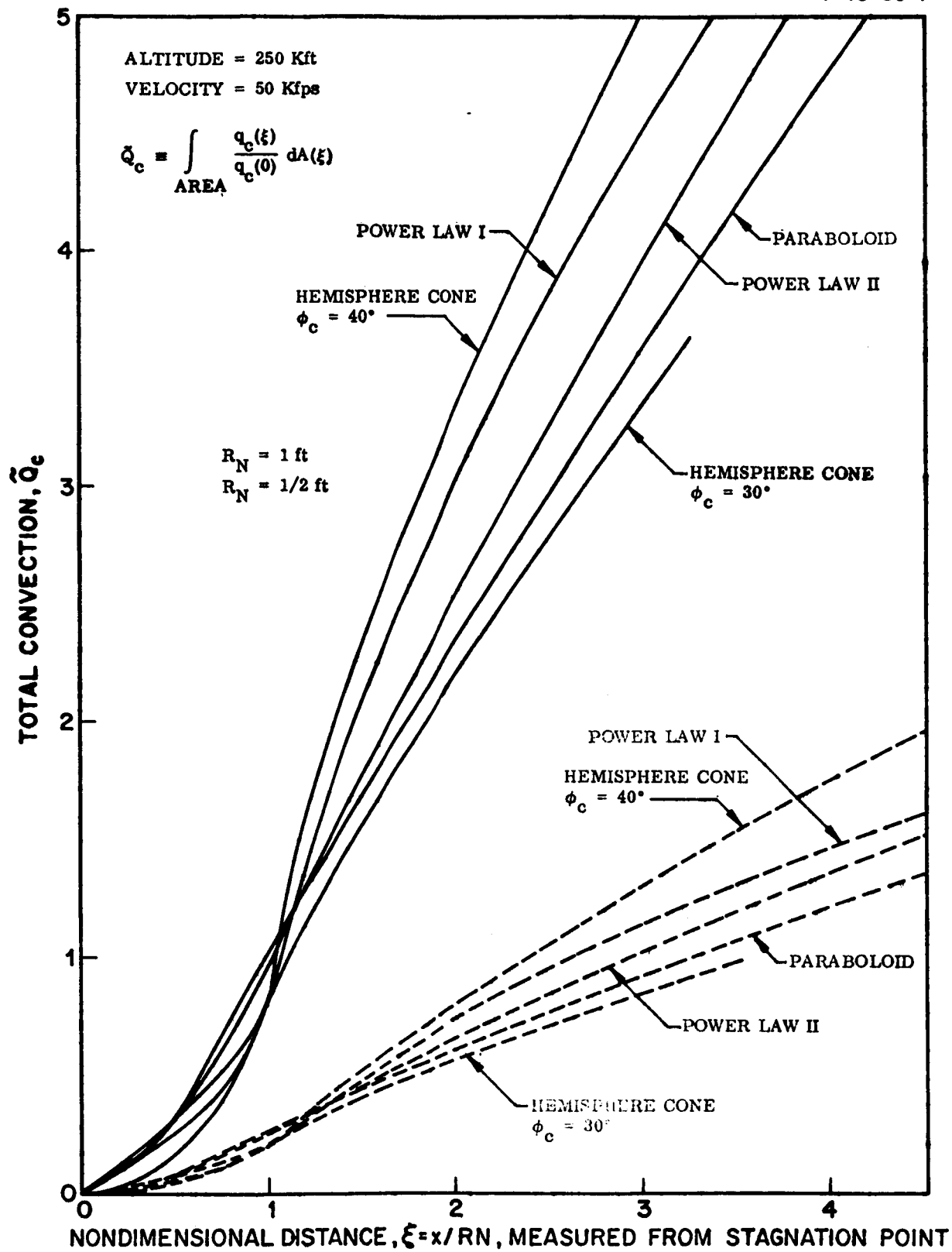


Fig.21 Convection Heating Integrated Over Surface Area

3.2 Radiative Heating

3.2.1 Correlation of Radiative Heat Flux Distribution

The radiative heat flux is diminished by the non-adiabatic loss mechanism in a more direct way than the convective heat flux. The radiative heat flux distribution for the shock layer flow is conveniently expressed as a product of two terms, preparatory to correlation.

$$\frac{q_r(\xi)}{q_r(0)} \bigg|_{\text{Non-Adia}} = \frac{q_r(0)}{q_r(0)} \bigg|_{\text{Adia}} \cdot \frac{q_r(\xi)}{q_r(0)} \bigg|_{\text{Non-Adia}} \quad (10)$$

In Eq. (10) the device of ratioing the results to the adiabatic stagnation point heat flux (available from standard analysis or correlations mentioned previously) has been imposed, in analogy with the convective heat flux distribution, to enhance the utility of the present work. Normalized in this manner the non-adiabatic radiation flux distribution for all cases are correlated with one equation, effectively uncoupling the radiation loss parameter. The radiation loss enters through the term $\frac{q_r(0)_{\text{Non-Adia}}}{q_r(0)_{\text{Adia}}}$, a direct function of the radiation loss parameter, Γ . For a given set of initial conditions (altitude, velocity, nose radius, ϵ/L prediction) Γ is readily computed. Results of calculations are available from previous studies, see Howe (Ref. 5), Hoshizaki (Ref. 1) as well as the present work. Fig. 22 shows the functional behavior of the stagnation point radiation flux ratio as implied by examination of the results. Symbols depict points from numerical solutions at various flow conditions. The general range of Γ in the present analysis may be reviewed in Fig. 2

The second term on the RHS of Eq. (10) is merely the ratio of the radiative heat flux distribution divided by the stagnation point value in a non-adiabatic shock layer. Correlation of this function has been made using the results of the computer code calculations. The correlation equation is:

$$\frac{q_r(\xi)}{q_r(0)} \bigg|_{\text{Non-Adia}} = 2.01 \times 10^{-2} \exp \left[3.90 \left[\frac{p(\xi)}{p(0)} \right]^{1/2} \right] \quad (11)$$

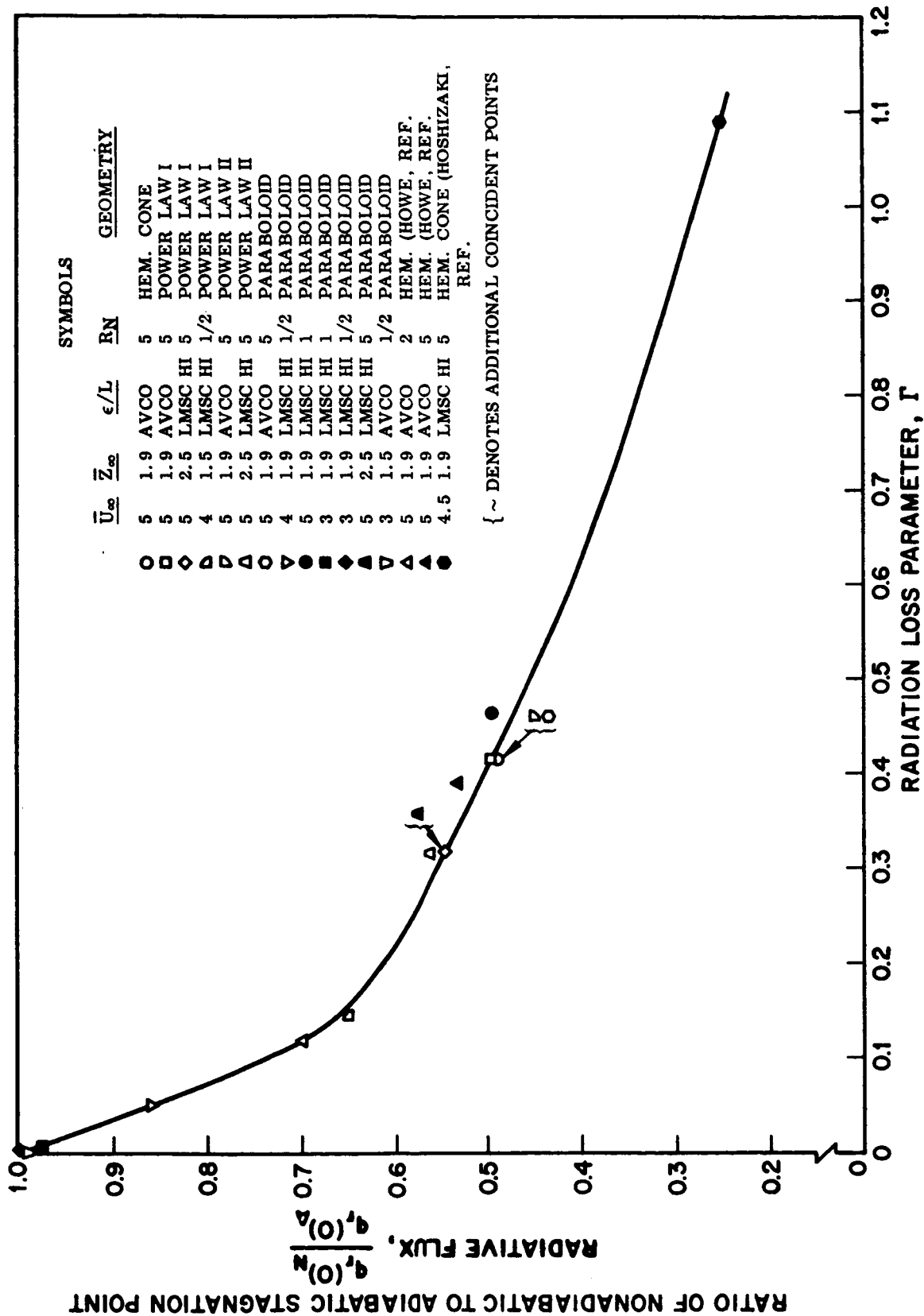


Fig. 22 Reduction in Stagnation Point Radiative Heat Flux as a Function of Radiation Loss Parameter

Again, the basic correlation with pressure distributions works well as a description of the average functional behavior of the results. The behavior of the correlation equation in comparison to results of the computer code may be seen in Fig. 23. The relatively limited scatter of numerical results around the values given by the analytical solution are not inconsistent with the general accuracy of the solutions. The possibility of a small, systematic variation in distribution resulting from a subtle dependence on radiation loss and nose radius of curvature will be examined when results of the new computer solutions (with self-absorption) are available. Thus far, no such systematic trend in dispersion of points has been detected from the present results.

The behavior of the solutions with respect to correlations in the conical region of the hemisphere-cones may be reviewed from the comparison of the correlation function, $g_2(\phi_c, \xi)$ and code results seen in a previous figure (Fig. 7). The complete radiation heat flux distribution showing the results of both correlations (Eq. (11) and g_2) applied to the hemisphere-cones appear in Fig. 24. The dashed extension for the 40° half angle cone represents the conical flow limiting values computed independently to indicate the apparent trend of the actual distribution at regions far from the nose ($\xi \rightarrow 5$). The comparable extension for the 30° half angle cone tends to vanish to the scale of the values depicted, hence is not shown. Agreement with the present correlation equations is readily apparent from examination of this figure.

The correlation for the conical region applied to the hemisphere-cones where $\xi \geq \xi_T$ is described by the following equation.

$$g_2(\phi_c, \xi) = \frac{q_r(\xi_T)}{q_r(0)} \Big|_{\text{Non-Adia}} \cdot \exp \left[-A_2(\xi - \xi_T)^2 \right] \quad (12)$$

In summary, the correlation equation for the radiative heat flux distribution is (combining Eqs. (10), (11), and (12)):

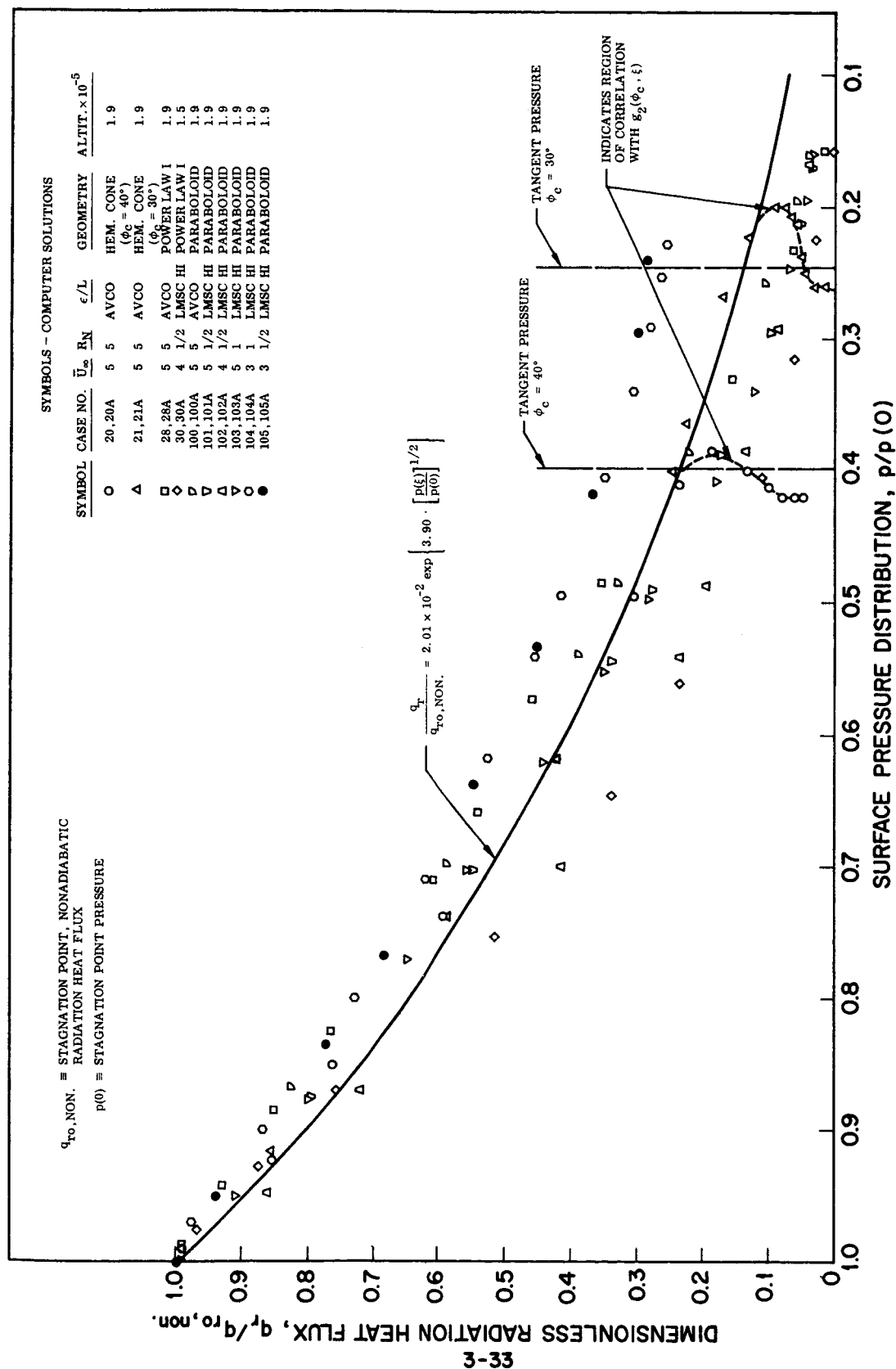


Fig. 23 Correlation of Radiation Heat Flux With Pressure Distribution

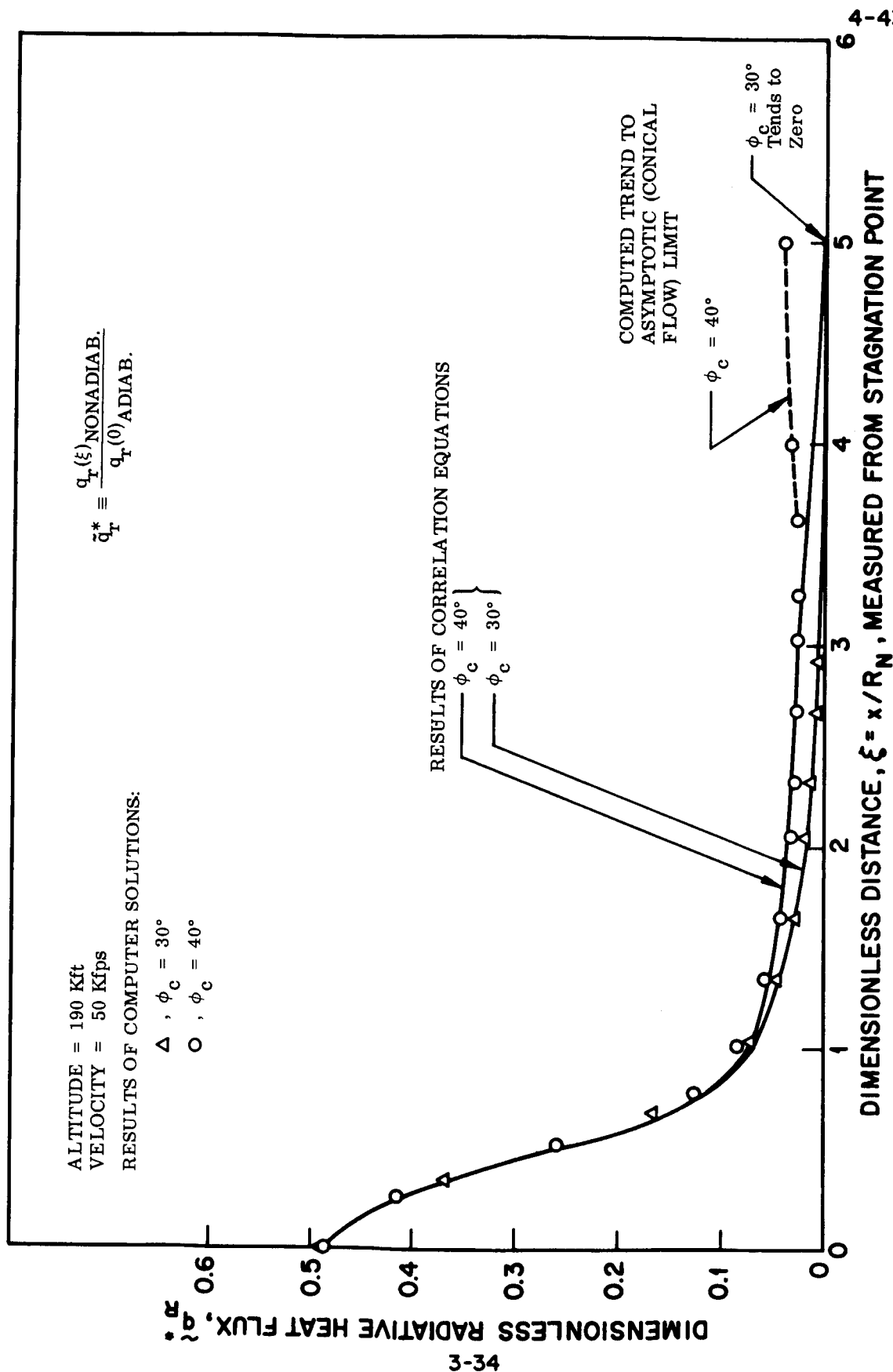


Fig. 24 Radiative Heat Flux Distribution, Hemisphere - Cones Comparison of Correlation Equation With Computer Solution

$$\frac{q_r(\xi)_{\text{Non-Adia}}}{q_r(0)_{\text{Adia}}} = f(\Gamma) \left\{ 2.01 \times 10^{-2} \exp \left[3.90 \left(\frac{p(\xi)}{p(0)} \right)^{1/2} \right] + \frac{q_r(\xi_T)}{q_r(0)} \right|_{\text{Non-Adia}} \cdot \exp \left[-A_2(\xi - \xi_T)^{v_2} \right] \right\} \quad (13)$$

with the term, $f(\Gamma)$ given by Fig. 22, for a range of values of radiation loss parameter, Γ . The other coefficients in the second term on the RHS are used for the hemisphere-cones. The first term, only, is used for the continuous analytic geometries.

Numerics for Conical Radiation Flux Correlation

	$q_r(\xi_T)/q_r(0)_{\text{Non-Adia}}$	A_2	ξ_T	v_2
$\phi_c = 40^\circ$	0.234	1.030	0.873	0.435
$\phi_c = 30^\circ$	0.137	1.285	1.048	0.954

3.2.2 Integration of Radiative Correlation Equations Over Surface Area

Following the procedure used for the convection heating, the correlation Eq. (13) is integrated over the annular differential area element corresponding to each of the specified geometries. Once again, correlation was with the pressure distribution, which is essentially only a geometric characteristic. This permits a generalization of the integrated total heating with geometry as the only parameter. The adjustments for free stream conditions appear in the equations as separately evaluated constant coefficients. Similar to the discussion in Sub-section 3.1.2, extension of the present applications are possible for similar geometries supporting similar pressure distributions or new integrals may be generated using Eq. (3) and dissimilar pressure distributions developed for other geometries.

The integration of the correlation functions for the various geometries results in the general equation for total radiation heating, ratioed to the adiabatic stagnation point heat flux. This equation is in terms of integrals which are evaluated and presented in this section.

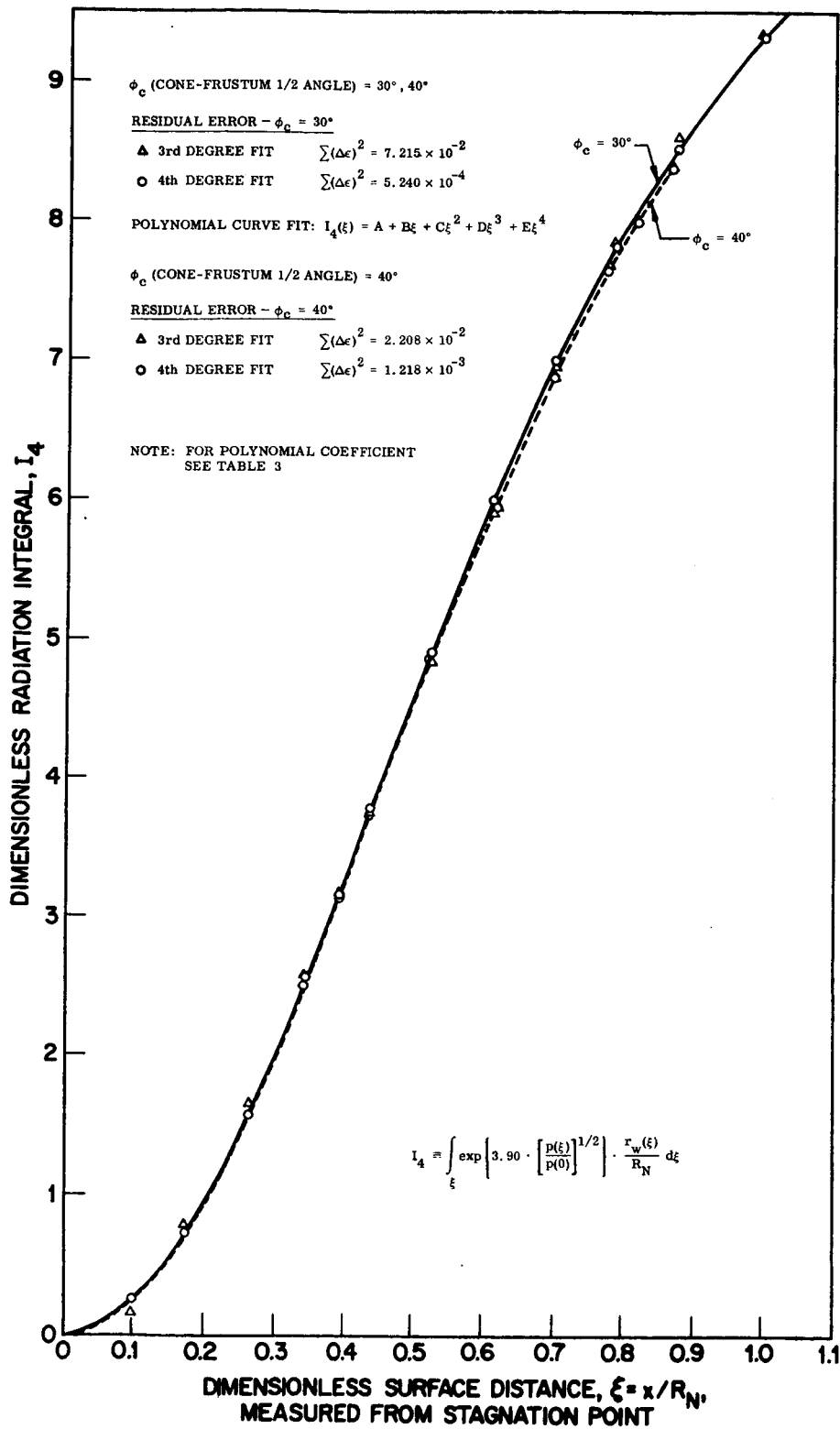
$$\tilde{Q}_r = \frac{1}{R_N^2} \int_{\text{Area}} \frac{q_r(\xi)}{q_r(0)} \frac{\text{Non-Adia}}{\text{Adia}} dA = 2\pi f(\Gamma) \times \left[2.01 \times 10^{-2} I_4(\xi) \right]_{\xi=0}^{\xi=\xi_T} + I_5(\xi) \Big|_{\xi=\xi_T}^{\xi=\xi_{\text{Final}}} \quad (14)$$

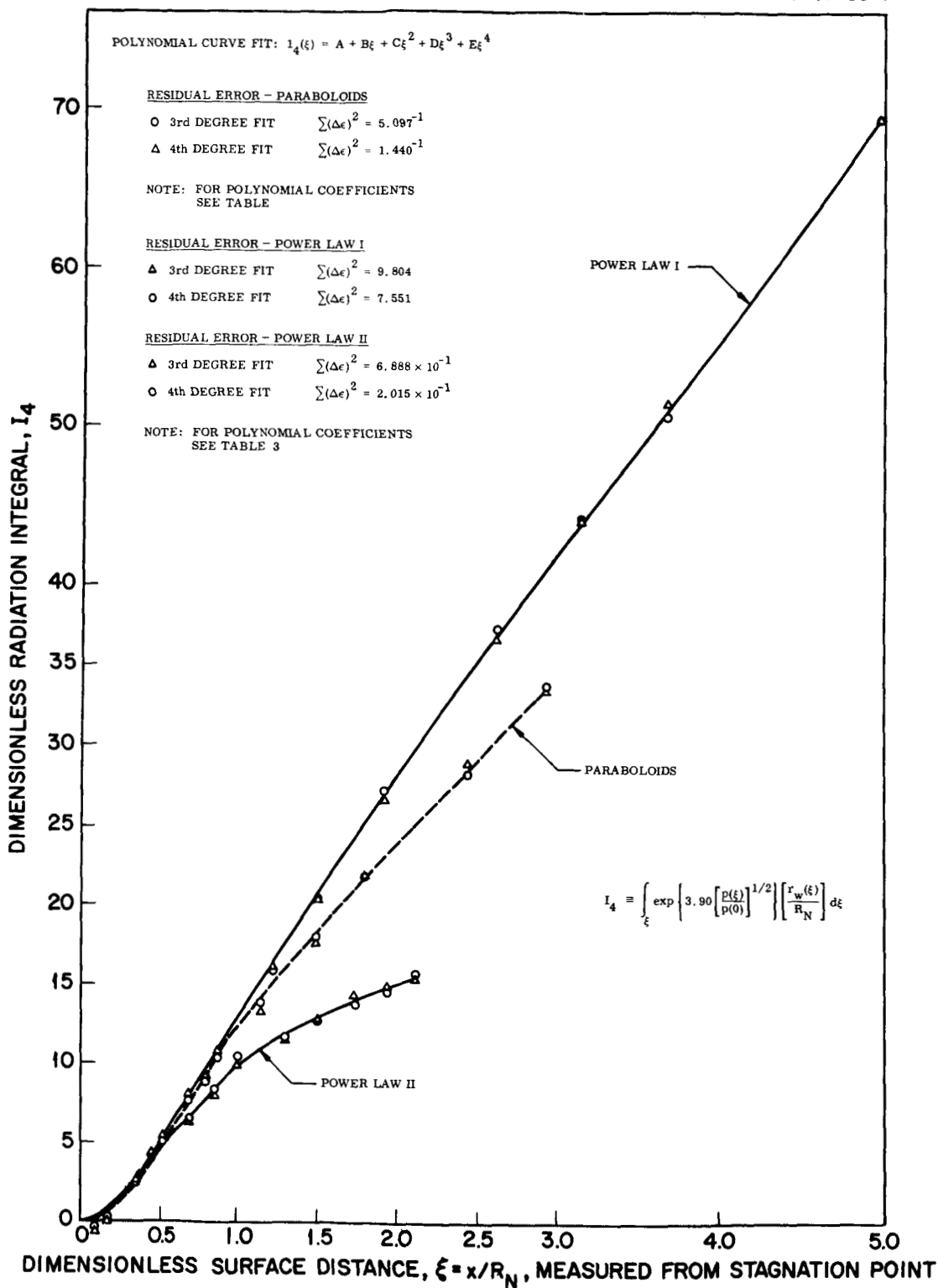
Analogous to the convection integration, the last term in Eq. (14), the integral $I_5(\xi)$ is used for the range of $\xi \geq \xi_T$, applied to the hemisphere-cones. For the continuous geometries this integral does not appear and evaluation is carried out over the entire body surface, using the integral, $I_4(\xi)$.

The evaluated integrals (I_4 and I_5) for arbitrary surface distance, ξ , may be obtained, for the specific geometries analyzed, in Figs. 25, 26, and 27. Again the final fits for the 3rd and 4th degree polynomials are shown explicitly on the figures along with the residual errors. The polynomial equations are of the general form shown in Eq. (9). The cubic form of Eq. (9) may be seen to yield satisfactory accuracy without invoking the more cumbersome 4th degree polynomial. Polynomial coefficients and the % error over the range of integration are listed in Table 3.

3.2.3 Systematic Application of Integrated Radiative Heating Over the Range of Analysis

Consistent with the work on the convection heating component, the total radiation heating as a function of surface distance has been computed for all of the geometries over nine trajectory points representing the range of the present analysis. The calculations were accomplished using the integrated heating expression, Eq. (14) for $R_N = 1 \text{ ft.}, 1/2 \text{ ft.}$

Fig. 25 Dimensionless Radiation Integral, I_4 , Evaluated for Hemisphere Cone

Fig. 26 Dimensionless Radiation Integral, I_4 , Evaluated for Parabolooids and Power Laws

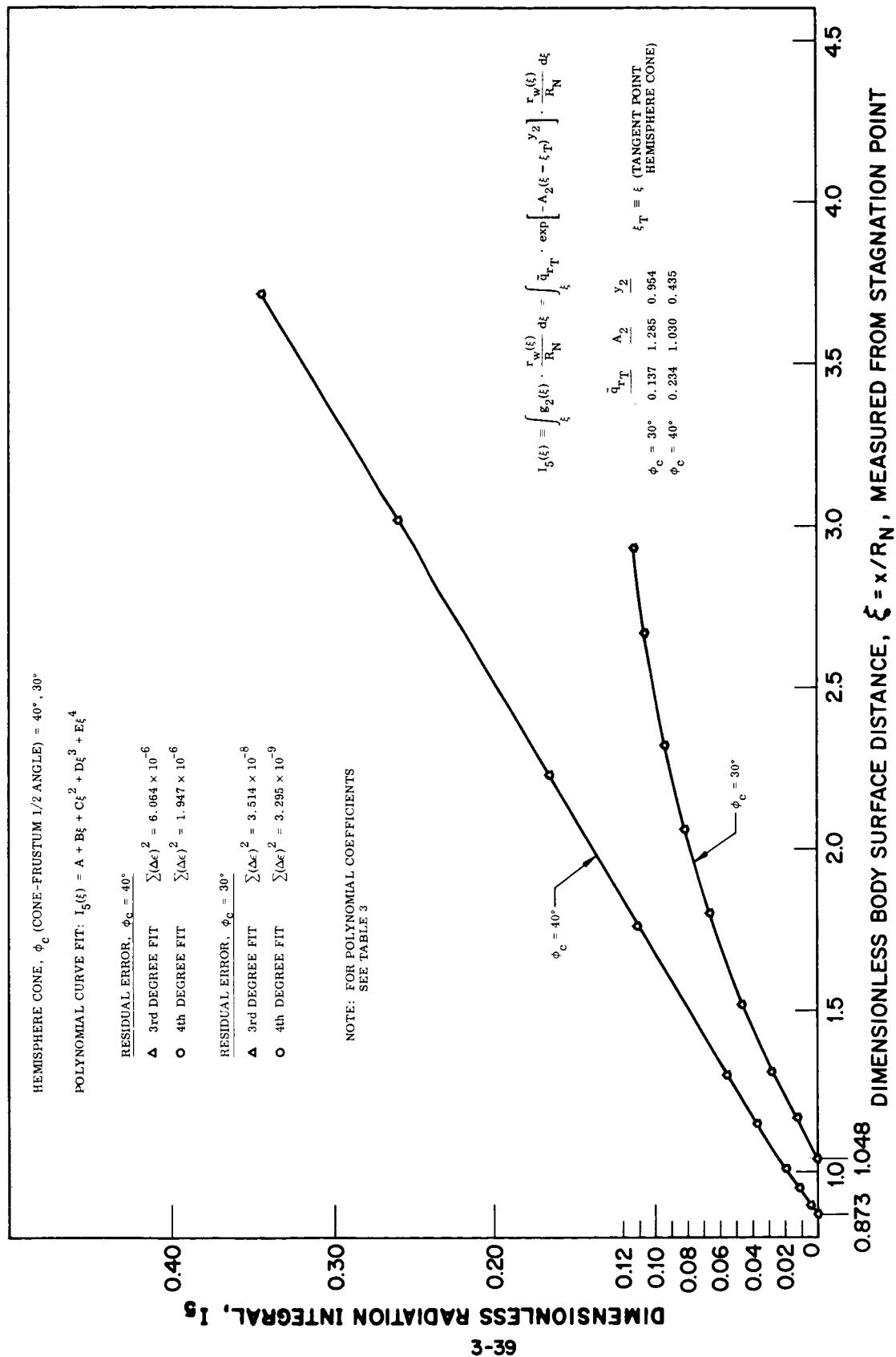


Fig. 27 Dimensionless Radiation Integral, I_5 , Evaluated for Conical Surface

Table 3

POLYNOMIAL COEFFICIENTS - RADIATION INTEGRALS (SEE EQUATIONS (14) & (9)).

POLYNOMIAL EQUATION OF THE FORM: $f(\xi) = A + B\xi + C\xi^2 + D\xi^3 + E\xi^4$

Geometry	Integral	Degree	A	B	C	D	E	% Deviation Over Integral Range
Hem.-Cone $\phi_c = 40^\circ$	I_4	3	-2.518 ⁻¹	2.577	2.132 ⁺¹	-1.483 ⁺¹	1.995 ⁺¹	2.60 ⁻¹
	"	4	2.222 ⁻¹	-3.835	4.695 ⁺¹	-5.382 ⁺¹		1.43 ⁻²
	I_5	3	-1.1784 ⁻¹	1.456 ⁻¹	-1.165 ⁻²	1.585 ⁻³		1.52 ⁻³
	"	4	-1.480 ⁻¹	2.147 ⁻¹	-6.560 ⁻²	1.872 ⁻²	-1.895 ⁻³	4.89 ⁻³
Hem.-Cone $\phi_c = 30^\circ$	I_4	3	-4.647 ⁻¹	4.770	1.585 ⁺¹	-1.078 ⁺¹		7.41 ⁻¹
	"	4	1.744 ⁻¹	-2.995	4.291 ⁺¹	4.693 ⁺¹	1.528 ⁺¹	5.38 ⁻³
	I_5	3	-1.729 ⁻¹	2.207 ⁻¹	-5.926 ⁻²	5.881 ⁻³		3.51 ⁻⁵
	"	4	-1.821 ⁻¹	2.418 ⁻¹	-7.662 ⁻²	1.196 ⁻²	-7.685 ⁻⁴	3.30 ⁻⁶
Paraboloid	I_4	3	-2.196	1.4197 ⁺¹	-1.908 ⁻¹	-1.878 ⁻¹		1.45
	"	4	-1.372	9.840	5.996	-3.316	5.096 ⁻¹	4.30 ⁻¹
Power Law I	I_4	3	-2.745	1.580 ⁺¹	-3.000 ⁻¹	6.862 ⁻³		1.40
	"	4	-1.824	1.132 ⁺¹	4.310	-1.529	1.579 ⁻¹	1.08
Power Law II	I_4	3	-1.226	1.177 ⁺¹	-8.440 ⁻¹	-4.978 ⁻¹		4.48
	"	4	-6.483 ⁻¹	6.750	1.001 ⁺¹	-8.565	1.907	1.31

The results are given in Figs. (28) through (36) with entry conditions listed on the figures and specified geometry, a parameter.

It will be noted that the integrated radiation shows a somewhat different precedence as to relative heating levels in comparison to the convection heating discussed previously. The more oblate power law profile exhibits higher values throughout, with the paraboloid relatively close. The larger of the hemisphere-cones, $\phi_c = 40^\circ$, generates total radiation heating below the two previous analytic profiles, while the two more slender configurations power law II and the 30° half angle hemisphere-cone are lower yet in total heating for a given surface position. The relative sequence for the latter two geometries is the same as that encountered in the investigation of the convection, however the three comparatively blunt profiles are seen to have readjusted their relative positions.

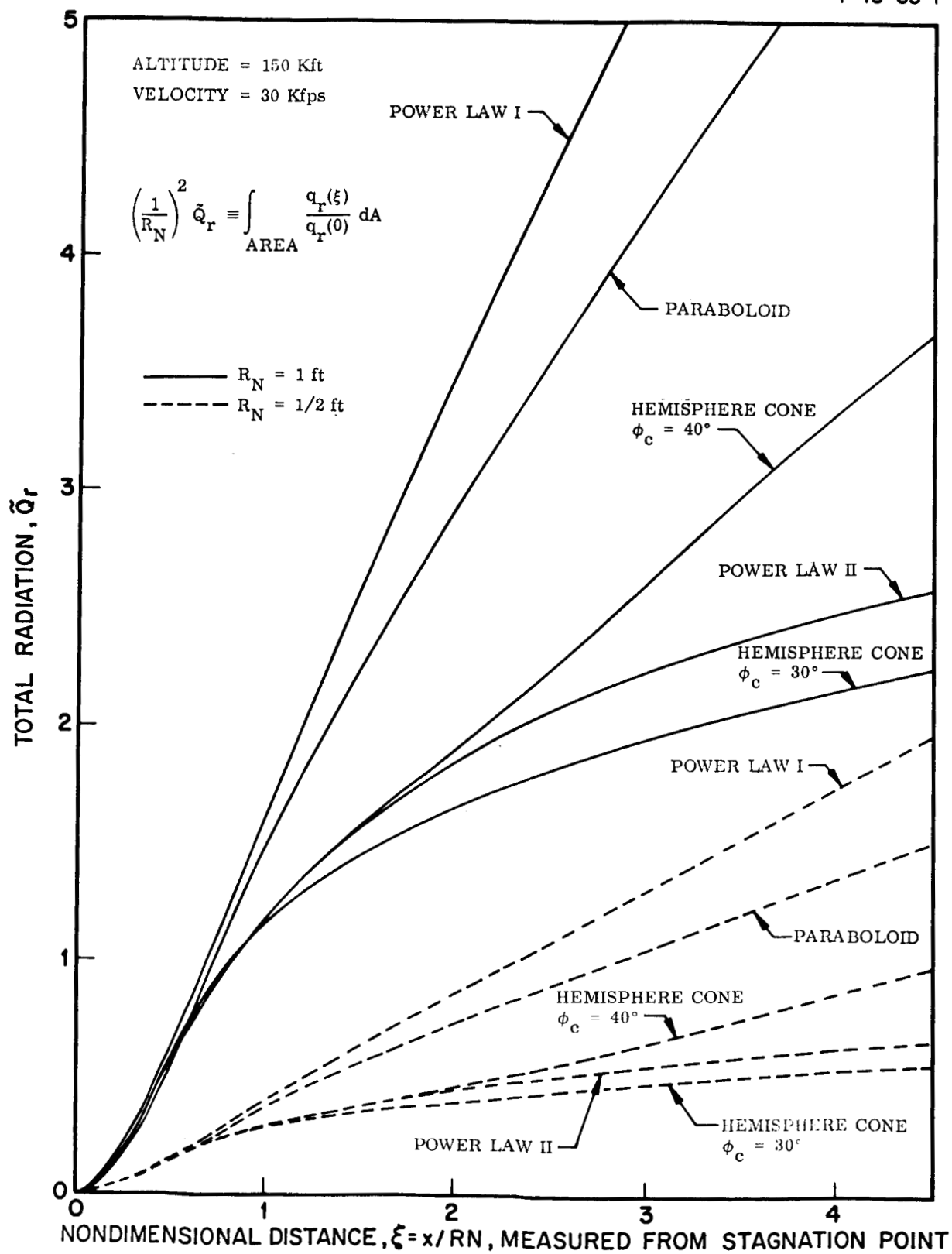


Fig. 28 Radiation Heating Integrated Over Surface Distance

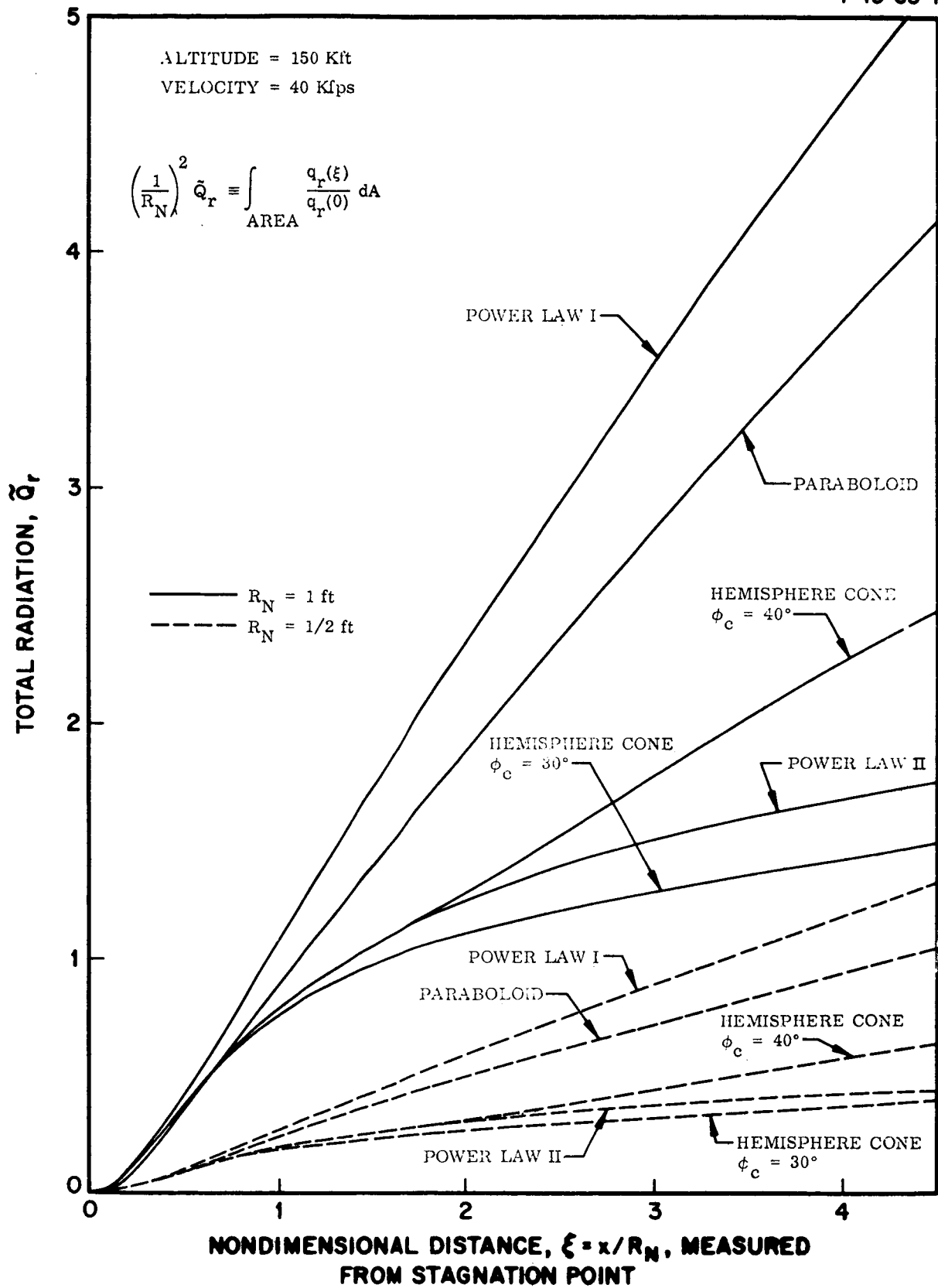


Fig. 29 Radiation Heating Integrated Over Surface Area

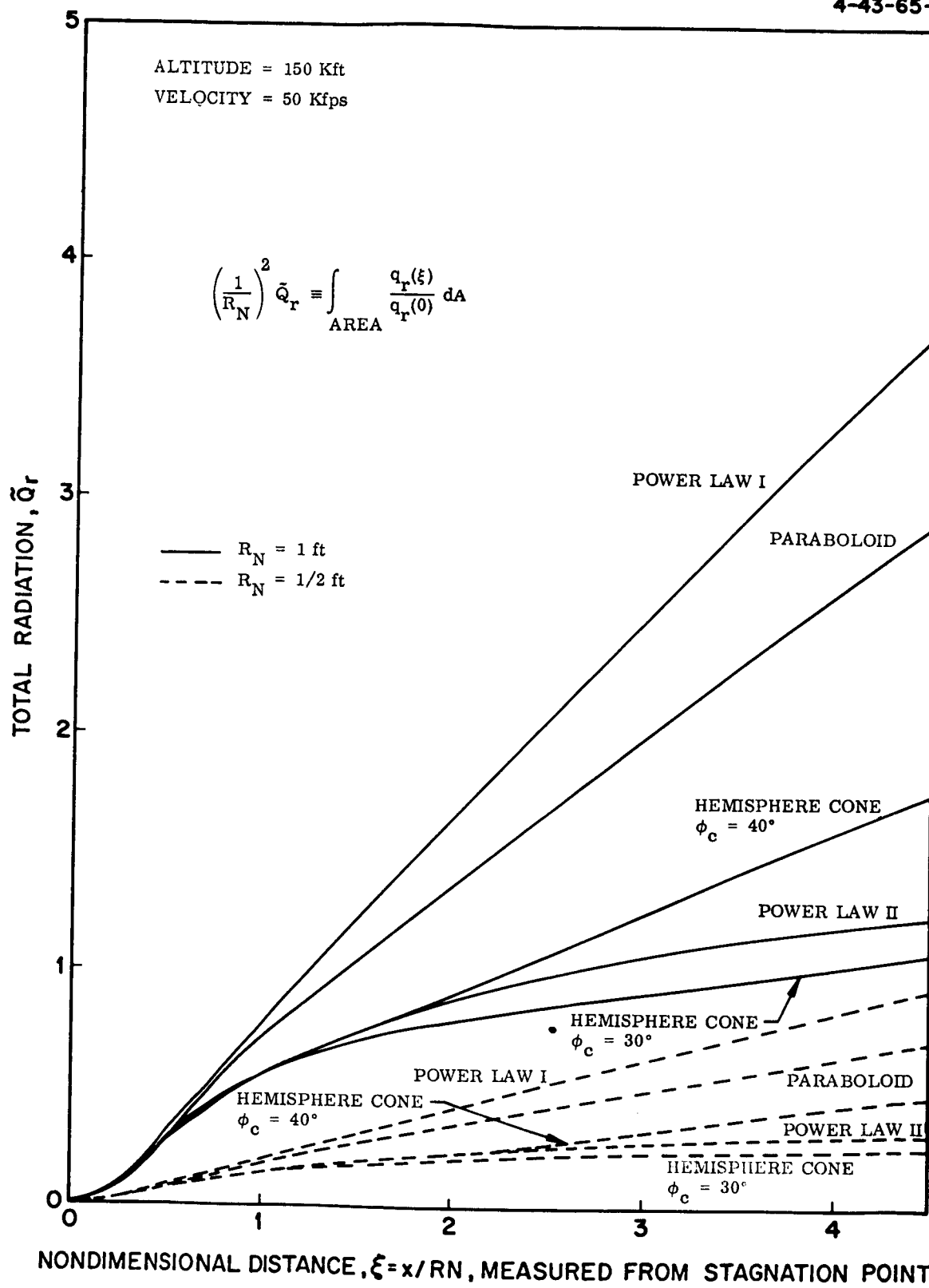


Fig.30 Radiation Heating Integrated Over Surface Area

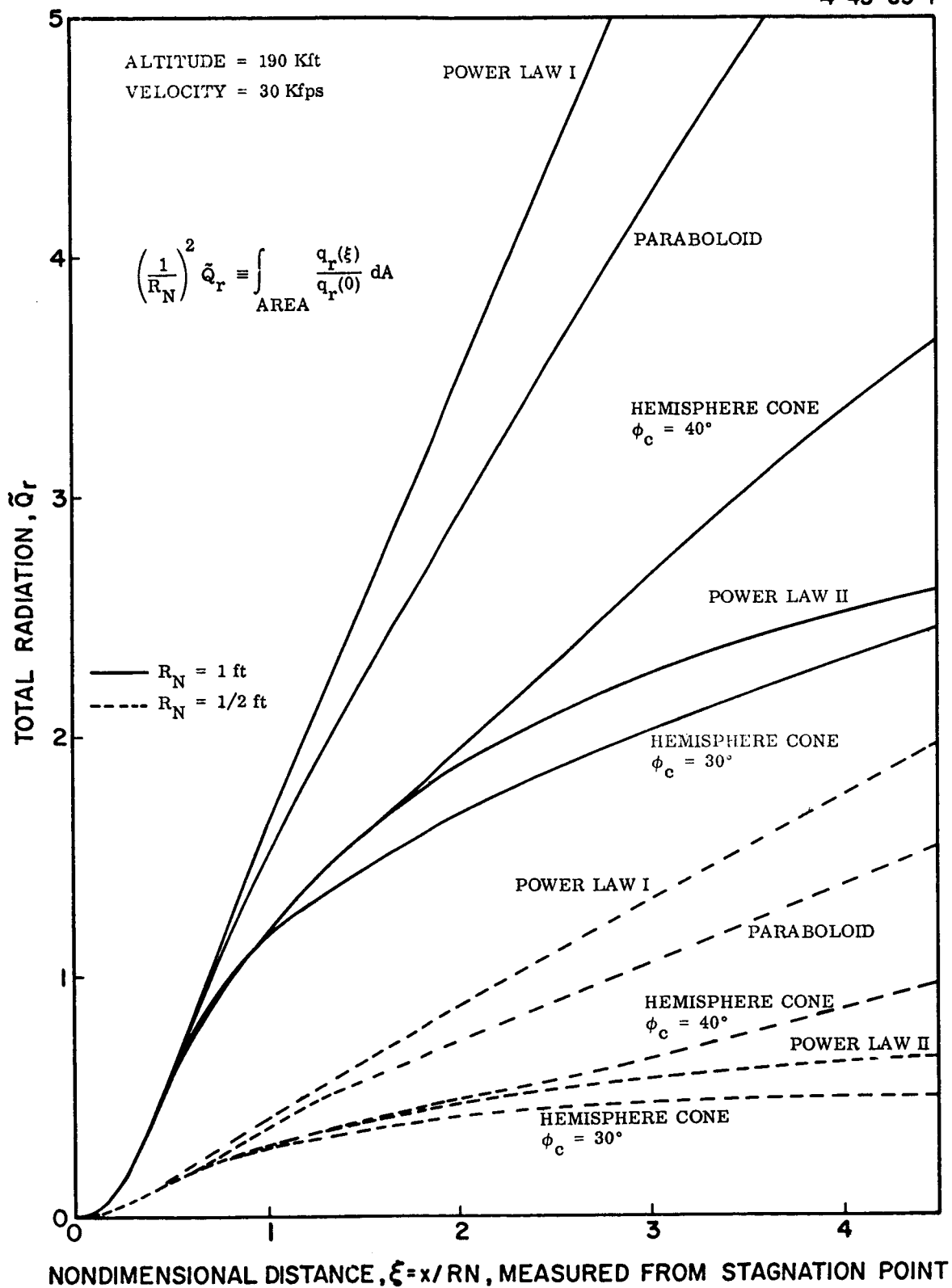


Fig. 31 Radiation Heating Integrated Over Surface Area

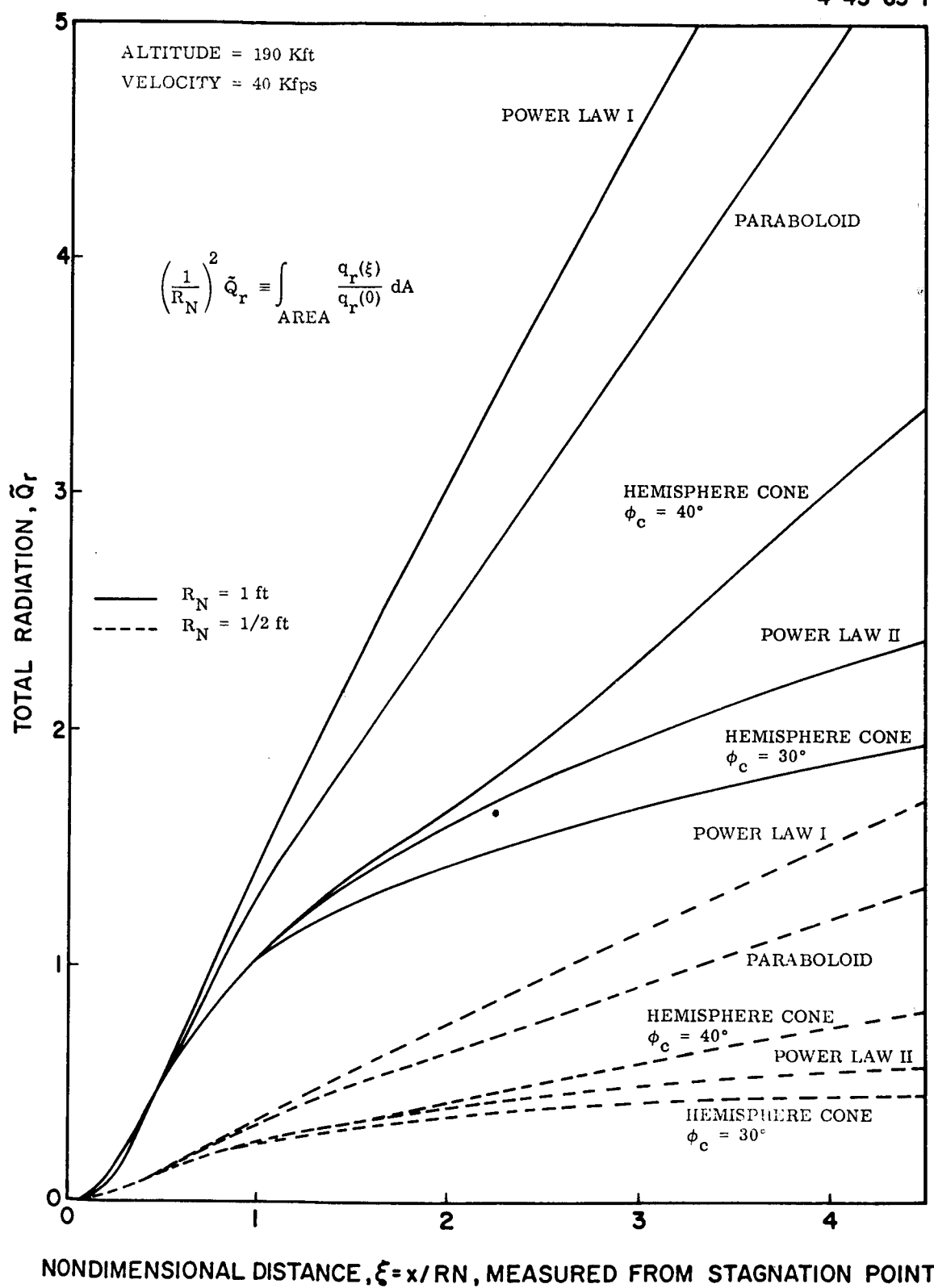


Fig.32 Radiation Heating Integrated Over Surface Area

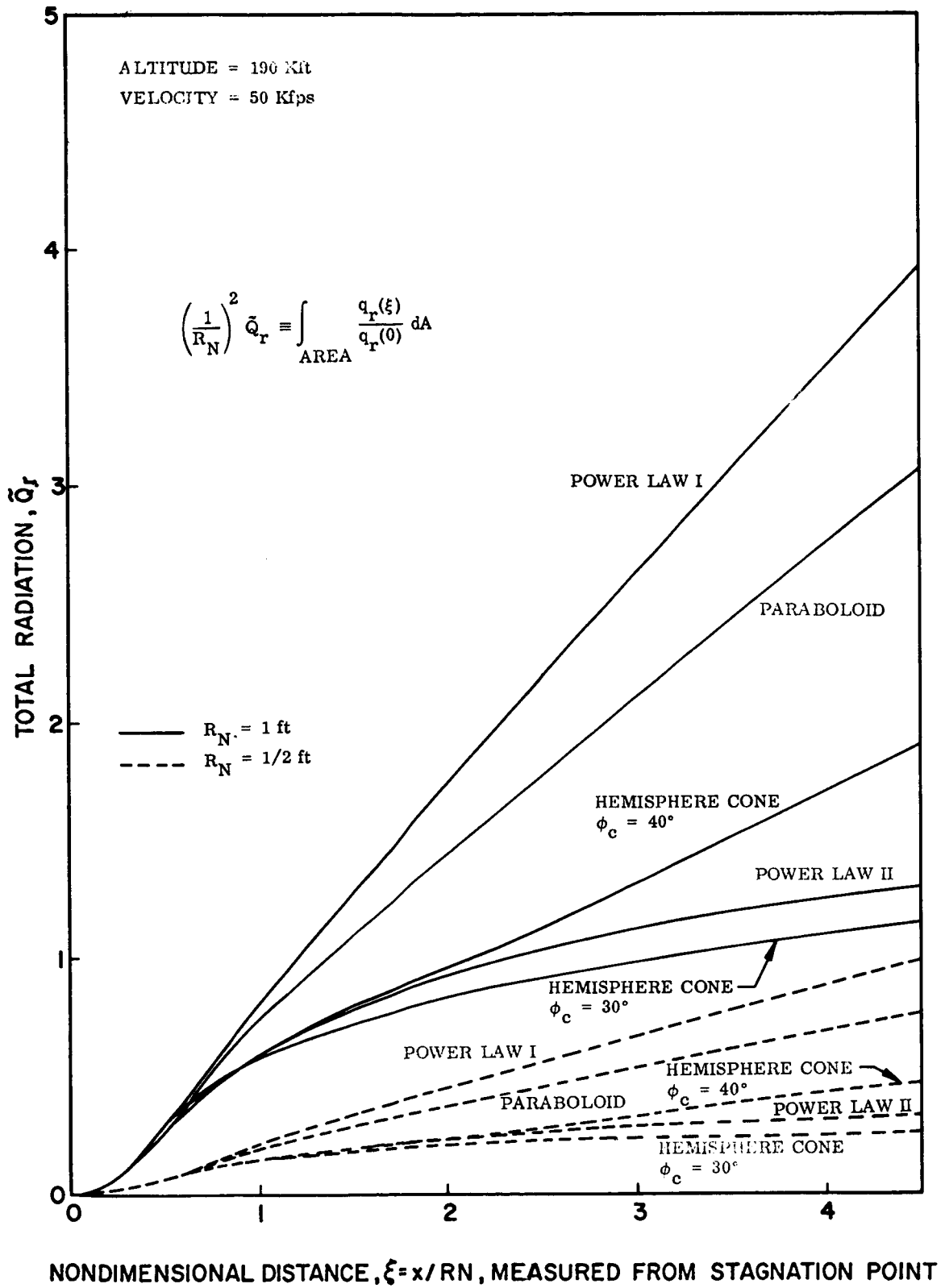


Fig.33 Radiation Heating Integrated Over Surface Area

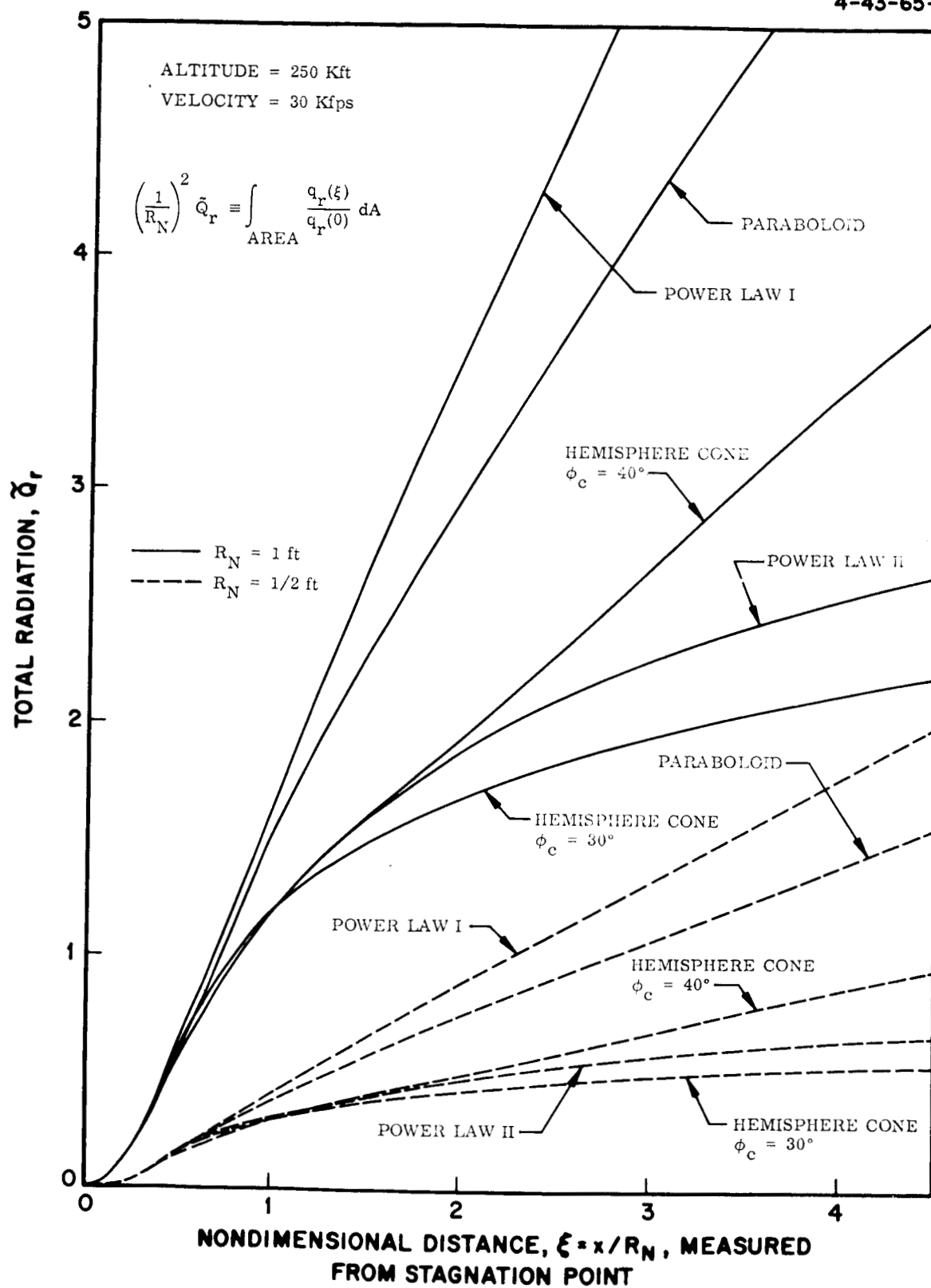


Fig. 34 Radiation Heating Integrated Over Surface Area

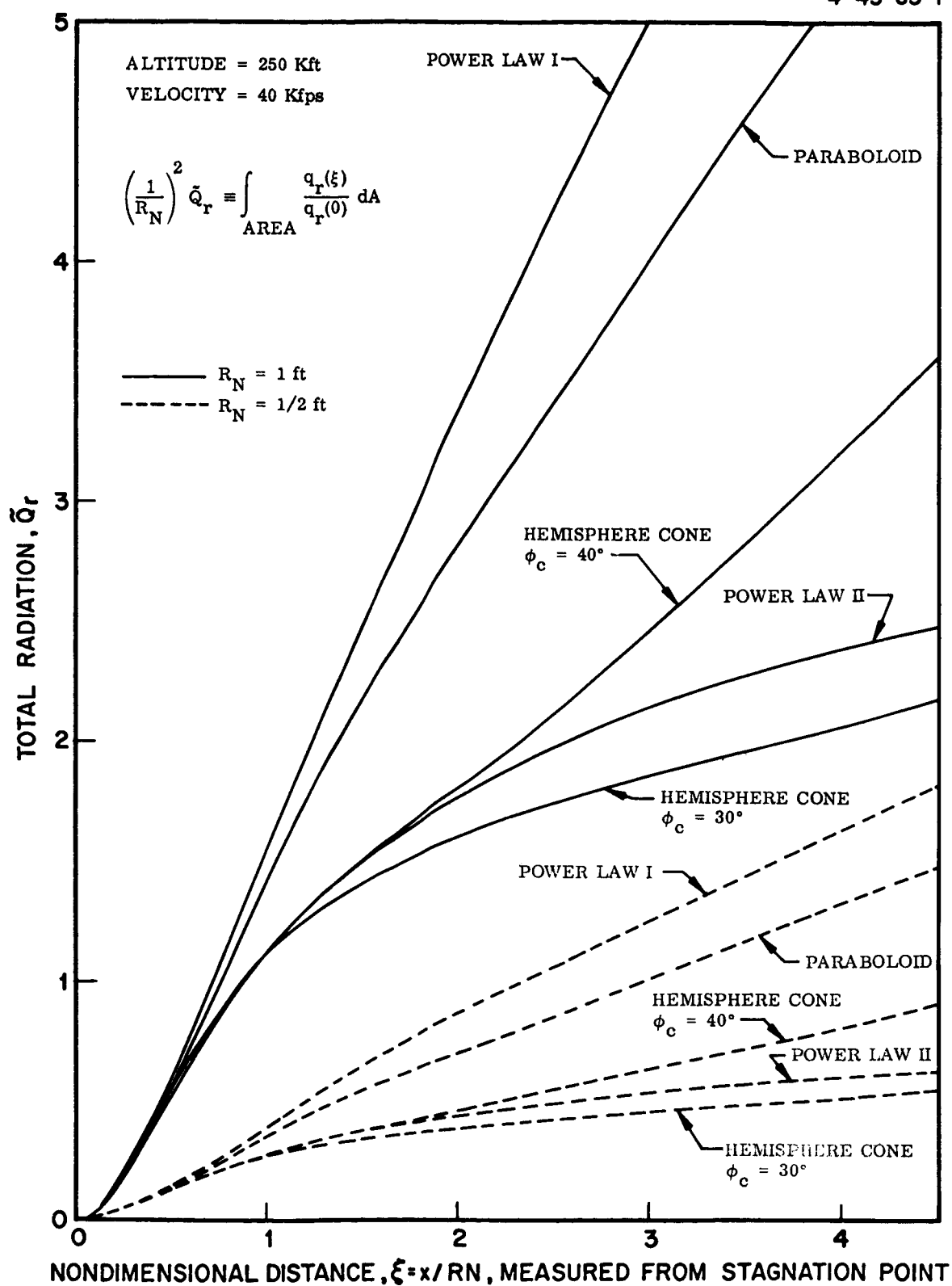


Fig. 35 Radiation Heating Integrated Over Surface Area

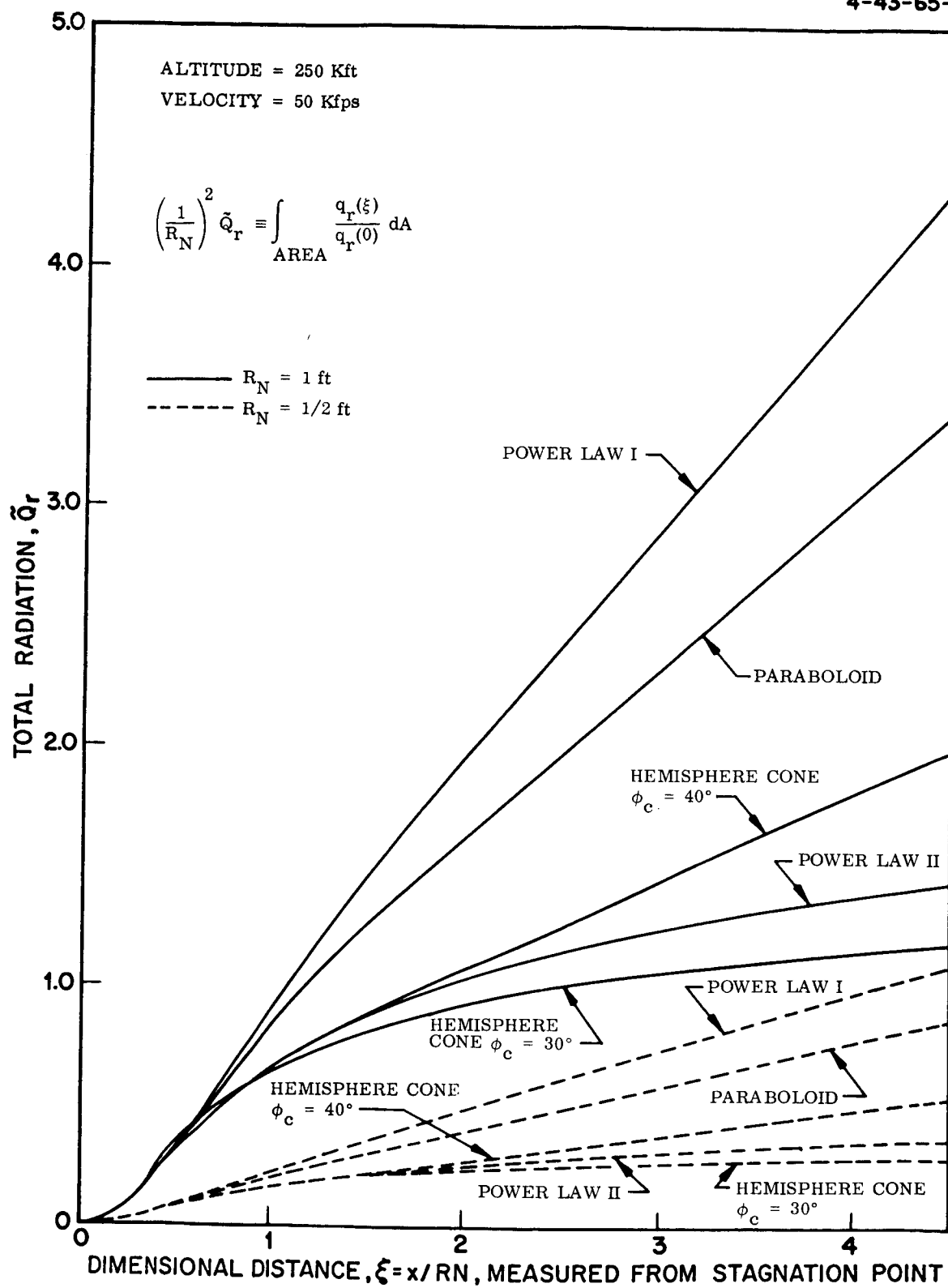


Fig. 36 Radiation Heating Integrated Over Surface Area

3.3 An Evaluation of Geometrical Effects

A standard for comparison for total heating to the variety of dissimilar geometries must be selected. It was decided that a reasonable factor for consideration would be the enclosed volume of the arbitrary geometry. Justification for the importance of the volume is related to the necessity of particular attention to this factor in entry vehicle design for a particular mission. Certainly minimum spatial requirements will be defined by the mission. At the same time a successful design must clearly incorporate estimates of the total heat imposed on the vehicle surface and the resulting internal temperature environment. Such a procedure is followed here to examine effects of geometry on total heating.

Fig. 37 presents the dimensionless volume, $\text{Volume} \times (R_N)^{-3}$, as a function of surface distance, ξ , for the geometries analyzed in the present study. Selection of the desired volume, essentially establishes the surface distance and, through use of Figs. (13) through (21) or (28) through (36), the integrated surface heating for convection and radiation components. Determination of the appropriate stagnation point heat flux converts the dimensionless component heating to the proper level for the flow conditions. The present calculations were computed using the values determined in the numerical computations for the radiative heating and the results of Ref. (7) for the convective heating.

The calculations are based on a 1 ft. nose radius of curvature for a fixed volume of 10 cubic feet. (No significance is attached to this particular volume. It merely represents a convenient selection for the present trial comparison of geometric effects). An intermediate altitude in the range analyzed was selected, $\bar{z}_\infty = 1.9$; with velocities, $\bar{u}_\infty = 3, 4, 5$. This generated results covering a range of coupling from negligible to strong as seen in Fig. 2.

Fig. 38 summarizes the results of the study of the effects of geometry on the total heating. The dependent variable is the total heat flux integrated

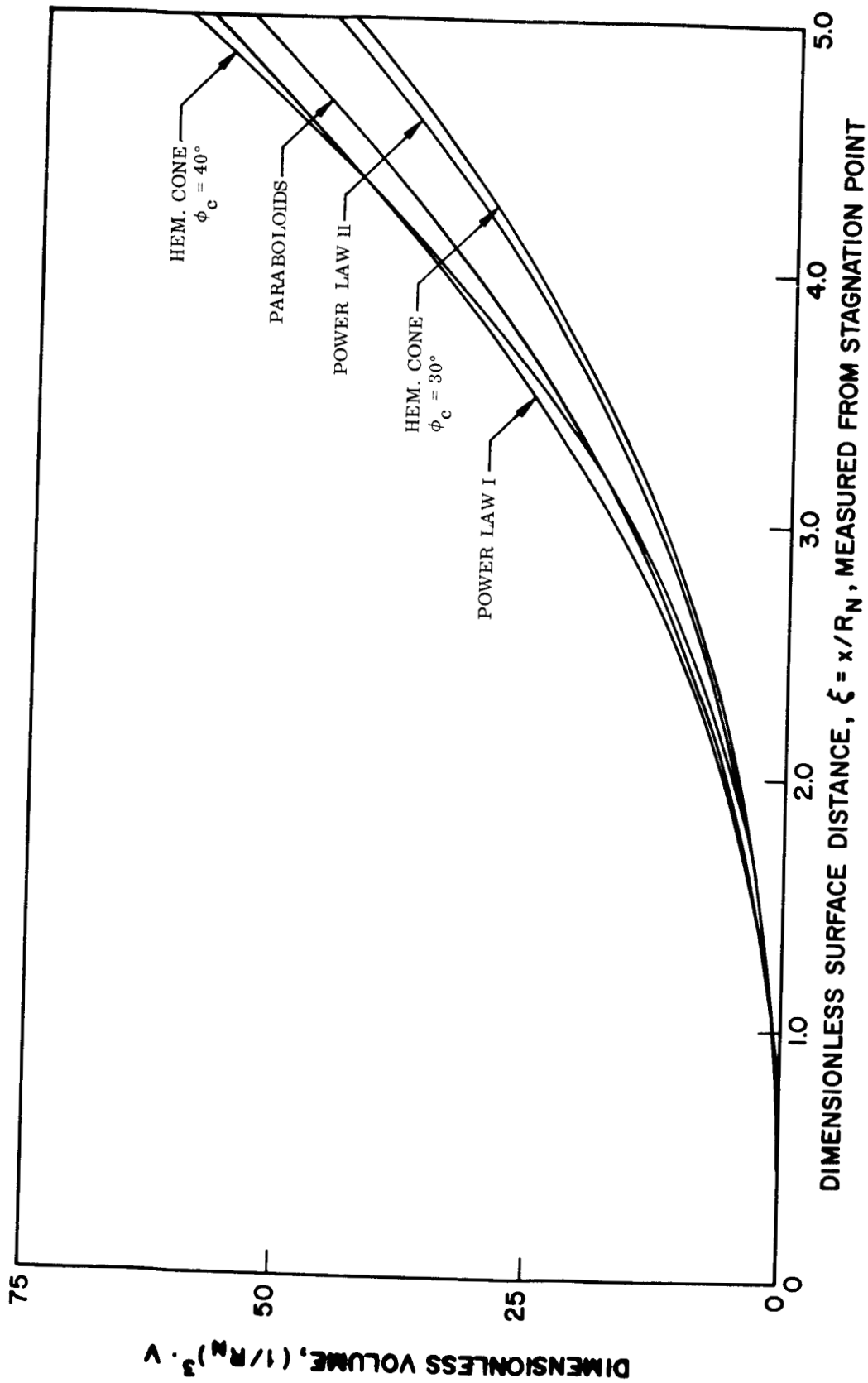


Fig. 37 Dimensionless Enclosed Volume, Evaluated for Geometries Analyzed

4-43-65-1

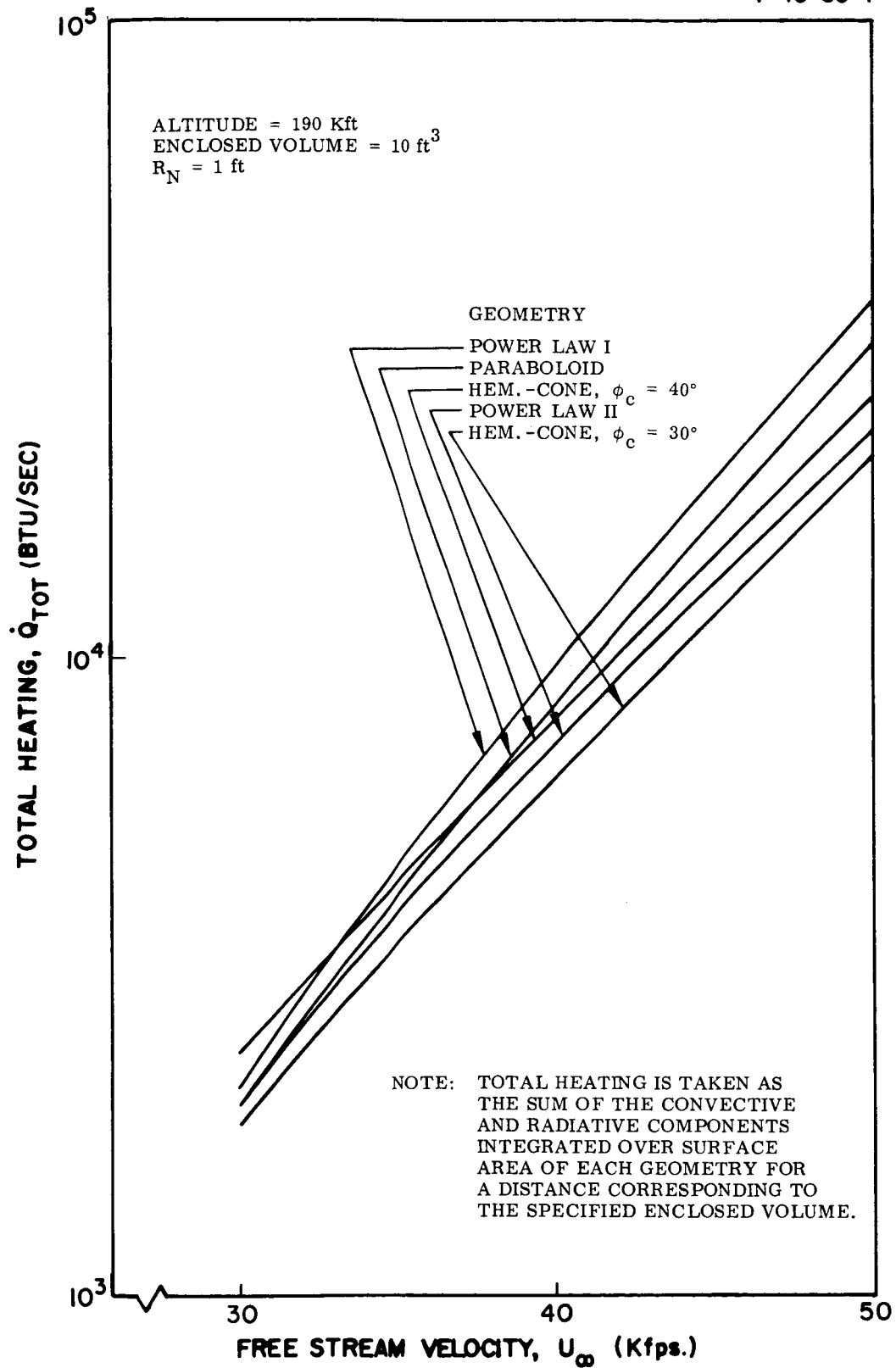


Fig.38 Effect of Geometry on Total Heating for Fixed Volume

over surface area (Btu/sec). The integration is over various surface distances (ξ) which yield the fixed volume specified for the individual geometry as seen in Fig. 37. The independent variable is the free stream velocity within the range $3 \leq \bar{u}_\infty \leq 5$.

The geometrical configurations reflecting the lowest total heating for the fixed volume were the slender profiles (30° hemisphere-cone and power law II). Here "slenderness" is defined as the relative smallness of the simple body fineness ratio for a fixed volume; nose radius of curvature divided by the axial length, ξ . The more oblate profiles; power law I, paraboloid and 40° hemisphere cone exhibit a generally higher total heating for the fixed volume; with the power law I profile the maximum, hence least favorable of the geometries analyzed.

It is also worth noting that the effects of minimizing the total heat through use of relatively slender profiles is slightly offset by the longer surface running length (and correspondingly larger surface area) dictated by a fixed volume requirement.

The conflicting requirements for slenderness to minimize total heating and relative bluntness to maximize volume are indicated here but no contradiction to the greater advantages with the more slender profiles was found for this range of geometries.

3.4 Effect of Mass Injection and Self Absorption of Radiant Energy

In the present analysis we have neglected the effect of self-absorption of radiant energy and the effect of ablation product mass injection into the shock layer. We cannot rigorously justify the neglect of these quantities but can only attempt to estimate the effect they will have on the results presented in this report.

At the time this study was initiated there was very little information on the effect of self-absorption. The gray-gas approximation, in which a mean absorption coefficient is employed, was thought to be valid and estimates of the effect of self-absorption using the Planck mean indicated that the shock layer would be optically thin for most reentry situations. New information which is currently available shows that the gray-gas approximation is a very poor one in terms of obtaining meaningful quantitative results on radiative energy transfer.

In this section, some new results on self-absorption effects obtained from additional work being carried out for NASA are presented. In Fig. 39 are presented the continuum absorption coefficients as calculated by Armstrong (Ref. 13) along with a correlation curve which is an empirical modification of the simplified Penner-Thomas analysis (Ref. 14). This correlation formula for the continuum absorption coefficient, which accounts only for atoms and ions, was used to calculate the energy transfer out of a plain parallel slab with the enthalpy profiles shown in Fig. 40. This slab can be thought of as an approximation to the local conditions in the shock layer of typical reentry bodies with the slab being bounded by the vehicle surface and the shock wave.

The radiative flux to the body and out through the shock wave was evaluated in three different ways. The gas was first assumed to be optically thin, secondly, the gray-gas approximation was employed, and finally spectral integration over frequency was carried out. The ratio of the radiative flux to the wall and through the shock wave, with and without self-absorption

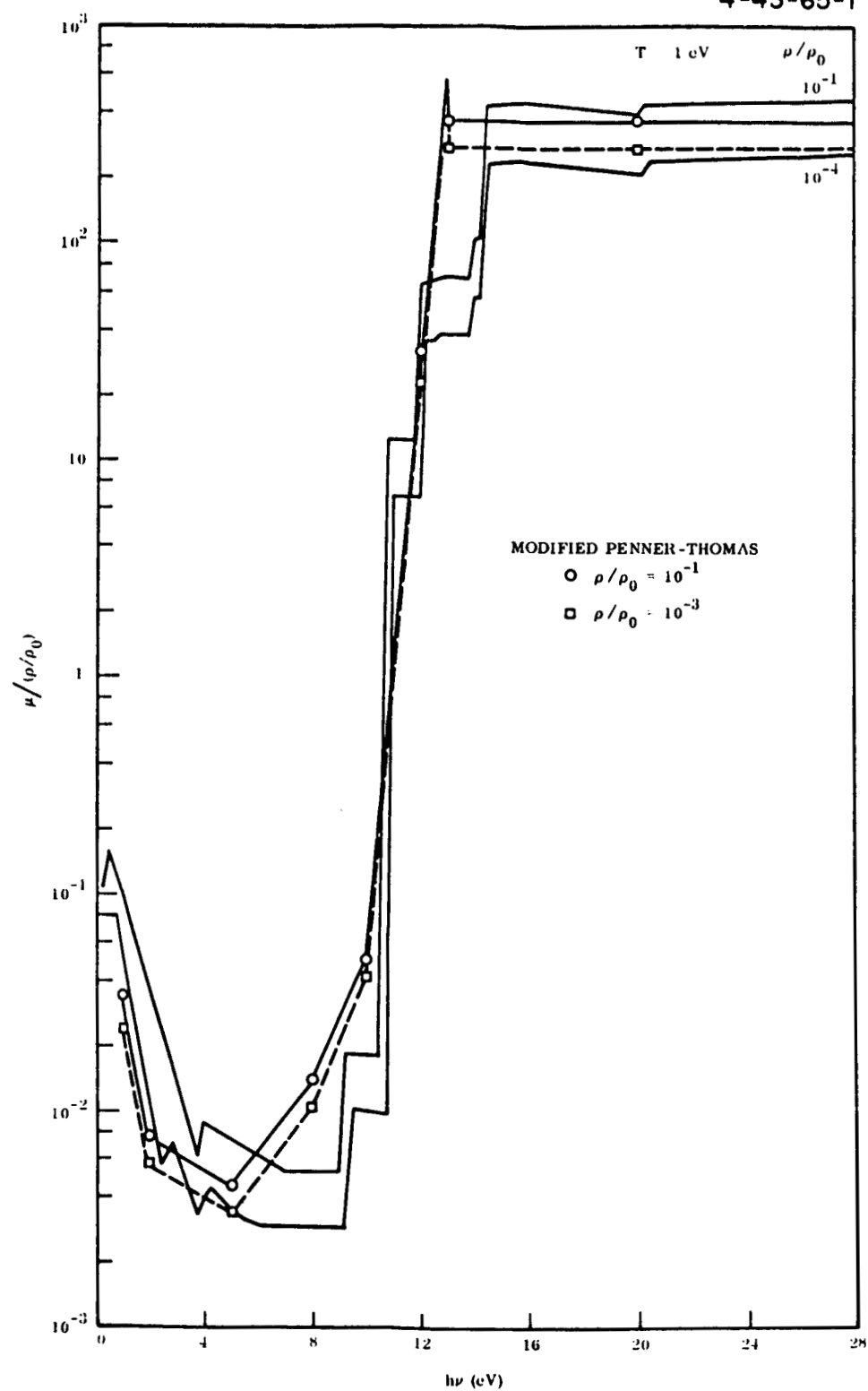


Fig. 39 Continuum Absorption Coefficients of Nitrogen

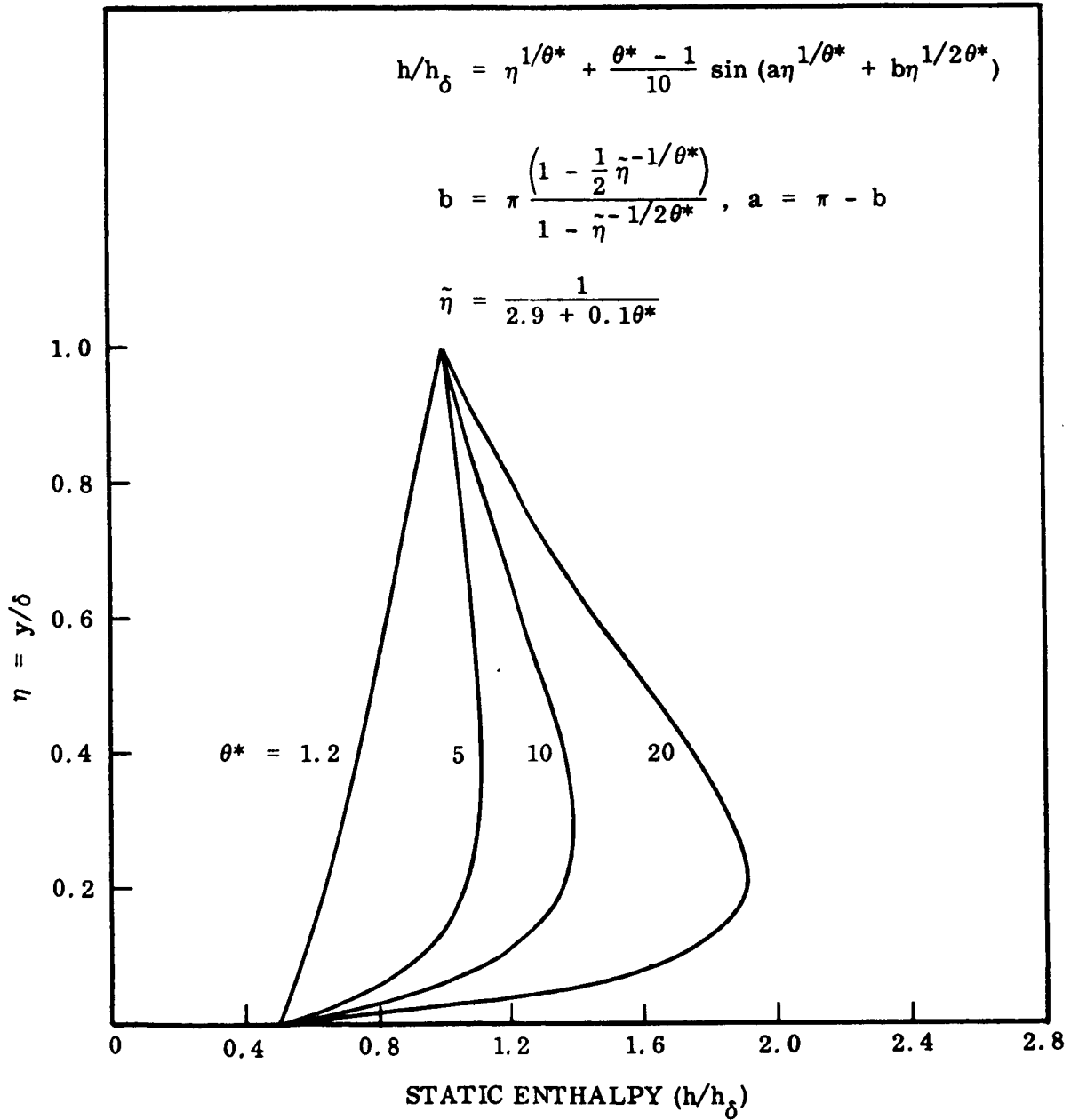


Fig. 40 Static Enthalpy Profiles

are presented in Fig. 41. In Fig. 42, the corresponding distribution of the radiative flux with frequency both at the wall and at the shock are presented. These results show that for small values of the enthalpy form parameter θ^* , the vacuum ultraviolet portion of the spectrum of the radiative flux to the wall is highly absorbed. For large values of θ^* , the vacuum ultraviolet is absorbed much less since maximum emission occurs much closer to the wall as can be seen by inspection of the enthalpy profiles (Fig. 40). As expected, the results for the radiative flux through the shock exhibit the opposite behavior with θ^* than the radiative flux to the wall.

These results show first of all, that the gray-gas approximation can lead to misleading results and that self-absorption will reduce the radiant energy flux to the surface and through the shock significantly. In terms of the present analysis this means that if self-absorption were taken into account the flow in the shock layer would be more nearly adiabatic since less energy is lost by radiation and secondly, the radiative flux to the surface would be greatly diminished. Self absorption in the shock layer is a function of the shock layer thickness and the density. At the stagnation point the density is high, relatively speaking, and the shock layer thin, while in the after-body region the densities are low and the shock layer thick. Although this tends to make the effect of self-absorption uniform over the body, it is conceivable that the radiative heating distribution may be significantly altered by self-absorption.

Since a great deal of absorption occurs in the cool air near the body convective heating may be significantly increased. This raises an interesting point which is "How is the total heat flux to the surface affected by self-absorption?". An extension of the viscous shock layer analysis to include self-absorption will provide the answer to this question. Even if the total heating is not significantly altered, the response of this surface material will be affected since the surface material will respond differently to a heat flux which is applied purely by radiation and to a heat flux due to convective heating. The difference being that in the case of pure radiative heating the ablation products will blanket the surface and inhibit the surface

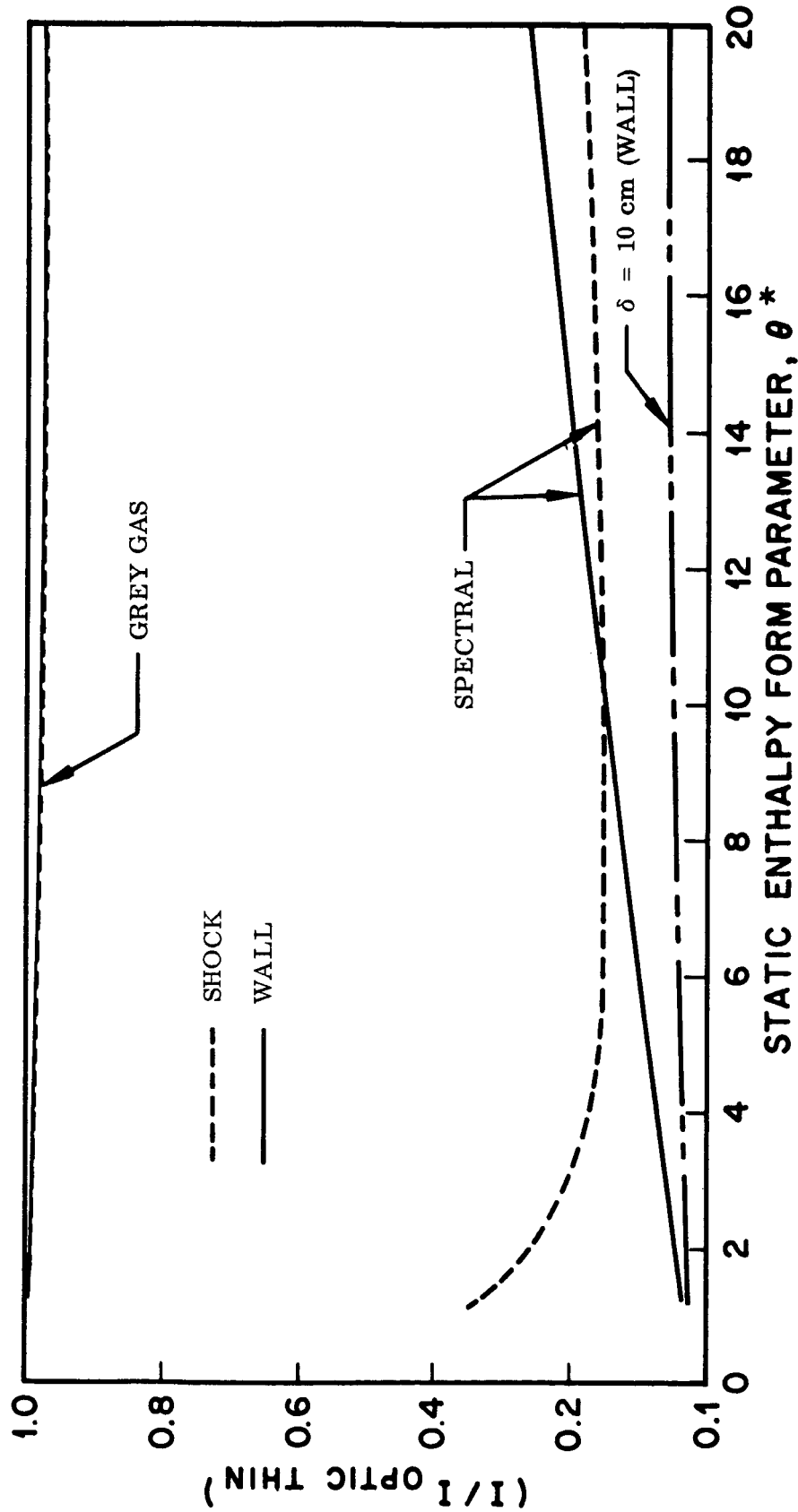


Fig. 41 Ratio of Radiative Flux With and Without Self-Absorption
For a Slab of Gas 1 cm Thick. $p = 1 \text{ atm}$
Temperature Behind Shock $= 11,400^\circ \text{K}$, $\rho_g/\rho_o = 1.1 \times 10^{-2}$

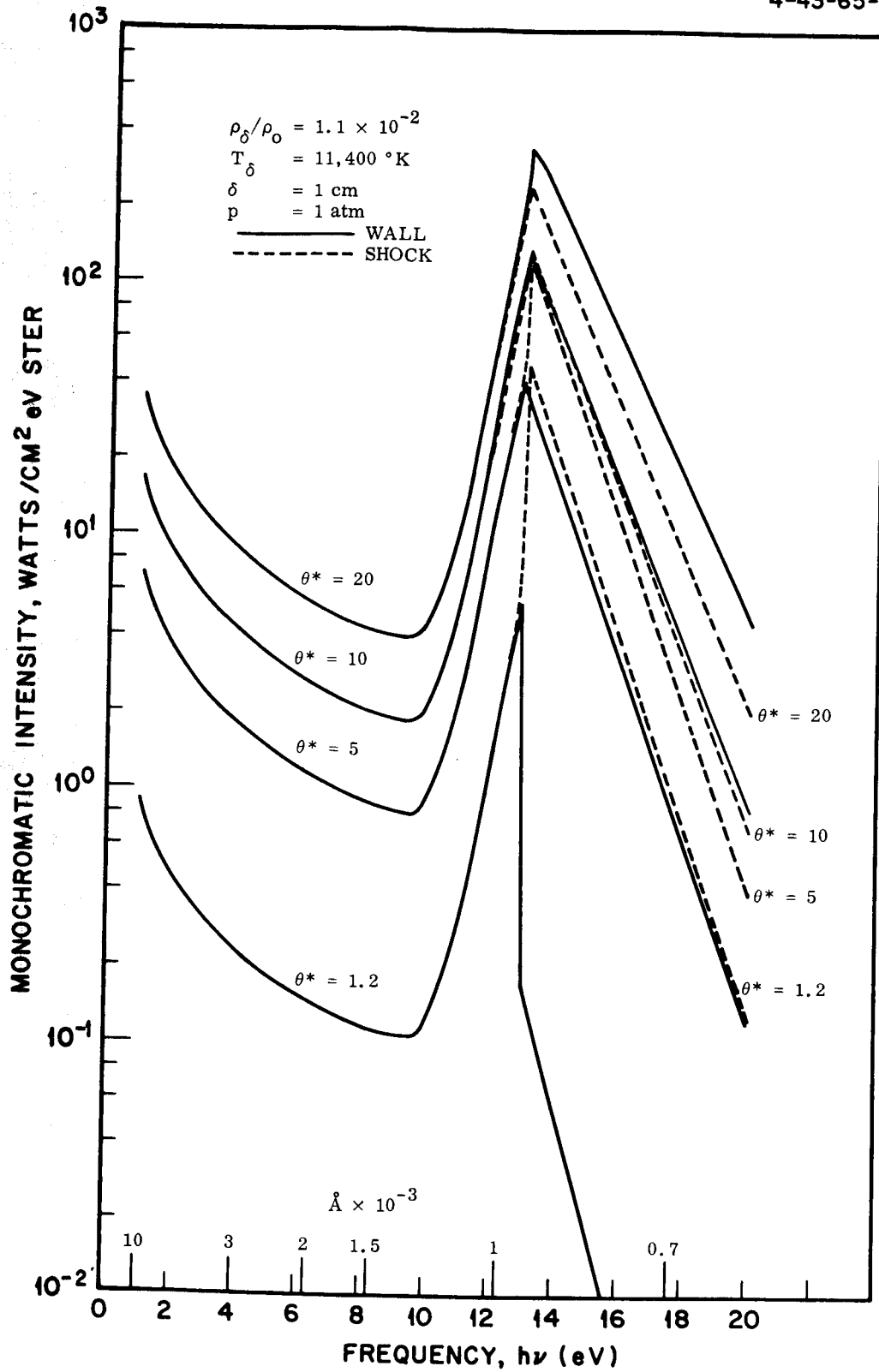


Fig. 42 Monochromatic Intensity as a Function of Frequency, $h\nu$

reactions between the air molecules and the surface.

The injection of mass into the shock layer will effect both the radiative and the convective heating. In the case of radiative heating injection of the relatively cool ablation products into the shock layer will decrease the radiative flux to the surface by absorption. In some cases, if the ablation products diffuses into the higher temperature regions of the shock layer, they may increase the local radiative flux. The net result, however, will probably be a reduction in the radiative flux to the surface. Mass injection will greatly reduce the convective heating as shown by the results of Howe (Rf. 15) which are presented in Fig. 43. This reduction is proportional to the total heat flux to the surface. For severe entry conditions the convective heating can be reduced to significant levels by the injection of the ablation products. The effect of mass injection on the present results will be to decrease the differences in the convective heating between the different body shapes considered. This is so because those configurations which have the largest heat flux will also have the largest reduction in the convective heating since the mass injection rates are proportional to the total heat flux.

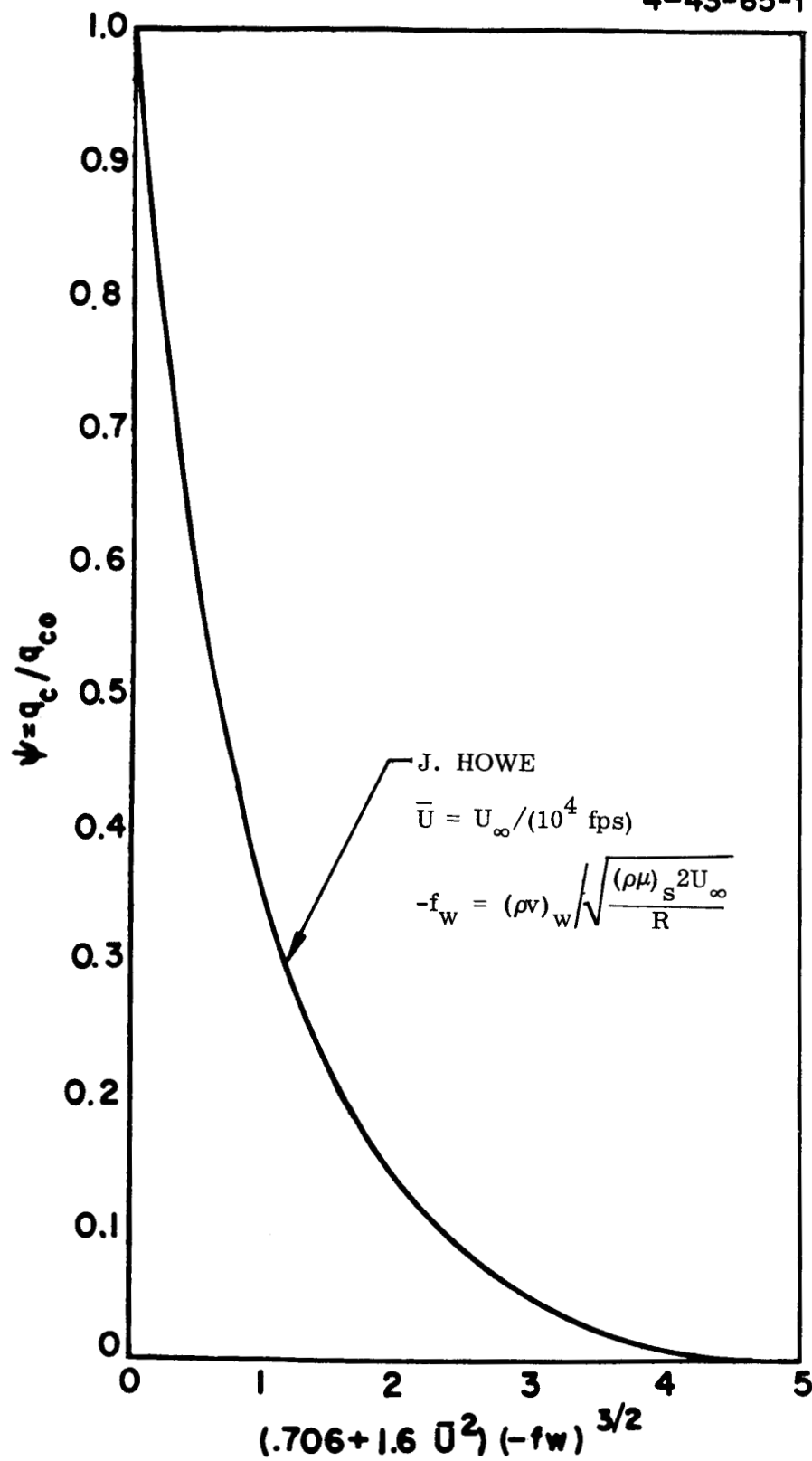


Fig. 43 Reduction of Convective Heating due to Mass Injection

4. SUMMARY AND CONCLUSIONS

It has been demonstrated that the relatively complex problem of investigating the coupled convective and radiative heating to an entry body moving at superorbital speed may be simply summarized by correlation of selected numerical solutions. The basis of the present study was a series of numerical solutions for arbitrary geometries and flight conditions generated using a theoretical solution and digital computer program developed at Lockheed.

The present analysis does not incorporate the effects of shock layer self absorption or mass addition. A critical discussion is presented in the report on the possible effects from those processes relative to the problem analyzed here. Further analysis of these effects necessarily awaits completion of a new computer program presently being developed which incorporates self-absorption and mass injection. In addition the new program is being prepared with a capability for solution over a much larger range in temperature and density with respect to the thermodynamic and transport property functions. It follows that a much larger range in superorbital entry conditions may be investigated with the new code. In addition, the present success with the correlation approach has given added incentive to investigation of other possible geometrical profiles that show promise for superorbital entry vehicles.

In summary, results of the present studies indicate the following conclusions:

The most readily obtainable hypersonic flow distribution variable (surface pressure) is a successful choice for a correlation variable. Thus distribution of heating can be expressed as a simple function of geometry (as demonstrated by the invariance of hypersonic surface pressure distribution with fixed geometry).

Specific flight environments may then be simulated by calculating the values of separate coefficients which are functionally dependent only on free stream conditions and nose radius of curvature.

A variety of studies of the heating environment encountered by arbitrary geometries may be developed using the simple correlations in relation to a fixed design criteria. Once such criteria, a fixed volume requirement, is analyzed here and suggests that slender configurations with small nose radius of curvature show the most promise in minimizing the total heat transferred to the vehicle surface in superorbital entry regimes.

5. REFERENCES

1. Hoshizaki, H., and Wilson, K. H., "The Viscous Radiating Shock Layer About a Blunt Body," AIAA Journal, Vol. 3, No. 9, Sept. 1965, pp. 1614 - 1622
2. Viegas, J. R. and Howe, J. T., "Thermodynamic and Transport Property Correlation Formulas for Equilibrium Air from 1000°K, to 15,000°K," NASA TN D-1429, Oct. 1962.
3. Allen, H. J., and Seiff, A., "Aerodynamic Heating of Conical Entry Vehicles at Speeds in Excess of Earth Parabolic Speed," NASA TR-R-185, Dec. 1963.
4. Kivel, B., and Bailey, K., "Tables of Radiation from High Temperature Air," AVCO-Everett Res. Lab., Res. Report 21, 1957.
5. Howe, J. T., and Viegas, J. R., "Solutions of the Ionized Radiating Shock Layer, Including Reabsorption and Foreign Species Effects and Stagnation Region Heat Transfer," NASA TR-R-195, 1963.
6. Marrone, P. V., "Normal Shock Waves in Air: Equilibrium Composition and Flow Parameters for Velocities from 26,000 to 50,000 ft/sec," Cornell Aero. Lab., Rept. No. AG-1729-A-2, 1962.
7. Hoshizaki, H., "Heat Transfer in Planetary Atmospheres at Super Satellite Speeds," ARS Journ. (32), 10, p. 1544, 1962.
8. Thomas, P. D., "Air Emissivity and Shock Layer Radiation," J. Aerosp. Sci. (29), 4, p. 477, 1962.
9. Lees, L., "Laminar Heat Transfer Over Blunt Nosed Bodies at Hypersonic Flight Speeds," Jet. Prop. (26), 1, p. 4, 1965.
10. Cohen, N. B., "Boundary Layer Similar Solutions and Correlation Equations for Laminar Heat Transfer Distribution in Equilibrium Air at Velocities up to 41,000 ft/sec," NASA TR-R-118, 1961.

11. Peng, T. C., and Pindroh, A. L., "An Improved Calculation of Gas Properties at High Temperatures: Air," Boeing Co. Report D2-11722, 1962.
12. Vinokur, M., "Hypersonic Flow Around Bodies of Revolution Which are Generated by Conic Sections," Paper given at 6th Midwestern Conf. on Fluid Mech., U. of Texas, Sept. 1959. Also Lockheed Missiles & Space Company Report LMSD 288139 (1), Part 1 (Fluid Mech.), Jan 1960.
13. Armstrong, B. J., "Opacity of High Temperature Air," AF Weapons Lab. Final Report, Contract AF 29(601)-5006 (to be issued).
14. Penner, S. S., and Thomas, M. "Approximate Theoretical Calculation of Continuum Opacities," AIAA Journ, (2), 9, 1964.
15. Howe, J. T, and Y. S. Sheaffer, "Mass Addition in the Stagnation Region for Velocity Up to 50,000 Feet per Second," NASA TR-R-207, Aug. 1964.
16. Hoshizaki, H., Buckingham, A. C., Wilson, K. H, and Chisnell, R. F., "Study of Superorbital Entry Heating Problems. Quarterly Progress Report for the Period 3 June to 3 Sept. 1964," 1st Quarterly Progress Report Contract No. NAS 7-295, Sept. 1964.

APPENDIX A

ANALYSIS OF ENTRY TRAJECTORY, NOSE RADIUS AND NOSE BLUNTNES

A.1 ENTRY TRAJECTORY AND NOSE RADIUS OF CURVATURE

The initial task completed in the present study was an analysis made of 24 lifting entry vehicle trajectories with initial entry velocities ranging up to 70 Kfps. The analysis, summarized in the 1st Quarterly Progress Report (Ref. 16) showed that the different initial conditions and vehicle aerodynamic properties generated characteristically different heating profiles. It was found, for example, that peak heating trajectory points were widely scattered and that no "representative" heating profile could characterize even a limited variation in superorbital entry conditions. Thus heating pulse width, shape, decay and characteristic heating decay times were all found to vary to a degree which precluded any systematic generalization. The subsequent heating study thus had to be directed at obtaining results for a variety of superorbital trajectory points representing a large range of possible conditions.

This preliminary trajectory study was accomplished using a 3 degree-of-freedom numerical computer code developed at LMSC. The computer code has built-in correlation equations for the adiabatic stagnation heat radiative and convective flux components as a function of trajectory and atmospheric variables. Hence it was possible to examine the uncoupled total stagnation point heat flux from the computer output for the range of selected entry conditions. Peak heating for both convective and radiative heating occurred at or very near pull-out on all of the trajectories analyzed. The results were useful in determining the effects of nose radius on the reduction of the peak total heating in the stagnation region. This study is summarized in Fig. A.1, a two part graph showing the nose radius of curvature (ft.) which results in the total minimum heating stagnation point total heat flux ($\frac{\text{Btu}}{\text{Ft}^2\text{-sec}}$) as a function of free stream velocity and altitude. Constant altitude bands

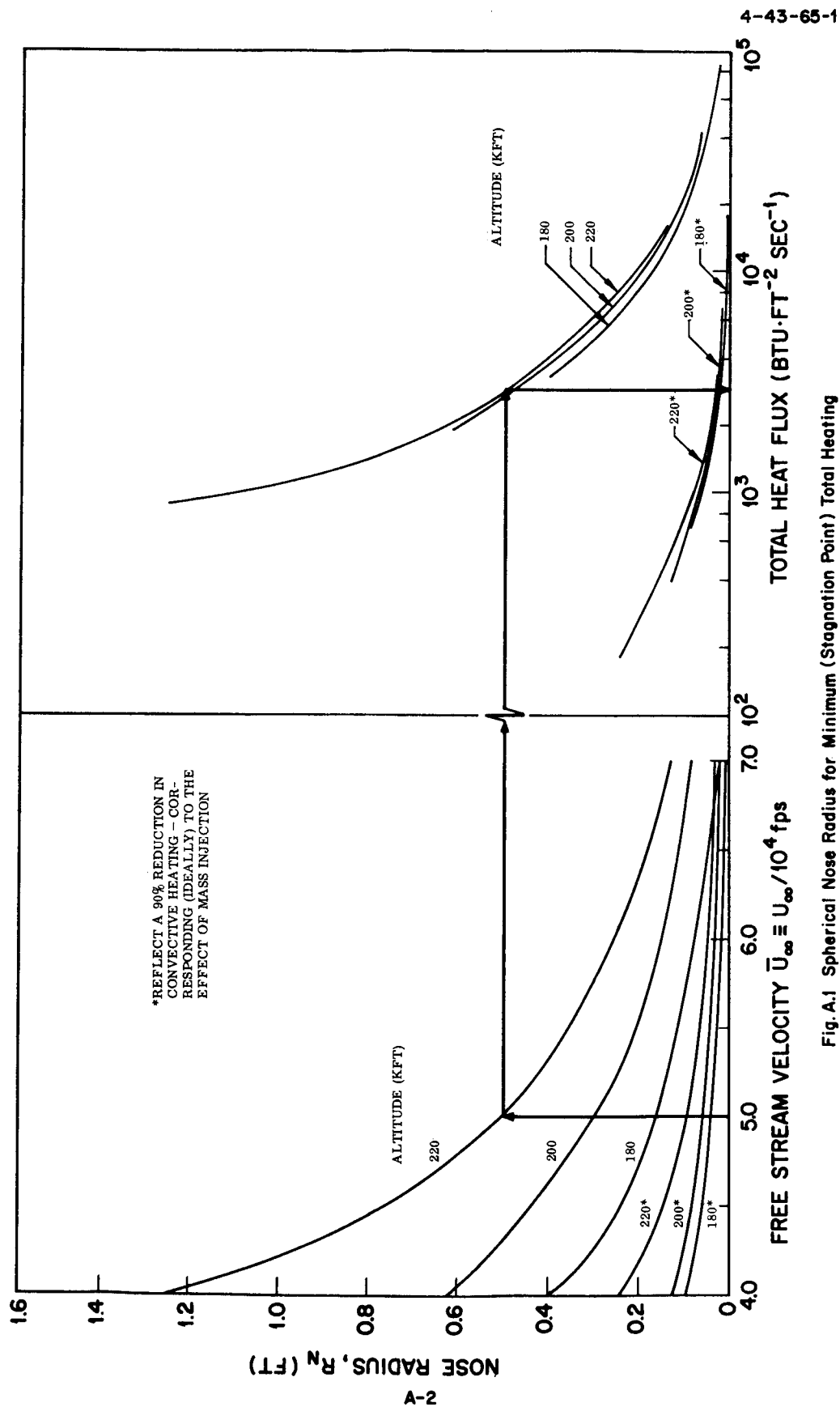


Fig. A.1 Spherical Nose Radius for Minimum (Stagnation Point) Total Heating

(180, 200, 220 Kft) serve as the parameter linking both parts of the Figure. The velocity range is from 40 to 70 kfps.

The results indicate that minimum heating is associated with small nose radii ($R_N \leq 1$ ft.) for all practical combinations of velocity and altitude in the range analyzed. The average is around $R_N = 0.2$ for velocities greater than 50 Kfps). Also shown on the figure are curves (signified by an asterisk on the altitude call-out) which are based on calculations in which a 90% reduction in the convective heating component was used to simulate the ideal effects of mass injection. While these curves show a variation in the scale of the effects (and a reduction in the nose radii for minimum heating because of the greater dependence on the radiation component) the trends are the same as shown by the results for no mass injection. Studies described in the body of this report are based on nose radii of $\frac{1}{2}$ and 1 ft., consistent with the trends depicted here.

A.2 NOSE BLUNTNESS

One of the initial objectives of the present study was to determine the effect of nose bluntness on the total heating. The motivation for investigating the effect of nose bluntness on total heating was based on the following observations:

- o The convective heating can be significantly reduced by radiation cooling
- o Blunting the nose will increase the particle transit time and hence the radiation cooling.

By blunting the nose, the convective heating to the nose and the after-body region will be minimized by maximizing the radiation cooling. The radiative heating will be increased in the nose region but can (it was thought initially) be reduced to insignificant levels by quickly expanding the flow around the body. It was thought that the trade-off between the decreased convective heating and the increased radiative heating would be favorable in that the total heating would be substantially reduced. However, it turned out that the entropy layer generated by bluntness creates a hot layer of gas near the body which